Probing the Non-Trivial states of Low Dimensional Topological Materials by Magnetotransport

SHAMA

A thesis submitted for the partial fulfillment of
the degree of Doctor of Philosophy

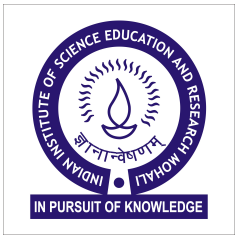

Department of Physical Sciences

Indian Institute of Science Education and Research (IISER) Mohali

Knowledge city, sector 81, SAS Nagar, Manauli PO, Mohali 140306, Punjab, India

September 2022

To my family

Declaration

The work presented in this thesis has been carried out by me under the guidance of Dr. Yogesh Singh at the Indian Institute of Science Education and Research Mohali. This work has not been submitted in part or in full for a degree, a diploma, or a fellowship to any other university or institute. Whenever contributions of others are involved, every effort is made to indicate this clearly, with due acknowledgment of collaborative research and discussions. This thesis is a bonafide record of original work done by me and all sources listed within have been detailed in the bibliography.

Shama
(Candidate)

In my capacity as the supervisor of the candidate's thesis work, I certify that the above statements by the candidate are true to the best of my knowledge.

Dr. Yogesh Singh
(Supervisor)

Acknowledgments

Firstly, I would like to thank my thesis supervisor, Dr. Yogesh Singh, for providing me the opportunity to work under his guidance. I am grateful to him for his efforts during scientific discussions related to my project. I am highly thankful to him for giving me the freedom to explore my own ideas and learn new research skills during this entire journey. His constant support and encouragement helped me at various stages of my graduate studies. I would also like to thank my thesis committee members: Dr. Goutam Sheet, Dr. Sanjeev Kumar, for their insightful comments, encouragement, and technical questions, which helped me to widen my research from various perspectives.

I am very thankful to IISER Mohali for the generous financial support during my Ph.D. I would like to acknowledge the use of the PPMS Sonipat (CFMS 14T, Cryogenic Ltd.), Central Research Facility, IIT Delhi for some electrical transport measurements. I want to thank Dr. S. Chakraverty from INST Mohali, India, for providing PPMS for electrical transport measurements.

I would like to acknowledge the XRD facility, Raman facility, and SEM facility of IISER Mohali. I am thankful to Vivek for helping me in using the EDX facility. I thank Dr. Angshuman Roy Choudhury, for the SC XRD characterization of our grown single-crystal samples.

My sincere thanks also go to Dr. R. K. Gopal for fruitful discussions during my research. I am very thankful to my labmate Anzar Ali for all the discussions and support in the lab. I want to thank my fellow lab-mates Amit, Ashwini Balodhi, Kavita Mehlawat, Jaskaran Singh, Dr. Ritu Rawat, Dr. Gaurav Sharma, Savita, Barkha, Sarvesh, Pradeep, Harleen Kaur, Ankit, and Peyush for their valuable help and support.

I would also like to thank my batchmates and friends Aastha Vasdev, Sandeep Howladar, Gokul, Sudipto, Kanika Singla, Ritesh Kumar, Suman Kamboj, Anshu Sirohi, Monika, Deepti Rana, Shekhar Das, Mohammad Aslam, Leena Agarwal, Soumya Datta, Soumyadip Haldar, Shelender Kumar, Shyam Sundar Yadav, Pankaj, Ramu Kumar Yadav, all others for their help and for making my years enjoyable at IISER Mohali.

I am incredibly grateful to my parents for their selfless love and giving me the liberty to choose what I desired. This work would not have been possible without their blessings and support. I am very thankful to my best friend Dr. Atul Kumar Dubey, Research Associate, IIT Delhi, India, for his selfless support.

Abstract

The discovery of topological materials such as topological insulators, topological semimetals, topological superconductors, etc., has led to a surge in condensed matter physics owing to their non-trivial band structure. Topological insulators (TI) are insulating materials with conducting edge/surface states protected by time-reversal symmetry. These edge/surface states are immune to non-magnetic impurities. Due to spin-orbit coupling, the conducting edge/surface states have a spin momentum locking property. The spin momentum locking results in the helical nature of surface states. Topological semimetals (Dirac/Weyl) are the three-dimensional phases of matter with gapless electronic excitations. The degeneracy of band crossings gives rise to distinct topological semimetal phases such as Dirac or Weyl semimetals, and beyond these. 3D Dirac semimetals (DSM) can be seen analogous to 2D Graphene, with the Dirac bands dispersing linearly in all three momentum directions. In DSMs, conduction and valence bands touch each other at discrete points in the Brillouin zone, called Dirac Points. These Dirac points are degenerate, protected by time-reversal (TRS) and inversion (IS) symmetry. The DSMs can be converted into other topological phases such as Weyl semimetal (WSM) by breaking either time-reversal symmetry (TRS) or inversion symmetry (IR), which leads to the splitting of Dirac point into two non-degenerate Weyl points. Unlike Dirac and Weyl fermions with four-fold and two-fold band degeneracy, many other new fermions have been predicted in materials with higher-fold band degeneracy. Due to their distinctive bulk band structure, the TSMs have been shown to exhibit exotic physical properties such as giant magneto-resistance, Fermi arc surface states, high mobility, non-trivial Berry phase, chiral anomaly induced negative magneto-resistance, etc. In topological materials, bulk conductivity often overwhelms the surface state's contribution, complicating the explicit interpretation of the observed effects electronically. Increasing the surface to volume ratio thus offers the possibility to enhance the contribution of the topological surface states to the conductivity. Therefore, the fabrication of thin films is an effective technique to reduce the bulk contribution by increasing the surface-to-volume ratio.

This thesis presents the growth and magneto-transport investigation of non-trivial states of some low-dimensional topological materials. These materials include the topological semimetal candidates $Pd_3Bi_2S_2$, $PdSb_2$, $Pd_3Bi_2Se_2$, and topological semimetal $Co_3Sn_2S_2$. Our work on these materials reveals several exciting results: (i) observation of 2D weak anti-localization in thin films of topological semimetal $Pd_3Bi_2S_2$, indicating for the first time the contributions from two dimensional (2D) topological surface states,(ii) observation of two dimensional Dirac fermions in thin films of topological candidate $Pd_3Bi_2Se_2$, (iii) Comparative study of weak anti-localization and electron-electron interaction effect in thin films of topological semimetal candidate $PdSb_2$, giving an alter-

nate way to gain information about the coupling between the topological surface states and bulk states, (iv) observation of planar Hall effect below the ferromagnetic ordering temperature in $Co_3Sn_2S_2$, indicating that planar Hall effect can't be connected with the topological character of $Co_3Sn_2S_2$.

List of publications:

1. *2D weak anti-localization in thin films of topological semimetal $Pd_3Bi_2S_2$.*
   Shama, R.K. Gopal, Goutam Sheet, and Yogesh Singh.
   Sci. Rep. 11, 12618 (2021).

2. *Observation of planar Hall effect in the ferromagnetic Weyl semimetal $Co_3Sn_2S_2$.*
   Shama, R. K. Gopal, and Yogesh Singh.
   J. Magn. Magn. Mater. 502, 166547 (2020).

3. *Unusual Magnetotransport from two-dimensional Dirac Fermions in $Pd_3Bi_2Se_2$.*
   Shama, Dinesh Kumar, Goutam Sheet, and Yogesh Singh.
   Physica E Low Dimens. Syst. Nanostruct. 144, 115457 (2022).

4. *The observation of Weak Antilocalizaion in thin films of topological semimetal candidate $PdSb_2$.*
   Shama, Aastha Vasdev, Dinesh Kumar, Goutam Sheet, and Yogesh Singh.
   arXiv preprint arXiv:2202.01527

5. *Rotating magnetocaloric effect in the ferromagnetic Weyl semi-metal $Co_3Sn_2S_2$.*
   Anzar Ali, **Shama** and Yogesh Singh.
   J. Appl. Phys. 126, 155107 (2019).

6. *Domain structure evolution in the ferromagnetic Kagome-lattice Weyl semimetal $Co_3Sn_2S_2$.*
   Sandeep Howlader, Ranjani Ramachandran,**Shama**, Yogesh Singh, Goutam Sheet.
   J. Phys.: Condens. Matter 33, 075801 (2021).

7. *Observation of Shubnikov–de Haas Oscillations, Planar Hall Effect, and Anisotropic Magnetoresistance at the Conducting Interface of EuO–KTaO3.*

Nand Kumar, Neha Wadehra, Ruchi Tomar, **Shama**, Sanjeev Kumar, Yogesh Singh, Sushanta Dattagupta, Suvankar Chakraverty.
Adv. Quantum Technol., 4: 2000081 (2021).

Contents

List of Figures

List of Tables

CHAPTER 1

General Introduction

1.1 Integer Quantum Hall effect

Band theory has been extremely successful in arranging a wide variety of materials in two types: metals and insulators. These are classified in accordance with the energy gaps between the conduction and valence bands. In metals, the Fermi level lies in the conduction band. In an insulator, the Fermi level lies in a gap between the conduction and valence band, which is larger than the energy gap of semiconductors. One can convert an insulator into a semiconductor by tuning the Hamiltonian without closing the energy gap. This defines the topological equivalence between two insulating states. But some insulating states can't be transformed into each other without closing the gap, despite having the same symmetries. Such insulating states are topologically distinct [1].

In mathematics, topology is mainly concerned with geometrical properties of objects, which are invariant under continuous deformations such as bending, crumpling, pressing but not tearing or gluing. These properties are called topological invariants [2]. For example, a coffee mug can be transformed into a doughnut under continuous deformations, so they have similar topological invariants. But a doughnut can't be converted into a sphere under continuous deformations, so these two have different topological invariants. The topological invariants are classified by genus 'g,' which accounts for no. of holes. Acc. to the Gauss-Bonnet theorem,

genus 'g' is defined as

$$\frac{1}{2\pi}\int_{Surface} KdS = 2-2g, \tag{1.1}$$

where K is the Gaussian curvature. For a sphere, the integral value is 4π, which results in a zero value of g, which means no holes. Therefore, if we change a sphere into an ellipsoid, still its topological invariant remains the same. A similar concept applies to the electronic states of matter.

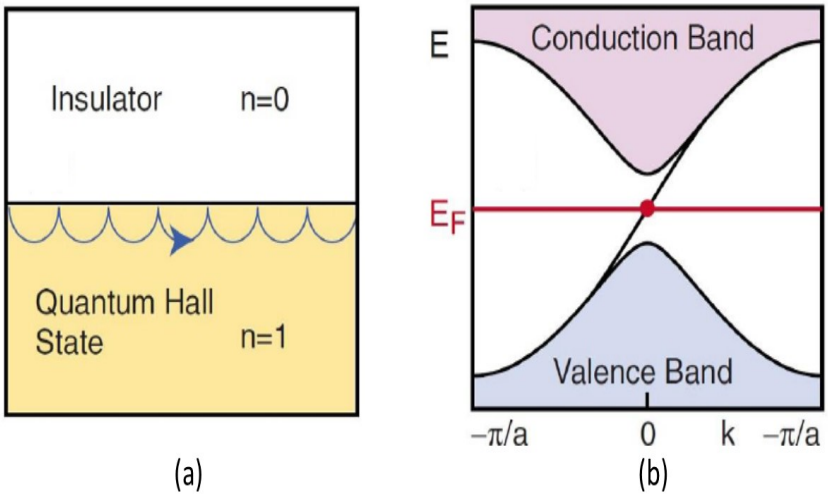

Figure 1.1: (a) A interface between a quantum Hall state and an insulator has skipping orbits, which are chiral in nature. (b) A single chiral edge state connecting the valence band and conduction band. Reprinted from **Rev. Mod. Phys. 82,3045(2010).**

Before the remarkable discovery of the integer Quantum Hall effect (QHE) in 1980 by Klaus Von Klitzing [3, 4], Ginzburg-Landau theory [5] of spontaneous symmetry breaking was used to describe the phases such as ferromagnet's (rotational symmetry breaking) and superconductors (broken-gauge symmetry). The integer quantum Hall state is the first state of matter, which doesn't have an analogous symmetry broken. The Quantum Hall effect (QHE) occurs when electrons confined to two dimensions are subjected to a strong out-of-plane magnetic field. In a magnetic field, electrons undergo cyclotron motion with frequency ω_C forming orbits. At low temperatures, cyclotron orbits get quantized, which results in the formation of Landau levels with energy $E_m = \hbar\,\omega_C\,\langle m+1/2\rangle$. The m^{th} and$(m+1)^{th}$ landau levels are separated by an energy gap of $\hbar\omega_C$. If m Landau levels are filled and others are empty, then the chemical potential lies between the filled and empty Landau levels, which is similar to that of an insulator. However, charge carriers at the edges form skipping orbits as their cyclotron orbits bounce off the edges, as shown in figure 1.1(a). This chiral motion of charge carriers under applied electric

field leads to the finite value of quantized Hall conductivity (σ_{xy}), which is given by

$$\sigma_{xy} = N\frac{e^2}{h} \tag{1.2}$$

where N is the filling factor, the quantization of σ_{xy} can be measured to 1 part in 10^9 [6]. The edge states appear at the interface of a trivial insulator, and Quantum Hall states are Chiral because they can flow only along one particular edge, as shown in fig. 1.1(b). These chiral edge states are immune to impurities as states required for backscattering are absent.

Later, the difference between a normal insulator and quantum Hall state was explained by Thouless, Kohmoto, Nightingale, and den Nijs (TKNN) [1]. These states are distinguished by a topological invariant n $\in$ Z (Z denotes the integers) called Chern invariant. The Chern invariant can be understood in terms of the Berry phase. The Berry phase is a geometrical phase acquired by a quantum state over a cycle during an adiabatic process [7]. The Bloch states $|u_m(k)>$, the eigenstates of Hamiltonian H(k), under gauge transformation are given by $|u_m(k)> = \exp^{i\phi(k)}|u_m(k)>$, where k is crystal momentum in reciprocal space. Under gauge transformation, A_n transform as $A_n + \nabla\,\phi$(k), which is known as the Berry connection or the Berry vector potential. For a closed path C, Berry phase in momentum space can be expressed as

$$\gamma_c = \oint_C A_m.dk \tag{1.3}$$

In analogy to electrodynamics, it is useful to define a gauge field tensor in terms of Berry vector potential, $F_m = \nabla_k \times A_m$. Therefore according to stokes theorem, the Berry phase can be written as

$$\gamma_c = \int_S (\nabla_k \times A_m).d^2k = \int_S F_m d^2k \tag{1.4}$$

The Chern invariant in terms of berry flux in the Brillouin zone is given by

$$n_m = \frac{1}{2\pi}\int d^2k F_m \tag{1.5}$$

The Chern number is invariant provided gaps separating the occupied and unoccupied band remain finite. The TKNN showed that quantum Hall conductivity could be rewritten in Chern invariant over the entire Brillouin zone. The n = 0 value of the Chern invariant represents a trivial insulator (n = 0) and n = 1 represent a quantum Hall state (n=1). To change the value of a topological invariant, a gap has to

close somewhere between the quantum Hall state and trivial insulator. Therefore, the transformation of the Hamiltonian from a trivial insulator to a quantum Hall state is not smooth.

1.2 Quantum spin Hall state and 3D topological insulators

The realization of quantum Hall state (QHE) requires a very high magnetic field, which limits its applications. The question arises whether a magnetic field (breaks time-reversal symmetry) is necessary to obtain the topological state. Murakami, Nagaosa, and Zhang suggested the occurrence of QHE by the internal spin-orbit coupling [8]. Kane and Mele (2005), as well as Bernevig and Zhang(2006), had provided the theoretical prediction of the existence of the time-reversal invariant topological state, called as Quantum spin Hall insulator (QSH) [9, 10]. In a QSH, the internal spin-orbit coupling will act as an effective magnetic field (B_{eff}) which is opposite for up (↑) and down (↓) spin electrons. The spin (↑) electrons would be chiral, with conductance in fractional multiples of $\frac{e^2}{h}$, while spin (↓) electrons would be anti-chiral, with conductance in fractional multiples of -$\frac{e^2}{h}$, as shown in fig. 1.2(c). Therefore, the QSH state can be viewed as two copies of a QH state with opposite spins, as shown in fig. 1.2(a). The effective Hamiltonian for QSH edge state is given by

$$H = \hbar v_f \sigma_x k_y \tag{1.6}$$

where v_f is the Fermi velocity, σ_x is Pauli spin matrix x-component, k is the reciprocal lattice vector. Also, the QSH state is known as a 2D topological insulator.

In QSH, spin non-degenerate edge states are immune to backscattering by non-magnetic impurities. The reason is when a spin (↑) electron backscatters by an impurity, it acquires a phase of π. Similarly, spin (↓) electron acquires a phase of -π during backscattering. This leads to destructive interference of reflected wave functions, which allows a perfect transmission. However, this scenario works only for the odd no. of propagating channels. This odd-even effect was pointed out by Qi and Zhang [11]. If the impurity were magnetic, time-reversal symmetry is broken. As a result, perfect destructive interference is no longer possible, and backscattering would be allowed. Naively, one can propose a topological invariant (TKNN) for QSH similar to the QH state. one can define the TKNN invariant as $n_\uparrow$ for up spin electrons and $n_\downarrow$ = -$n_\uparrow$ for down spin electrons. This implies the zero value of the

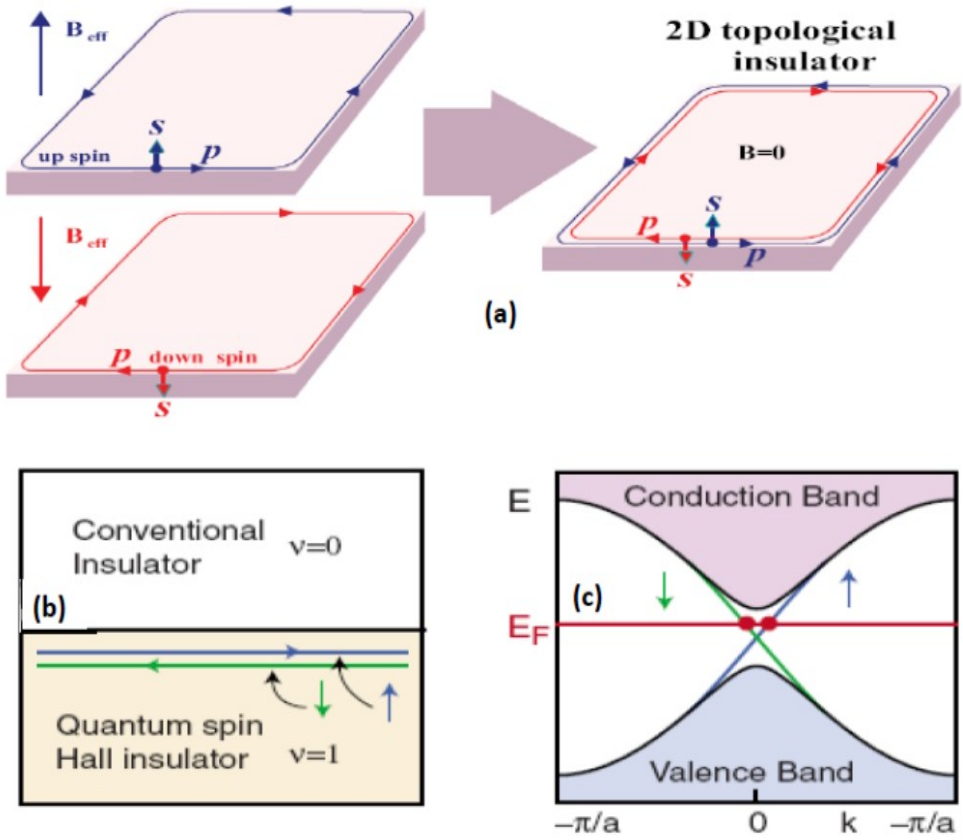

Figure 1.2: (a) A quantum spin Hall state consists of two copies of quantum Hall state. (a) Reprinted from **G. Tkachov, Topological insulators: The physics of spin helicity in quantum transport (Pan Stanford, 2015).**(b) Chiral Edge states at the interface between QSH insulator and a trivial insulator. (c) The chiral edge state dispersion, in which up (blue arrow) and down spins(green arrow) moves in opposite directions. (b), (c) Reprinted from **Rev. Mod. Phys. 82,3045(2010).**

TKNN invariant for the QSH state. For QSH state, a new topological invariant was mathematically formulated by kane (2005), Fu (2006), and others [12, 13]. The topological invariant is defined as

$$(-1)^{\nu} = \prod_{r=1}^{4} \delta_a \tag{1.7}$$

where δ_a is given by

$$\delta_a = \frac{\sqrt{det[S(\Gamma)]}}{Pf[S(\Gamma)]} \tag{1.8}$$

The $\nu = 0$ value represents a trivial insulator and $\nu = 1$ represents a QSH insulator, as shown in fig. 1.2 (b). The QSH state was first observed experimentally in HgTe/(Hg, Cd)Te quantum wells (QWs) [14].

In 2007, Fu. *et al.* had theoretically predicted the existence of a 3D analog of QSH insulator, which is known as a three-dimensional topological insulator (3D TI) [15]. The 3D topological insulators can be constructed by stacking layers of the 2D quantum spin Hall insulator. The 3D topological insulators have insulating bulk and gapless conducting surface states protected by time-reversal symmetry. These 2D surface states disperse linearly in all three directions. The conducting surface states have a spin momentum locking property which arises due to spin-orbit coupling, as shown in fig. 1.3(a). The spin momentum locking results in the helical nature of surface states, as shown in fig.1.3(b). The Hamiltonian for a 3D topological insulator is given by

$$H = \hbar v_f(\sigma_x k_y - \sigma_y k_x) \tag{1.9}$$

where v_f is the Fermi velocity, σ_x,σ_y are the components of Pauli spin matrix, k is a reciprocal lattice vector. In 2008, Hsieh *et al.*(2008) reported the discovery of the surface states experimentally in $Bi_{1-x}Sb_x$ alloy using the angle-resolved photo-emission spectroscopy (ARPES) [16]. The surface structure of $Bi_{1-x}Sb_x$ is quite complex, and the bandgap is also very small. Therefore a search began for new materials with a more significant bandgap and a much simpler surface. This led to the discovery of the second generation of 3D topological insulator materials such as Bi_2Se_3, Bi_2Te_3 etc [17, 18]. having a single Dirac cone. Unlike QSH insulator, 3D topological insulators are characterized by four topological invariants (ν_o,ν_1,ν_2,ν_3). Each invariant can take binary values 0 and 1, which leads to sixteen possible topological phases. A 3D topological insulator with $\nu_o = 0$ is referred as a weak 3D topological insulator. The ν_1,ν_2,ν_3 are the miller indices's, which describe the orientation of layers. The $\nu_0 = 1$ refers to a distinct phase, which is called

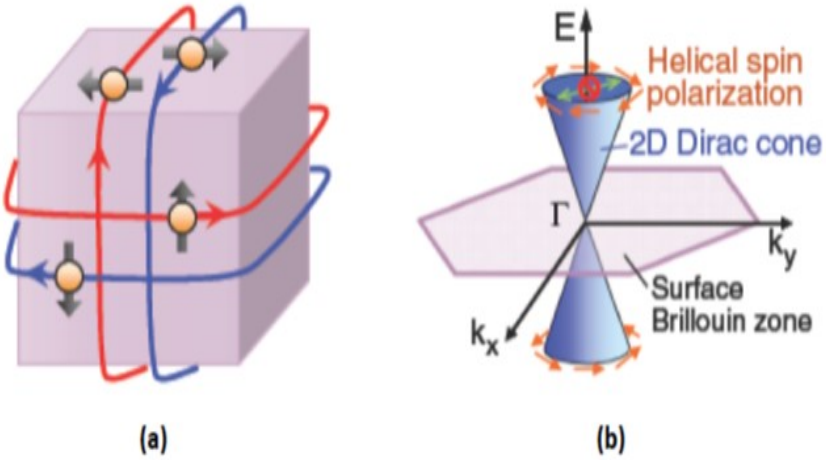

Figure 1.3: (a) Schematic representation of spin momentum locked surface states of 3D TI in real space. (b) Energy dispersion of surface states forming a 2D Dirac cone. Reprinted from **Journal of the Physical Society of Japan 82, 102001 (2013).**

a strong 3D topological insulator. ν_0 describes the no. of Kramer's points enclosed by the Fermi surface. In a 3D strong topological insulator, an odd no. of Kramer's degenerate points are enclosed by the Fermi surface. The surface electronic structure of a topological insulator is very similar to graphene, but rather than four Dirac points, it contains only one Dirac point.

1.3 Topological Semimetal

The discovery of a topological insulator in two and three dimensions has stimulated the search for new topological phases of matter. Topological semimetals (TSM) are the gapless electronic phases which exhibit topologically stable band crossings. The degeneracy of band crossings gives rise to distinct topological semimetal phases such as Dirac or Weyl semimetals, and beyond these [19, 20, 21, 22, 23]. In the beginning, TSMs were mainly considered as an intermediate phase between normal insulators (NIs) and topological insulators(TI). Unlike the topological insulators, there is an inversion symmetry (IS) which plays a vital role in addition to time-reversal symmetry (TRS). When the inversion symmetry (IS) is broken, gapless points can appear in pairs during the transition NI-to-TI, while for systems with inversion symmetry, the gap can close only at one k-point. Due to their distinctive bulk band structure, the TSMs have been shown to exhibit exotic physical properties such as giant magnetoresistance, non-Ohmic transport, Fermi arc surface states, high mobility, chiral anomaly induced negative magnetoresis-

tance, etc [24, 25, 26].

1.3.1 Dirac Semimetal

3D Dirac semimetals can be seen analogous to 2D graphene, with the Dirac bands dispersing linearly in all three k-directions. 3D Dirac cones were predicted to exist accidentally in many materials. 3D Dirac semimetals can be occurred at an intermediate point between the transition of topological insulators and ordinary insulators by tuning several parameters such as chemical composition, lattice constant, etc. The intermediate point is called a quantum critical point. Here, the main tuning parameter for this transition is spin-orbit coupling. By tuning the spin-orbit coupling, conduction and valence bands touch each other at a quantum critical point, as shown in fig 1.4, and the electronic band structure in bulk is described by 3D massless Dirac fermions [27, 28]. Below and above this tuning parameter, there exists a bulk bandgap that is inverted on one side w.r.t the other side. Specifically, the band crossing of these two bands leads to degeneracies, which occur at discrete points in the Brillouin zone (BZ). For the massless Dirac Fermions, Hamiltonian is given by

$$H\psi = \begin{pmatrix} \hbar v_F \sigma.k & 0 \\ 0 & -\hbar v_F \sigma.k \end{pmatrix} \psi \tag{1.10}$$

where v_F, σ and k represent the Fermi velocity, Pauli matrices, and momentum vector, respectively, since Pauli matrices are 2 $\times$ 2 matrices, Hamiltonian is a 4 $\times$ 4 matrices. However, such accidentally formed Dirac semimetals are not stable since they need fine-tuning, and a small perturbation may open a gap at the Dirac point. Experimentally, a 3D DSM state at a quantum critical point was realized in the number of compounds such as $BiTl(S_{0.5}Se_{0.5})_2$, $(Bi_{0.94}In_{0.06})_2Se_3$, etc [29, 30]. However, the Dirac point in this type of semimetal is unstable. It has been theoretically predicted that in a material with strong spin-orbit coupling and both time-reversal and inversion symmetry, if additional crystal symmetries such as crystalline rotational symmetries are present, the spin-orbit coupling may open a band-gap at all momenta except at special momenta along with the symmetry axis [19, 22, 31]. The protected degeneracy of conduction and valence band leads to the advent of 3D Dirac fermions in the materials. These Dirac fermions have been realized in Cd_3As_2 and Na_3Bi, which are robust against perturbations protected by crystal symmetries [20, 32].

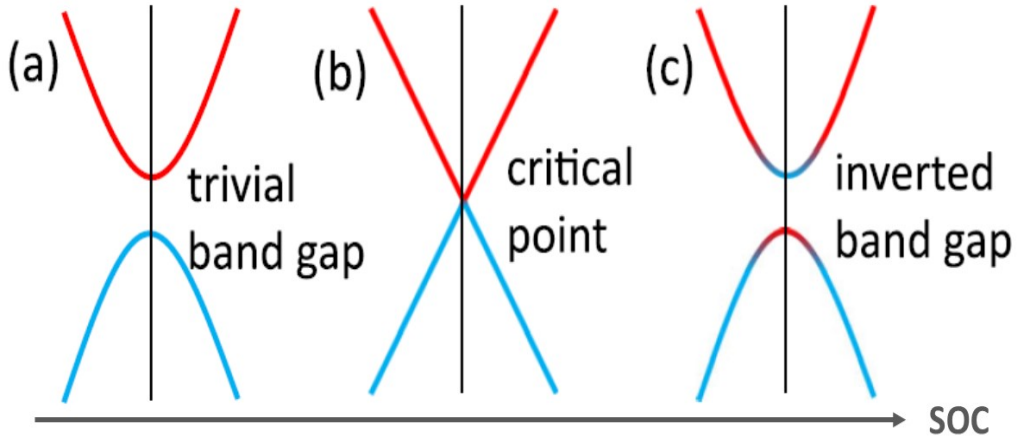

Figure 1.4: A 3D Dirac semimetal state can be realized by tunning spin orbit coupling of a system to the critical point in between a trivial insulator and topological insulator. Reprinted from **Science 347,294 (2015).**

1.3.2 Weyl Semimetals

In 1929, Weyl further simplified the Dirac equation (1.10) and proposed a new Hamiltonian for Weyl fermions[33] :

$$H\psi = \pm c\vec{\sigma}.\vec{p} \tag{1.11}$$

The above equation describes a right (left) moving particle known as chiral or Weyl fermions. In Weyl fermions, spin is projected either parallel or anti-parallel to the momentum vector, which defines their chirality. The TSMs containing Weyl fermions are known as Weyl semimetals. Like Dirac semimetals, Weyl semimetals also can be observed at a quantum critical point between the transition of topological insulators and ordinary insulators. Both Dirac and Weyl semimetals differ only in symmetry. Figure 1.5 shows the conversion of Dirac Semimetal to Weyl semimetal by breaking either inversion or time-reversal symmetry. In Weyl Semimetals, conduction and valence band touch each other at discrete points in the Brillouin zone.

The primary determining condition of such band touching is the degeneracy of bands, which is determined by symmetry. If time-reversal symmetry is broken and inversion is preserved, this allows the minimal no. of Weyl nodes at the same energy, i.e., two Weyl nodes of opposite chirality.

The time-reversal symmetry can be broken by applying an external magnetic

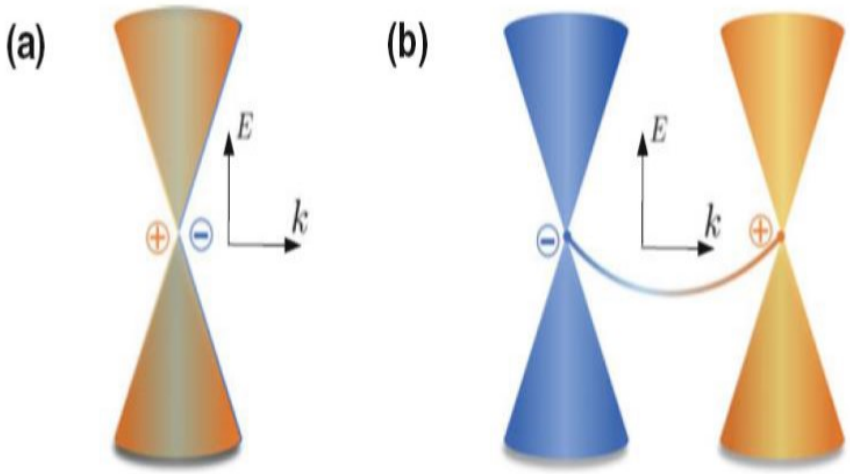

Figure 1.5: (a) Dirac semimetal with degenerate positive and negative chiralities fermions. (b) Weyl semimetal with positive and negative chiralities fermions are at different positions in k - space. Reprinted from **Topological Insulators (Springer, 2017).**

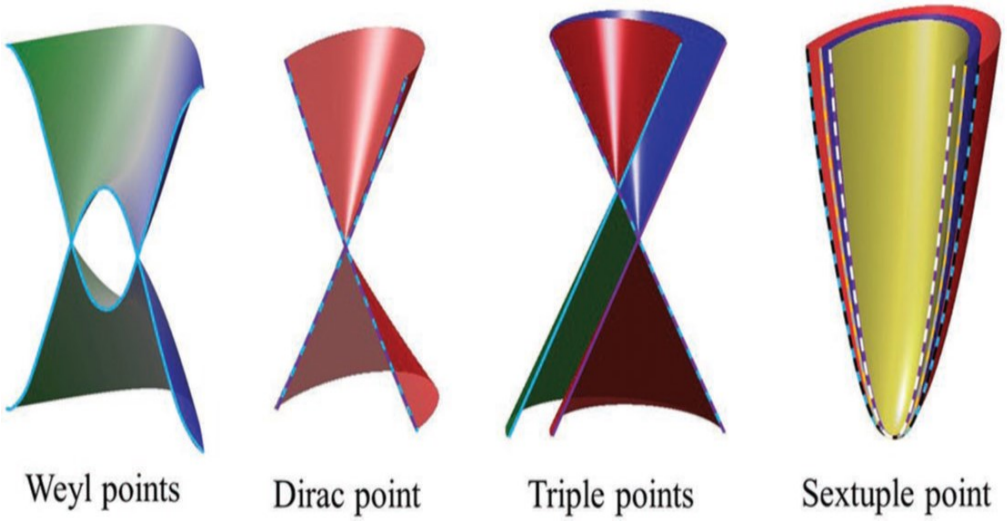

Figure 1.6: Schematic representation of Weyl, Dirac, triple, and sextuple points. Reprinted from **Adv. Mater. 2020, 32, 1906046.**

field or adding a magnetic impurity. If inversion symmetry is broken and time-reversal is preserved, the only difference comes in no. of Weyl nodes which must be in multiples of four [19]. Another topological explanation of Weyl nodes can be given in terms of Berry curvature. The Bloch electron experiences a vector potential $A(k) = i< u(k)| \nabla_k | u(k) >$ which is caused by the curvature of the k-space similar to the vector potential in the Electromagnetism. The vector potential also corresponds to a field $F(k) = \nabla_k \times A(k)$. If we do a surface integral over the entire Fermi surface enclosing a Weyl node, we will observe the following :

$$\oint F(k).dS(k) = \chi \tag{1.12}$$

This result suggests that we can treat a Weyl node just like a magnetic monopole, but this monopole generates the so-called Berry curvature in the momentum space. In addition, F(k).dS(k) is the Chern flux that passes through an infinitesimal area in the momentum space, and the closed surface integral yields Chern number χ, a topological number. Each Weyl node contributes a Chern number which implies the net-zero Chern no. of Weyl semimetals. Also, Weyl nodes are immune towards disorder, can vanish only by annihilation with another node of opposite chirality. These Weyl nodes have been predicted to observe in TaAs, TaP, NbAs, NbP materials [23, 34]. The Weyl nodes have been observed experimentally for the first time in TaAs by Angle-resolved photo-emission spectroscopy (ARPES) [35, 36].

1.3.3 Beyond the Dirac and Weyl fermions

The prediction and realization of Dirac and Weyl fermions in many materials has stimulated the research of other exotic fermions in condensed matter physics. The Weyl and Dirac fermions have their counterparts in high-energy physics that are constrained by Poincaré symmetry. In high-energy physics, the constraint of Poincaré symmetry significantly limits the occurrence of new particles. In condensed matter physics, the fermions are only required to satisfy the 230 space group symmetries, leading to a new type of fermions with no high-energy counterparts. Unlike Dirac ad Weyl fermions with four-fold and two-fold degeneracy, many other new fermions have been predicted in materials, which have three, six, eight-fold degenerated fermions as shown in fig 1.6. The higher-fold degenerated fermions have been predicted by density functional calculations (DFT) [37, 38, 39, 40]. These fermions have been experimentally realized in many materials such as MoP, CoSi, AlPt [41, 42, 43, 44].

1.4 Magnetotransport in Topological Semimetals

1.4.1 Large transverse unsaturated Magnetoresistance and High mobility

Magnetoresistance (MR) is a versatile experimental probe in analyzing electronic properties of various materials, such as carrier density (n), mobility (μ), and the nature of scattering and disorder. Magnetoresistance (MR) is defined as a change of resistivity under magnetic field normalized by zero-field resistivity (MR = [R(B) - R(0)]/R(0)). In typical non-magnetic and semi-conducting materials, the MR increases quadratically with the magnetic field applied transverse to current and saturates to a constant value when the product of the applied field and the mobility (μ) approaches unity [45]. However, Dirac and Weyl semimetals exhibit large unsaturated magnetoresistance (MR) when the magnetic field is applied transverse to the current direction. It has been observed that MR can reach up to 10^6 at low temperatures (below 2 K) and high magnetic fields [46, 47]. Non-saturating MR is commonly attributed to the semi-classical two-band model. Two band model is widely used to describe the longitudinal resistivity given by,[48]

$$\rho_{xx} = \frac{1}{e}\frac{(n_h\mu_h + n_e\mu_e) + (n_e\mu_e\mu_h^2 + n_h\mu_h\mu_e^2)B^2}{(n_h\mu_h + n_e\mu_e)^2 + (n_h - n_e)^2(\mu_h\mu_e)^2B^2} \tag{1.13}$$

Where $n_{e(h)}$ and $\mu_{e(h)}$ are carrier density and mobility of electrons and holes, respectively. When n_h and n_e are nearly compensated and mobility is very high, equation (1.13) results in a non-saturating quadratic magnetoresistance. The electron and hole carriers compensation results in rich magneto-transport properties, which have a strong temperature and applied transverse magnetic field (B) dependence in nonmagnetic compounds. The high mobility in TSMs can be understood in terms of relation with relaxation time τ and effective mass as $\mu = e\tau/m$.

In the case of Dirac and Weyl fermions, massless behavior is expected due to linear dispersion. The effective mass in TSMs can be calculated by quantum oscillations either in resistivity or magnetization. A very small value of effective mass has been observed in several topological semimetals [49, 50]. The non-trivial band topology of Dirac fermions suppressed the backscattering, which resulted in a large relaxation time(τ). Therefore, a small value of effective mass and large relaxation time leads to high mobility in TSMs. Thus, high purity samples are required to realize electron-hole compensation and high mobility, both of which will enhance mag-

netoresistance. Also, large linear MR could be observed in topological semimetals and other materials. The linear MR has been observed firstly in disordered Silver chalcogenides $Ag_{2+\delta}$ Se and $Ag_{2+\delta}$Te. This could be explained by two main theoretical mechanisms: (i)"quantum linear MR," which emerges in systems with linear band crossings when the lowest Landau level is occupied (ii) linear magnetoresistance results from large spatial fluctuations in the conductivity of the material, due to the inhomogeneous distribution of ions [51, 52]. Linear magnetoresistance has been observed in several TSMs such as TaP_2,$Co_3Sn_2S_2$,$PtTe_2$ [53, 54, 49].

1.4.2 Chiral anomaly

In 1969, a Chiral anomaly was discovered for relativistic fermions[55, 56]. However, it gained interest in recent years in physical systems such as Dirac and Weyl semimetals in condensed matter. This re-occurrence of interest is due to the recent understanding that chiral anomaly can lead to new anomalous transport phenomena in the presence of electromagnetic fields, which was realized firstly by Nielson and Ninomiya [57]. The chiral anomaly in condensed matter physics is called as an analog of Adler-Bell-Jackiw anomaly in particle physics. The Chiral anomaly is responsible for pumping the electrons between the nodes of opposite chirality in the case of Weyl semimetals in the presence of electric and magnetic fields, as shown in fig. 1.7, which can be understood via the equation:[19]

$$\frac{dn^{3D}_{R/L}}{dt} = \pm\frac{e^2}{h^2}E.B \tag{1.14}$$

where 3D reminds us that we are dealing with 3D Weyl fermions, R and L represents the right and left nodes, respectively. This equation suggests that the conservation of carrier density at an individual Weyl node depends on an angle between the magnetic field and the electric field. The non-conservation of charge carriers between the opposite Weyl nodes is maximum when electric and magnetic fields are parallel, which leads to extra flow of current in the direction of the applied electric field and results in negative longitudinal magnetoresistance (NMR). The NMR is suppressed as an angle between B and E increases. It was observed experimentally firstly in Dirac semimetal $Bi_{1-x}Sb_x$ for x $\approx$ 0.03 [58]. This was interpreted as a signature of Weyl semimetal, as Dirac Cone splits into Weyl nodes with opposite chirality on symmetry breaking either inversion or time-reversal. Chiral anomaly has been observed in several TSMs such as TaAs, NbP, Na_3Bi, $ZrTe_5$ [23, 59, 60, 61]. However, NMR may also appear due to other mechanisms such as current jetting

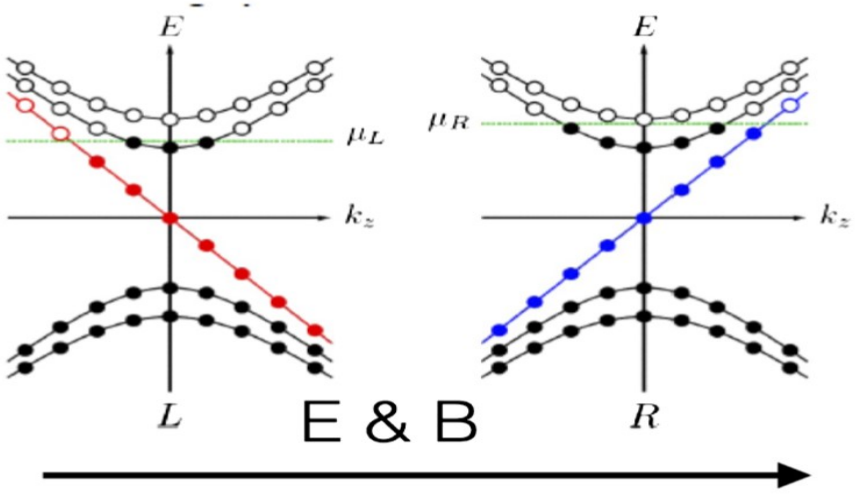

Figure 1.7: Spectrum in a magnetic field along the z axis displaying Landau levels that disperse along the field. The zeroth Landau levels are chiral. In addition, an electric field along z generates valley imbalance. Reprinted from **Rev. Mod. Phys., Vol. 90, No. 1,(2018).**

[62]. The current jetting mainly occurs due to the inhomogeneous current distribution in the magnetic field. This effect is strong in the materials that own large resistance anisotropy induced by the magnetic field [63]. The current jetting effect can be minimized by using a perfect bar shape single crystal with collinear and well-separated voltage contacts. In addition to NMR, the chiral anomaly may also result in another transport signature, which is an unconventional Hall effect, known as the planar Hall effect (PHE) [64].

1.4.3 Anomalous Hall effect

In addition to the Chiral anomaly, there is another phenomenon that makes topological semimetals interesting. In 1879, Edwin H. Hall discovered that the Lorentz force due to the external magnetic fields leads to accumulation of charges on one side, causing the conventional Hall effect. However, in ferromagnetic materials, a spontaneous Hall effect occurs in the absence of external magnetic fields, called the anomalous Hall effect. The origin of AHE has been a puzzle for many years. In 1954, Karplus and Luttinger (KL) proposed a theory for the anomalous Hall effect (AHE) that the electrons acquire an additional contribution to their group velocity when an external electric field is applied to a solid [65]. This anomalous velocity was perpendicular to the electric field and could contribute to the Hall effects. Later, KL theory was combined with the Berry phase, resulting in a new explanation for

AHE [66, 67]. The Intrinsic anomalous Hall conductivity due to velocity correction can be calculated by integrating the Berry curvature over the Brillouin zone and summed over all the occupied bands [68]. The Berry curvature can be called Berry flux. The topological features of the electronic band structure of TSMs lead to a large accumulation of Berry curvature, which results in additional contributions such as anomalous velocity.

Instead of the Berry phase, several other extrinsic mechanisms are proposed to be responsible for AHE, such as the side jump mechanism and skew scattering [69, 70]. Considering all the contributions, anomalous Hall conductivity is given by

$$\rho_{xy}^{AH} = \rho_{xy}^{int} + \rho_{xy}^{ext} \tag{1.15}$$

In general, both contributions are present and are of the same order of magnitude, making it very difficult to disentangle the intrinsic and extrinsic contributions experimentally. In a Weyl semimetal, it was proposed that the extrinsic part is absent [71]. The current due to the AHE is

$$J = \frac{e^2}{2\pi^2} b \times E \tag{1.16}$$

where b is the splitting vector and E is the electric field. The AHE is particularly interesting in Weyl semimetal because AHE is fully determined only by the relative location and topological charge of the Weyl nodes. Since the Weyl nodes are topologically protected and can only be removed by annihilating two opposite chirality nodes, the AHE current is also topologically protected in Weyl semimetals. AHE has been observed experimentally in various Weyl semimetals such as $Co_3Sn_2S_2$, $ZrTe_5$, TbPtBi [72, 73, 74].

1.4.4 Weak Anti-localization

In topological materials, the existence of topologically protected surface states that cannot be localized can be regarded as merit compared to ordinary metals [75, 76]. The two-dimensional surface states of topological materials have a helical spin structure in momentum space, giving rise to a π Berry phase when an electron moves adiabatically around the Fermi surface. The π Berry phase can lead to the absence of backscattering and further de-localization of the surface electrons [77]. In experiments, the delocalization of electrons was believed to be verified by a phenomenon named weak anti-localization [78]. This effect involves the destructive interference between time-reversed loops formed by scattering trajectories owing to

the π Berry phase [79]. The destructive interference can suppress the backscattering of electrons, which enhances conductance with decreasing temperature because dephasing mechanisms are suppressed at low temperatures [80, 81]. The quantum correction to the conductance resulting from WAL at zero magnetic fields is given as:[81, 82]

$$\Delta\sigma_{QI}(T) = \alpha p \frac{e^2}{\pi h} \ln\left(\frac{T}{T_{QI}}\right) \tag{1.17}$$

where α represents the no. of conducting channels and p is the exponent in the power-law fit of dephasing lengths. T_{QI} is a characteristic temperature at which the quantum correction vanishes. In quantum diffusion regime, the relevant length scale is phase dephasing length (L_ϕ), which is equal to $\sqrt{D\tau}$, D is Diffusion coefficient, and τ is the relaxation time. If L_ϕ > t where 't' is the sample thickness, then the quantum interference is two-dimensional, otherwise three-dimensional. Acc. to this criterion, we restrict our analysis to 2D or 3D quasi limit. A magnetic field can destroy the destructive interference as well as the enhanced conductivity, so the another signature of the weak anti-localization is a negative magneto-conductivity. For two-dimensional systems, the Hikami-Larken-Nagaoka (HLN) equation can describe weak anti-localization [78, 83]. This theory involves the contribution of quantum effects from three different mechanisms: spin-orbit coupling, elastic scattering, and electron phase coherence. In the limit of high spin-orbit coupling, the HLN equation can be written as:

$$\Delta\sigma(\mathrm{B}) = -\alpha \frac{e^2}{\pi \mathrm{h}} \left[\psi\left(\frac{1}{2} + \frac{\mathrm{B}_\phi}{\mathrm{B}}\right) - \ln\left(\frac{\mathrm{B}_\phi}{\mathrm{B}}\right)\right] \tag{1.18}$$

where α is the same parameter described in eq. 1.13, ψ is the digamma function, $\mathrm{B}_\phi = \frac{\hbar}{4eL_\phi^2}$ is the characteristic field required to destroy phase coherence. Acc. to HLN theory, the value of α is 1/2 for weak anti-localization. This value of α represents the contribution of one topological surface conducting channel. Therefore, the analysis of magneto-conductance within the HLN equation can give an insight into non-trivial behavior. Thus the weak anti-localization effect is an efficient phenomenon to identify non-trivial surface states in transport study. The weak anti-localization effect has been observed in various topological materials such as Cd_3As_2, LuPdBi, $ZrTe_5$ [84, 85, 86].

1.5 Structure of Thesis

Chapter 2 gives a brief description of the synthesis techniques used for the growth of polycrystalline and single crystalline samples such as $Pd_3Bi_2S_2$, $Pd_3Bi_2Se_2$, $PdSb_2$, and $Co_3Sn_2S_2$. This chapter also includes the description of pulse laser deposition technique used for the growth of thin films. We briefly review the characterization techniques such as energy-dispersive X-ray spectroscopy (EDX) and powder X-ray diffraction method (PXRD). The experimental setups used to measure various physical properties(magneto-transport, dc magnetization) have been discussed.

In **Chapter 3**, we have discussed the magneto-transport studies on $Pd_3Bi_2S_2$ (PBS) thin films grown by the pulsed laser deposition technique. Longitudinal resistance measurements on PBS thin films indicated a disordered metallic system. This disorder resulted in a reduced value of mobility of bulk carriers compared to single crystals, which suppressed the bulk contribution and allowed the first detection of transport contribution from topological surface states through the 2D weak antilocalization (WAL) effect. The WAL data measured for fields applied at different angles to the current direction, scaled with the perpendicular component of the field, confirmed the contribution of 2D topological surface states to the WAL. These results were satisfactorily analyzed in terms of the Hikami-Larkin-Nagaoka theory. It was found that the coefficient α deviated from the expected value of 0.5 for 2D systems with a single topological conduction channel. This indicated the contribution from additional (topological and trivial) conducting channels in the electron transport of PBS films. The dependence of the dephasing length on temperature was also anomalous. We found that this behavior can be understood by including the Nyquist electron-electron scattering and electron-phonon scattering as the phase relaxation mechanism in PBS films.

In **Chapter 4**, we discuss the growth and magneto-transport study of $Pd_3Bi_2Se_2$ thin films, revealing for the first time the contribution of two-dimensional (2D) topological surface states. The linear energy dispersion causes exceptional non-saturated linear magnetoresistance since all Dirac fermions inhabit the lowest Landau level in the quantum limit. The transverse magnetoresistance shifts from semi-classical weak-field B^2 dependence to high-field B dependency at a critical field $B^\star$. The critical field $B^\star$ increases with the increase in temperature and satisfies the quadratic temperature dependency, which is ascribed to the Landau level splitting of linear energy dispersion. The magneto-conductance has a strong cusp-like behavior at low temperatures, which is a hallmark of weak anti-localization (WAL). The 2D

Hikami-Larkin-Nagaoka (HLN) theory is used to analyze the low field magneto-conductance data, suggesting multiple topological conduction channels. It is also found that electron-phonon scattering also contributes to the phase relaxation mechanism in $Pd_3Bi_2Se_2$ thin films.

In **Chapter 5**, we have discussed the magneto-transport properties of $PdSb_2$ (PS) thin films. $PdSb_2$ has been proposed to consist of exotic fermions with six-fold degenerate band crossing. Previous studies have confirmed the existence of sixfold degenerate band crossings by angle-resolved photoemission spectroscopy (ARPES) and density functional theory (DFT). To have more information of non-trvial behaviour, we have grown the $PdSb_2$ (PS) thin films with different thicknesses by the pulsed laser deposition (PLD) technique. We observe a positive correction to magneto-conductivity at low temperatures, which is a signature of Weak anti-localization (WAL). The observation of WAL behaviour confirmed the contribution from the topological surface states. Using the Hikami-Larkin-Nagaoka (HLN) theory, we have extracted the dephasing length (L_ϕ). It is found that the temperature dependence of the L_ϕ cannot be described only by the Nyquist electron-electron dephasing; electron-phonon scatterings also contribute to the phase relaxation mechanism. From the WAL effect, we extract α (the number of the transport channels), which deviates from 0.5, reflecting the presence more than one topological conducting channels. On the other hand, the electron-electron interaction (EEI) effect has been observed in temperature-dependent conductivity. From the EEI effect, we extract the number of the transport channel, which are similar to that attained from the analysis of the WAL effect.

In **Chapter 6**, we have confirmed a large intrinsic anomalous Hall conductivity for our crystals comparable to the values reported previously, which provides strong evidence for the topological band structure of this compound. However, we did not observe the chiral anomaly induced negative longitudinal Magnetoresistance (NLMR) reported previously for these materials even though our crystals show a larger RRR than previously reported crystals. We pointed out that the NLMR reported previously is very small in magnitude, which is relatively weak and could be easily masked by a large orbital MR, as was observed in our measurements. It has recently been pointed out theoretically that the Planar Hall Effect (PHE) could be more direct evidence of the nontrivial band structure of a Weyl semi-metal. Therefore, we looked for and observed a large PHE for our $Co_3Sn_2S_2$ crystals. However, the temperature dependence of the PHE signal showed that the signal vanished close to the ferromagnetic T_C = 175K, which suggests that the origin of the PHE signal could be magnetic anisotropy in the ferromagnetic state rather than the Chiral

anomaly. Therefore, we concluded that most likely; the PHE can't be connected to the Topological character of $Co_3Sn_2S_2$.

In **Chapter 7**, I will summarize the research work carried out in this thesis. The present work includes the magneto-transport study, which gives information about the non-trivial behaviors of low dimensional topological materials. Such magneto-transport studies provide a path to better understand and discover the new topological materials.

CHAPTER 2

Experimental Details

This chapter deals with a brief overview of the experimental methods used during the research work. In part I, we describe the sample preparation techniques for bulk and thin film. In part II, we describe various experimental methods used for characterizing and evaluating the physical properties.

2.1 Sample Preparation

2.1.1 Method for synthesis of Bulk materials

We have prepared polycrystalline samples of $A_3M_2X_2$(A = Pd,Co; M = Bi,Sn: X = S,Se), $PdSb_2$ materials for thin film deposition and single crystals of $Co_3Sn_2S_2$, $PdSb_2$, respectively. The techniques used for their synthesis are given below:

2.1.1.1 Solid State Reaction

There are various ways to grow polycrystalline samples, such as sol-gel, auto combustion, solid-state reaction, etc. Among these, the solid-state reaction is the most widely used method for the growth of polycrystalline materials. It involves the reaction between two or more starting materials in solid form at high temperatures [87]. This growth process includes several heatings and intermediate grindings to

have a homogeneous and single-phase compound. The key steps one should follow during this reaction are as below:

- The stoichiometric amount of each reactant is weighed and mixed thoroughly using a mortar pestle. Depending upon the reactivity of reagents in air, sometimes an inert atmosphere is required for mixing.
- The homogeneously mixed powder is pressed into a pellet using 5-7 ton pressure to increase the reaction rate through a hydraulic press.
- The choice of atmosphere during heating is essential. In some cases, vacuum sealing is required before heating to avoid the formation of oxides.
- The reactivity of material with quartz tube and crucible should be known.

The polycrystalline samples of $A_3M_2S_2$(A = Pd,Co; M = Bi,Sn), $PdSb_2$ were prepared using this technique.

$Pd_3Bi_2S_2$

For polycrystalline growth of $Pd_3Bi_2S_2$, stoichiometric amounts of Pd (99.95%, Alfa Aesar), Bi (99.999%, Alfa Aesar), and S (99.99%, Alfa Aesar) were mixed thoroughly and palletized using a hydraulic press. The materials are then sealed in a quartz tube under vacuum. The quartz tube was placed in a box furnace heated to 750°C in 15 hours and kept there for 44 hours, and then followed by normal cooling.

$Pd_3Bi_2Se_2$

For polycrystalline growth of $Pd_3Bi_2Se_2$, stoichiometric amounts of Pd (99.95%, Alfa Aesar), Bi (99.999%, Alfa Aesar), and Se (99.999%, Alfa Aesar) were mixed thoroughly and palletized using a hydraulic press. The materials are then sealed in a quartz tube under vacuum. The quartz tube was placed in a box furnace heated to 1000°C in 20 hours and kept there for 48 hours, and then followed by normal cooling.

$PdSb_2$

Figure 2.1: Two table top muffle furnaces used to give heat treatment in air.

For polycrystalline growth of $PdSb_2$, amounts of Pd (99.95%, Alfa Aesar), Sb (99.999%, Alfa Aesar) in stoichiometric ratio 1:2 were mixed thoroughly and palletized using a hydraulic press. The pellet was then sealed in a quartz tube under vacuum. The quartz tube was placed in a box furnace heated to 800°C in 16 hours and kept there for 48 hours, and then followed by normal cooling to room temperature.

$Co_3Sn_2S_2$

For polycrystalline growth of $Co_3Sn_2S_2$, amounts of Co (99.999%, Alfa Aesar), Sn (99.999%, Alfa Aesar), and S (99.99%, Alfa Aesar) in stoichiometric ratio 3:2:2 were mixed thoroughly and palletized using a hydraulic press. The pellet was then sealed in a quartz tube under vacuum. The quartz tube was placed in a box furnace heated to 850°C in 17 hours and kept there for 48 hours, and then cooled to 700°C in 1 hour, followed by heating for 72 hours at 700°C.

2.1.1.2 Modified Bridgman Technique

The modified Bridgman is one of the oldest techniques used for growing single crystals. The single crystals of $Co_3Sn_2S_2$, $PdSb_2$ were grown by this technique. It involves the sealing of materials in a quartz tube and placed in a furnace for heating. For single crystal growth, a sample is cooled slowly to an appropriate temperature followed by normal cooling.

$Co_3Sn_2S_2$

For single crystal growth of $Co_3Sn_2S_2$, amounts of Co (99.99%, Alfa Aesar), Sn (99.999%, Alfa Aesar), and S (99.99%, Alfa Aesar) in stoichiometric ratio 3:2:2 were sealed in a quartz tube under vacuum. The sealed tube was placed in a box furnace heated to 1000°C and kept there for 12 hours, and then slowly cooled to 800°C over 7days. Large shiny crystals of millimeters size could be cleaved from the as-grown boule.

$PdSb_2$

For single crystal growth of $PdSb_2$, amounts of Pd (99.99%, Alfa Aesar), Sb (99.999%, Alfa Aesar) were taken in stoichiometric ratio 1:2.2 and sealed in a quartz tube under vacuum. The 10% extra of antimony was taken to recompense for the loss during heating. The sealed tube was placed in a box furnace heated to 1000°C in 6 hours and kept there for 20 hours, and then slowly cooled to 630°C in 7days. Large shiny crystals of millimeters size could be cleaved from the as-grown boule.

2.1.2 Thin Film Fabrication

Thin film is defined as a thin layer of material whose thickness varies from nanometers to a few microns. In the case of thin films, the surface-to-volume ratio is larger as compared to bulk. One of the most important advantages of thin films is growing materials that are not even stable in the bulk form. Depending upon the thickness of the thin film, its properties differ significantly from its bulk part. There are several techniques for thin film deposition, such as pulsed laser deposition (PLD), chemical vapor deposition (CVD), thermal evaporation, magnetron sputtering, sol-gel process, and molecular beam epitaxy (MBE), etc. Pulse laser deposition (PLD) is unique for depositing multicomponent compounds and complex oxides among these various techniques. A brief description of pulse laser deposition is given in the proceeding sections.

2.1.2.1 Pulse Laser Deposition

In PLD, a high-power pulsed laser is focused on a rotating target inside a vacuum chamber through a quartz window. The absorbed energy is firstly converted

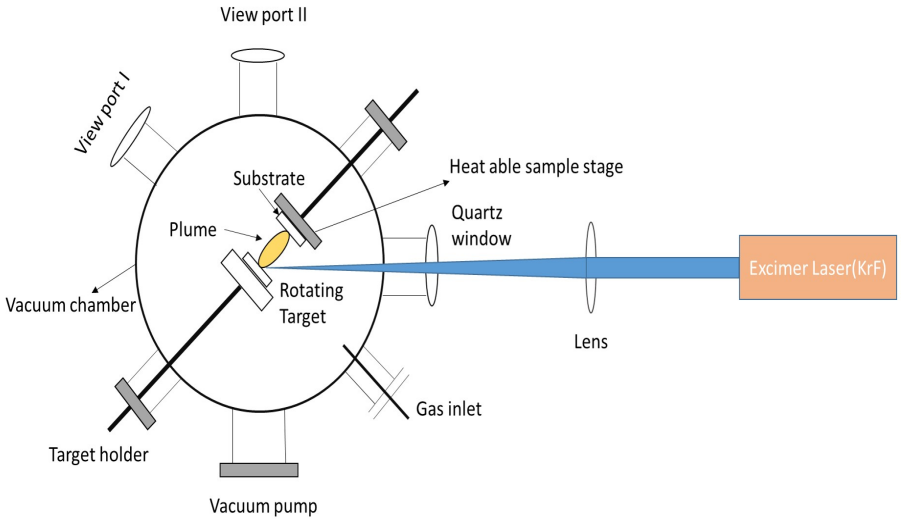

Figure 2.2: Schematic of PLD set-up used for thin film growth.

into electron excitation and then into thermal, chemical, and mechanical energy resulting in evaporation, ablation, and plasma formation. The ejected species from the target expand in the form of plasma. For stoichiometric ablation of a compound, it is necessary to have a smaller thermal diffusion length and high optical absorption coefficient at the selected laser wavelength. The thermal diffusion length is given by $l = 2\sqrt{(D\tau)}$, where τ is the laser pulse duration and D is the diffusion constant. For insulators, l is very small, so ablation of a target is mainly controlled by diffusion constant, independent of τ. For metals & semiconductors, the diffusion constant is very large, so by constraining τ to smaller values, one can reduce "l." For ablation of a target, a choice of τ can be necessary but not a sufficient condition. Each pulse must contain enough energy to heat a useful volume of a material.

In PLD, ablation of less reflective and conductive materials is most efficient. The useful wavelength range of laser lies in between 200 to 400 nm. For laser to be effective , generally excimer lasers are used, which emit radiation in UV range. Commercially available lasers are : XeF= (λ = 352 nm); XeCl (λ = 308 nm); KrF (λ = 248 nm); KrCl (λ= 22 nm); ArF(λ = 193 nm). Among these, KrF excimer is extensively used for thin film deposition by PLD.

2.1.2.2 Experimental setup of PLD

The main components of PLD system are given below :

- Deposition chamber, rotating target assembly, pump system including a roughing and turbo pump, Substrate holder with heater.

- An excimer laser for target ablation.
- Optical components to focus the laser beam on a target.

The schematic of the PLD system used for growing the thin films is shown in fig. 2.2. As discussed previously, PLD is one of the most successful techniques for growing multicomponent and complex materials. Various parameters such as laser energy density, repetition rate, substrate, target to substrate distance, substrate temperature, etc., affect the growth and properties of thin films. To obtain good quality films, we need to optimize these parameters. Despite several advantages, the PLD system has some drawbacks:

- Due to the small angular diffusion of plasma plume in PLD, it is difficult to deposit on a large area. Generally, PLD grown films are uniform over an area of 1×1 cm^2.
- Another is the splashing effect, which leads to large particulates nucleating on a thin film that causes significant surface roughness.

Using PLD, we have grown thin films of two materials $Pd_3Bi_2S_2$, $Pd_3Bi_2Se_2$, and $PdSb_2$. Target ablation was performed on polycrystalline samples of $Pd_3Bi_2S_2$, $Pd_3Bi_2Se_2$, and $PdSb_2$ using KrF excimer laser with energy density 1.8 J/cm^2. The target and substrate distance was kept at about 4-5 cm. The optimal substrate temperatures for growth of $Pd_3Bi_2S_2$, $Pd_3Bi_2Se_2$, and $PdSb_2$ thin films are 240° C, 240° C, and 120° C.

2.2 Characterization Techniques

2.2.1 Energy Dispersive Spectroscopy using Scanning Electron Microscope

A Scanning electron microscope (SEM) is an electron microscope that produces images of samples by scanning the surface with a focused electron beam. As the electron beam interacts with the sample's atoms, it generates a variety of signals that provide details about the sample's surface topography and chemical composition. An image is created by combining the position of the electron beam with the strength of the signal being detected. One of these is secondary electrons (SEs), whose mean free path in solid matter is constrained by their low energies of around 50 eV. As a result, SEs can only able to escape the top few nanometers of a sample's

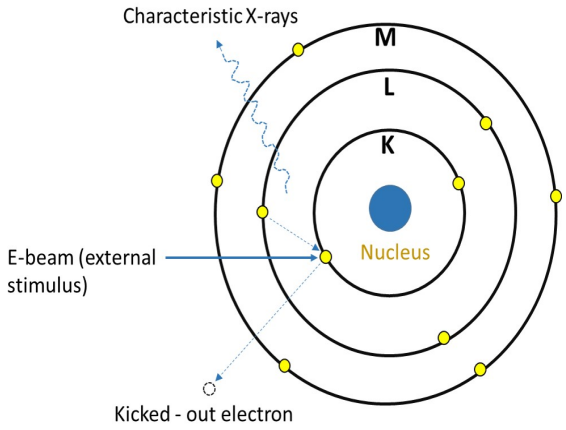

Figure 2.3: Schematic of emission of characteristic X-rays on interaction of electron beam with sample.

surface. Back-scattered electrons (BSEs) are the another beam electrons that elastic scattering causes to be reflected from the material. Since they have much higher energy than SEs, they emerge from deeper locations within the specimen, and, consequently, the resolution of BSE images is less than SE images. However, because the intensity of the BSE signal is closely connected to the atomic number (Z) of the material, BSEs are frequently utilised in analytical SEM, along with spectra derived from the distinctive X-rays. Magnification in an SEM can be controlled over a range of about 6 orders of magnitude from about 10 to 3,000,000 times. Magnification is controlled by the current supplied to the x, y scanning coils, or the voltage supplied to the x, y deflector plates. In our case, We have obtained SEM images of various samples with electron beam of energy $\approx$ 15 KeV. we have taken images at a magnification of around 25000 times.

The energy-dispersive X-ray spectroscopy (EDX) is a powerful technique used to identify the chemical composition of a sample in Scanning electron microscope (SEM) . It is based on Moseley's law, which states a direct correlation between the frequency of X-ray emitted and the atom's atomic number. This emission of X-ray is stimulated by the high-energy electron beam. During EDX analysis, a sample is bombarded by a high-energy electron beam, which results in the ejection of electrons from the atoms comprising the sample's surface. The electron vacancies are created, which are filled by electrons from a higher energy level, which leads to the emission of an X-ray whose energy corresponds to the energy difference between the two levels. There is an x-ray detector that measures the relative profusion of emitted X-rays versus energy. The spectrum of counts vs. X-ray energy is analyzed to determine the elemental composition of a sample. The schematic diagram of energy-dispersive x-ray spectroscopy is shown in Fig. 2.3.

2.2.2 X-ray Diffraction

X-ray diffraction (XRD) is a standard technique that enables us to characterize the crystal structure of a sample, i.e., thin-film and bulk. It provides information on structures, phases, preferred crystal orientation, and other structural parameters such as strain, crystal defects. X-rays of wavelength $\lambda \approx 0.5$ - 2.5 are mainly used for diffraction study because for diffraction to occur, and the wavelength must be of the order of inter-atomic spacing in crystalline materials.

In 1912, Laue had suggested that crystals could be used as a diffraction grating [88]. In 1913, W.L Bragg developed Bragg's law, which connects the observed scattering with reflections from evenly spaced parallel planes within a crystal. When X-rays are incident on a crystal, they get reflected by sets of evenly spaced parallel planes and undergo constructive interference. Bragg's condition for the observation of diffraction is given below :

$$2dsin\theta = n\lambda \tag{2.1}$$

where d indicates the spacing between crystal planes, λ specifies the wavelength of the incident X-ray beam, θ is the incident angle, and n is the diffraction order. In a powder XRD system, a monochromatic x-ray incident on a sample at an angle θ w.r.t sample surface. The motion of the detector is such that it always makes an angle of 2θ with the incident X-ray beam. The intensity detected by the detector is plotted against angle 2θ, which is analyzed to get various information.

The X-ray diffraction measurements of all samples were performed using a Rigaku Ultima high-resolution X-ray diffractometer. The XRD pattern was recorded in the angular range from 10° to 90° at a step size 0.02°. To obtain crystal information such as purity, lattice parameters, we have done Rietveld refinement using General Structure Analysis Software (GSAS) [89, 90].

2.2.3 Atomic Force Microscopy

Atomic force microscopy (AFM) is powerful imaging technique that enables us to study a sample's surface morphology by measuring the interactions between the sample surface and tip(probe). AFM consists of a tip attached to one end of a cantilever. AFM tips are made up of Si or Si_3N_4, and their size is nearly 10-20 nm. The probe motion across the surface is controlled by a feedback loop and piezoelectric scanners. Inter-atomic forces between the probe and the sample surface cause

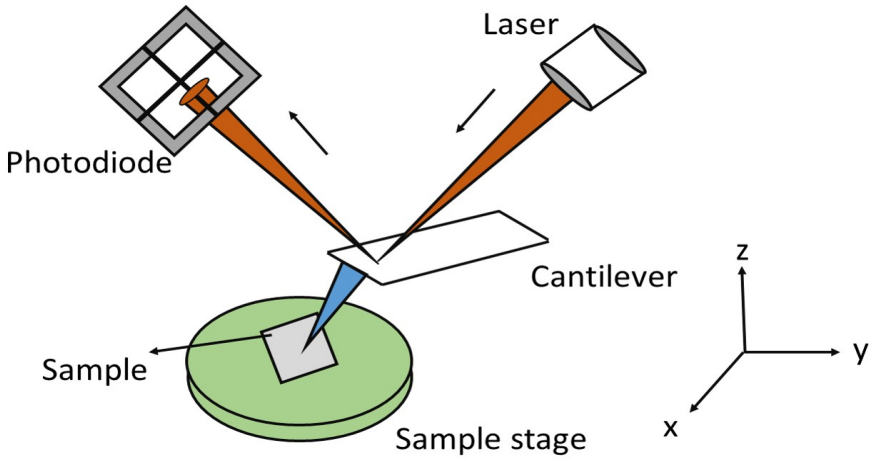

Figure 2.4: Schematic of atomic force microscopy (AFM)

the probe to deflect as the sample's surface topography or other properties change. This deflection of the probe is measured by focusing a laser on the cantilever back with a photo-diode detector. From the detector, this information is fed back to a computer, which creates a map of topography and other properties of interest. The schematic of atomic force microscopy is shown in fig. 2.4. There are different operation modes of AFM like contact, non-contact, and tapping modes. In our case, we used non-contact to map the topography of samples.

2.3 Physical Property Measurement

After synthesis and characterization of materials, we have studied physical properties using a physical property measurement system designed by Quantum Design, as shown in fig. 2.5.

2.3.1 Vibrating Sample Magnetometer (VSM)

The vibrating sample magnetometer (VSM) is designed to probe the magnetic properties of solids. The VSM consists of a non-magnetic sample holder, a linear motor transport to have sinusoidal motion of sample, pickup coil for magnetic flux detection, and electronics to control the linear motor transport and measure the response from pick up coil as shown in fig. 2.6. The VSM basically works on the principle of Faraday's law of induction [91]. In the VSM, the magnetic sample oscillates sinusoidally inside a pickup coil, which produces an electromotive current in the pickup coil, which is proportional to the magnetization of the magnetic

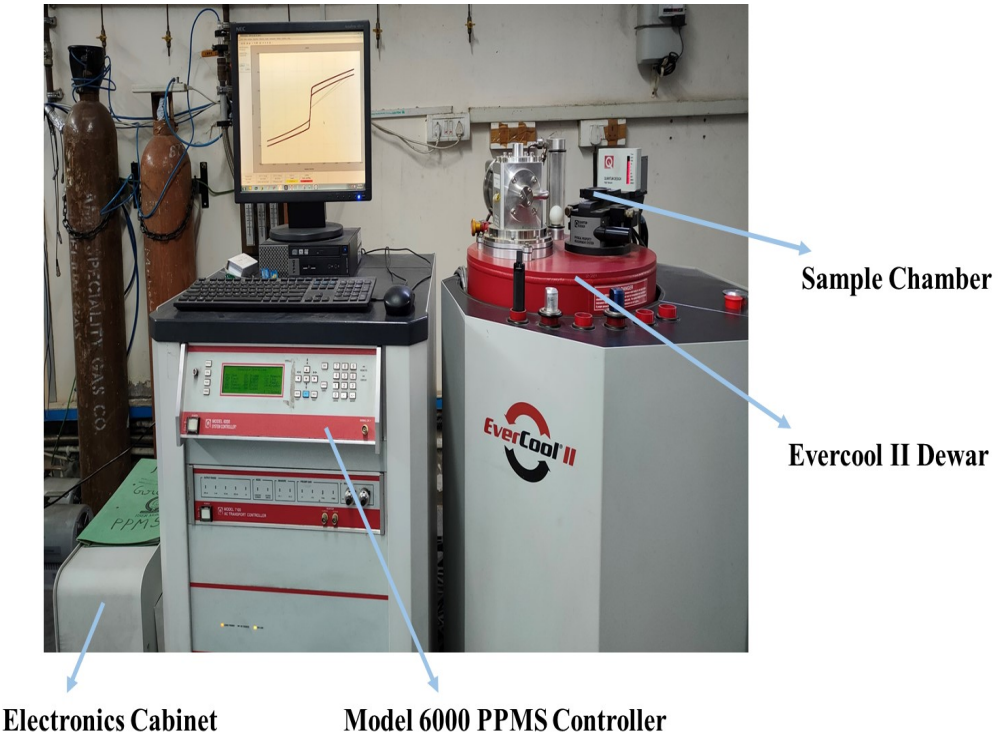

Figure 2.5: Quantum Design (QD) Physical Property Measurement System (PPMS)

sample. The time-dependent voltage induced in the pickup coil is given by the following equation:

$$V_{coil} = \frac{d\phi}{dt} = \frac{d\phi}{dz}\frac{dz}{dt} \tag{2.2}$$

where ϕ is the magnetic flux confined by the pick-up coil, z is the vertical position of the sample, and t is the time. By using a compact gradiometer pick-up coil, a linear motor operating at 40 Hz, this system can resolve magnetic moment changes of up to 10^{-6} emu at a data rate of 1 Hz. We have used the VSM option of PPMS designed by Quantum design to measure the magnetization of all samples [92].

2.3.2 Electrical Resistivity

Resistivity measurement is a simple method to have information about the electrical properties of materials. Two probe and four-probe measurements are mainly used for measuring resistivity. Among these two, the four-probe technique is more sensitive as it reduces the contribution of leads. Four contacts were made on a sample using small gold wires and highly conductive silver paste in this technique. Out of four wires, the current was passed through the two outer wires, and two inner wires were used to probe the voltage. Using dimensions of sample, the resistivity

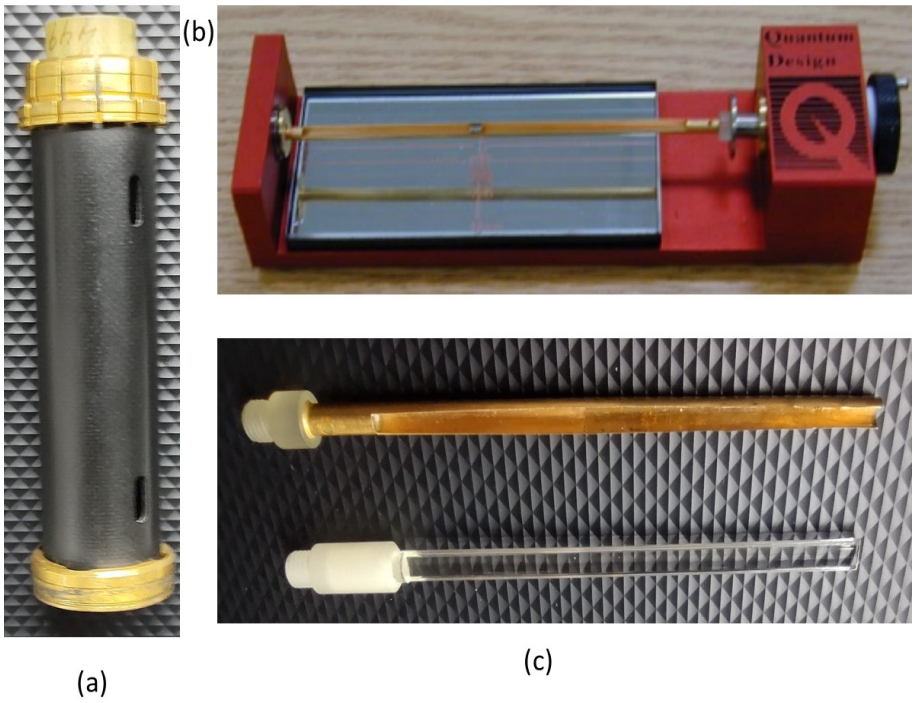

Figure 2.6: (a) Pick up coil (b) sample mounting platform (c) sample holder.

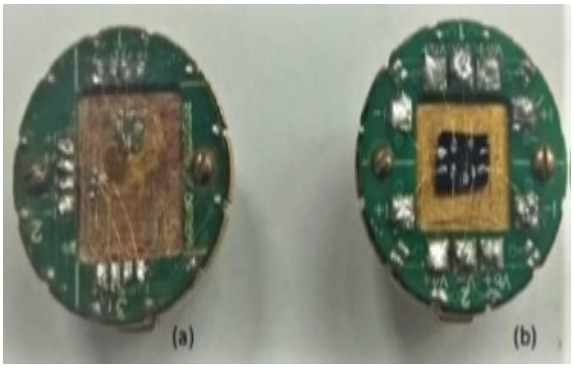

Figure 2.7: Sample mounted on a (a) DC resistivity and (b) AC resistivity puck.

can be calculated via relation given below:

$$\rho = \frac{RA}{l} = \frac{R(b \times t)}{l} \implies \frac{\rho}{t}(ohm/sq.) = \frac{R}{l/b} \tag{2.3}$$

where A (b $\times$ t) is the cross-section area, l is the distance between voltage leads, b is the width, t is the thickness of the sample, and I is the constant current supplied to the system, V is voltage difference measured between the leads. Here, the sq. term = l/b , this indicates the consideration of dimensions of sample in the data. This term mainly used in case of low dimensional systems such as thin films. In our system, the DC and AC resistivity can be measured in the temperature from 300 K to 2 K and a magnetic field up to 9 T. On a DC resistivity puck, one can mount three samples simultaneously, as shown in fig. 2.7(a). The AC resistivity measurement has greater sensitivity than DC measurement and is mainly used for highly conducting samples. The ACT option supports various transport measurements such as resistivity, Hall coefficient, I-V curve, and critical current. The typical picture AC resistivity puck with a sample is shown in Fig. 2.7 (b). The angle-dependent magnetoresistance measurements can be carried using the Horizontal Rotator option of QD-PPMS. There are a number of factors which must be taken into account during magnetotransport measurements, such as the current jetting effect and crystal inhomogeneity, etc. A significant resistance anisotropy (caused by the magnetic field) and point-like current contacts cause the current to flow primarily parallel to the magnetic field direction, where the resistance is minimal. The electrical current creates a jet between the current contacts if the magnetic field B is applied along the line connecting them, giving rise to the term "current jetting." The non-collinear voltage probes on the sample's surface then disengage from the current and measure a reduced or even zero potential difference, V(B). The measured voltage decreases as the resistance anisotropy increases with increasing field, which results in an apparent negative longitudinal MR, described here by MR(B) = R(B)/ R_o, R_o = R(B = 0). The current jetting effect can be minimized by using a perfect bar shape single crystal with collinear and well-separated voltage contacts. In the present study, the electrical transport measurements were done using the standard four-probe technique ranging from room temp to 2K at a magnetic field of 9T using QD-PPMS [93].

CHAPTER 3

Observation of 2D weak anti-localization in thin films of the topological semimetal $Pd_3Bi_2S_2$

3.1 Introduction

The prediction and realization of Dirac and Weyl fermions in materials has triggered the research of other fermions in condensed matter physics. Recently, Bradlyn *et al.* have predicted the existence of new fermions (beyond Dirac and Weyl fermions) in various materials by performing electronic structure calculations within the density functional theory [40]. $Pd_3Bi_2S_2$ has been theoretically proposed to consist of exotic fermions having three-fold degenerate band crossing at P point, which is only 0.1 eV above the Fermi level, as shown in fig. 3.1 [40]. In previous reports, the magneto-transport studies have been done on polycrystalline, single-crystalline, and nanoparticle samples of $Pd_3Bi_2S_2$ [94, 95, 96]. The transport study of polycrystalline $Pd_3Bi_2S_2$ gave information about bulk's non-superconducting and metallic behavior down to 0.35 K [94]. In the case of $Pd_3Bi_2S_2$ nanoparticles, the superconducting transition was observed at 0.4 K [95]. In $Pd_3Bi_2S_2$ single crystals, the magneto-transport study revealed interesting features like a large non-saturating magnetoresistance, which was ascribed to the high mobility of the charge carriers [96]. It is essential to reduce the mobility of the bulk charge carriers to observe the contribution from surface states.

In low dimensional systems, several interesting phenomena such as weak lo-

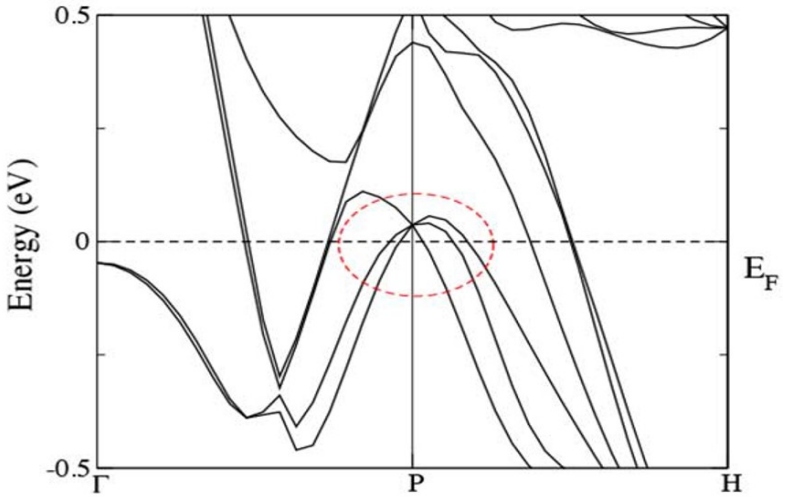

Figure 3.1: The band structure of $Pd_3Bi_2S_2$, where threefold crossing is almost at Fermi level. Reprinted from **Science 353, 6299 (2016).**

calization (WL) or weak anti-localization (WAL), quantum interference (QI), and universal conductance fluctuations (UCF) are expected to emerge [78, 83, 97, 98, 99]. The constructive or destructive interference of electrons moving through time-reversed paths gives rise to negative or positive correction to the conductivity, which is known as weak localization or anti-localization (WL/WAL) [78, 83, 97, 98]. The possible signatures of these effects can be observed using electron transport such as magneto-resistance (MR), Hall effect, etc. In topological materials, the WAL effect is observed as an important consequence of spin momentum locking, which results in a relative π Berry phase acquired by electrons executing time-reversed paths [100, 101]. In this chapter, we report the magneto-transport study of $Pd_3Bi_2S_2$ (PBS) thin films, which were grown using pulse laser deposition technique (PLD).

3.2 Experimental Details

$Pd_3Bi_2S_2$ thin films were grown on a Si(111) substrate using pulsed laser deposition (KrF excimer, λ = 248 nm) in Argon atmosphere. The laser ablation was performed on the polycrystalline target under the growth conditions of 1.8 J/cm^2 laser fluence at low repetition rate. The as-grown PBS thin-films (S0) were post annealed for 30 min in Argon atmosphere at 260°C (S1) and 300°C (S2). The phase purity of PBS thin-films was confirmed using a X-ray diffractometer. Figure 3.2 shows the x-ray diffraction (XRD) pattern of as-grown PBS thin film S0, which confirmed the cubic crystal structure of PBS thin films with space group $I2_13$.

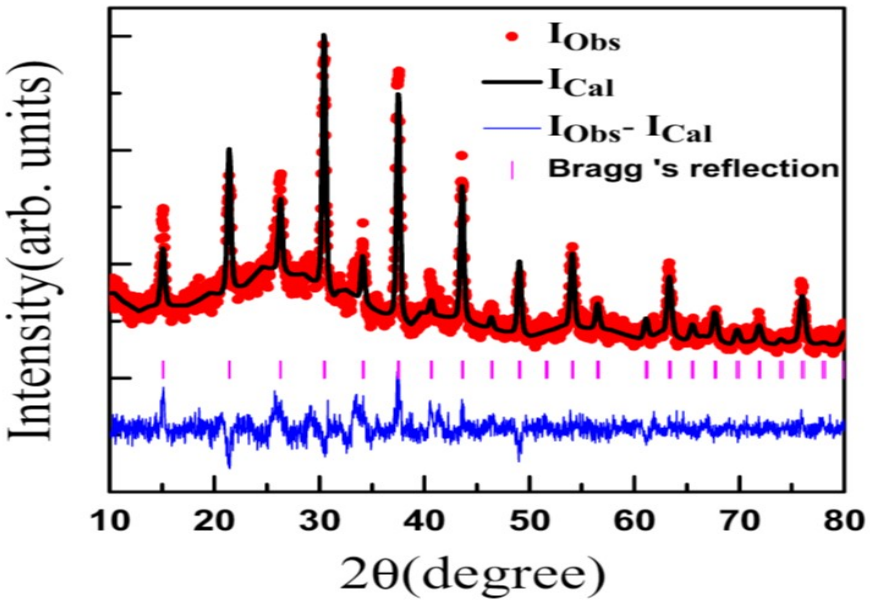

Figure 3.2: The X-ray diffraction pattern of $Pd_3Bi_2S_2$ with Rietveld refinement. The Red circles, black line, blue line, and magenta bar marks represent observed, calculated, background (the difference between observed and calculated) and Bragg positions, respectively.

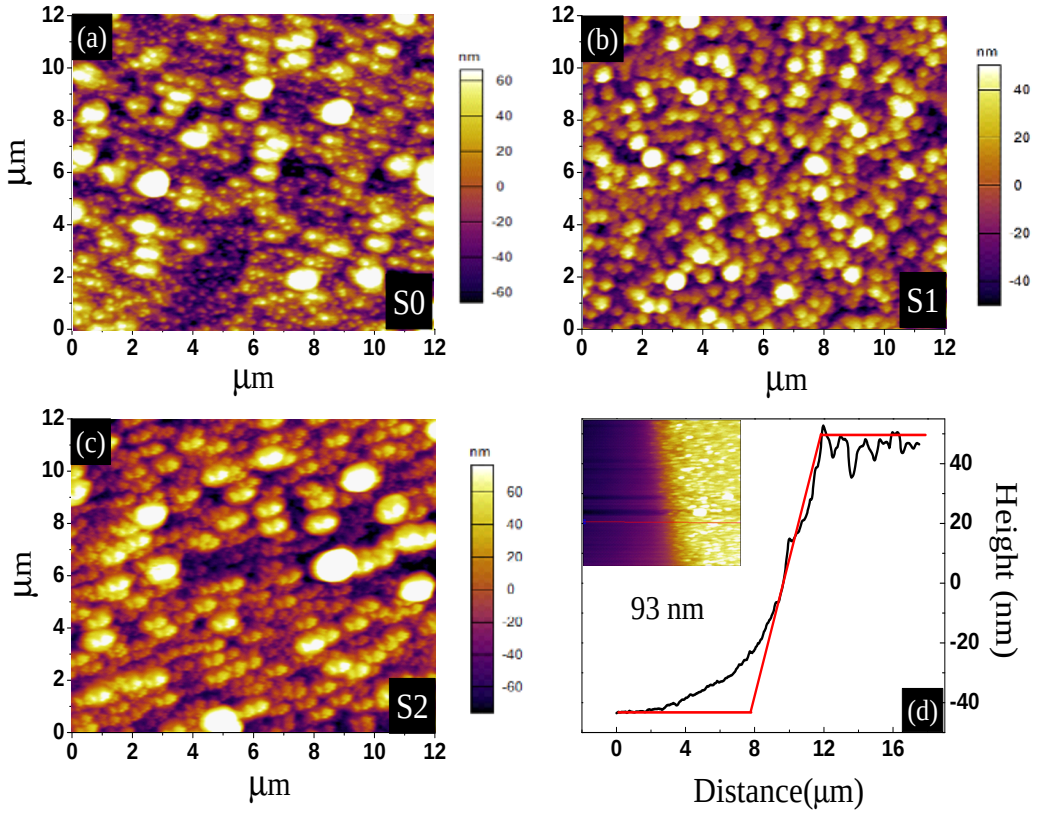

Figure 3.3: (a-c) AFM topography image of all PBS thin film samples. (d) Height profile across 93nm thin film.

A Rietveld refinement of the XRD pattern gave the lattice parameters $a = b = c$ = 8.47 Å, which are in good agreement with PBS bulk values reported previously [96]. The surface morphology and average film thickness were measured using an atomic force microscope (AFM) from Asylum Research (model:MFP3D) as shown in fig. 3.3. The stoichiometry of PBS thin films was confirmed using energy dispersive spectroscopy in a scanning electron microscope from JEOL as shown in fig. 3.4 (d). The longitudinal and Hall resistances were measured in a Quantum Design Physical Property Measurement System (PPMS-ECII) equipped with a 9 T magnet.

Table 3.1: Parameters for $Pd_3Bi_2S_2$ thin films. T_{ann} is the post-annealing temperature, Ro is the sheet resistance at the lowest temperature, RRR is the residual resistivity ratio, $n_e(n_h)$ is the electron(hole) carrier density, $\mu_e(\mu_h)$ is the electron(hole) mobility, L_ϕ is the phase coherence length, and α is a parameter in the HLN theory which depends on the number of conduction channels.

Extracted parameters	**S0**	**S1**	**S2**
T_{ann} (° C)	Not annealed	260	300
R_o	12.2	6.91	8.81
RRR	2.1	2.6	2.7
$n_e/n_h(\times 10^{21}/\text{cm}^3)$	0.19/1.4	0.21/1.6	0.2/1.53
$\mu_e/\mu_h(\times 10^2\text{cm}^2/\text{Vs})$	1.7/0.64	1.5/0.6	1.6/0.61
L_ϕ(nm)	206	239	218
α	0.28	0.26	0.29

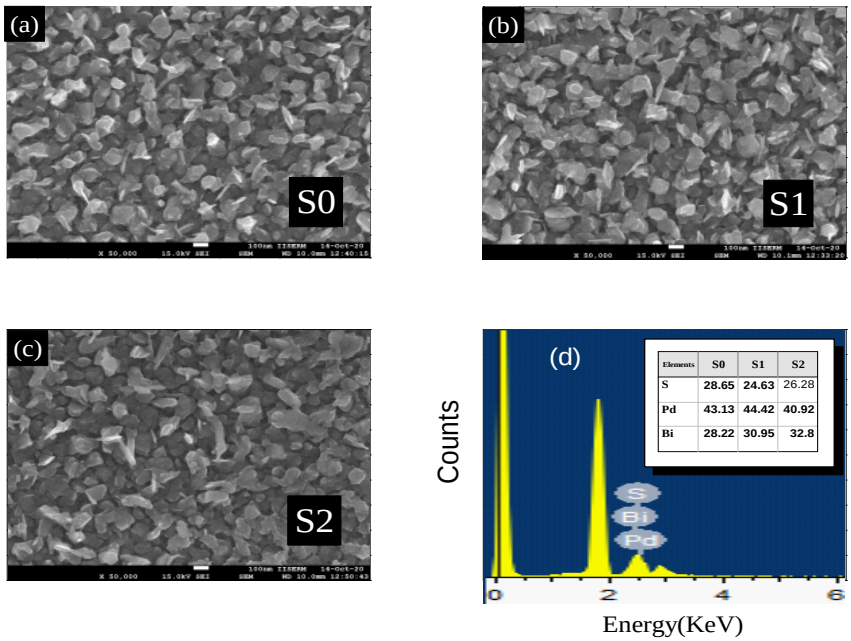

Figure 3.4: (a-c) SEM micro graphs of all PBS thin films obtained on Si (111) substrate (d) EDS data.

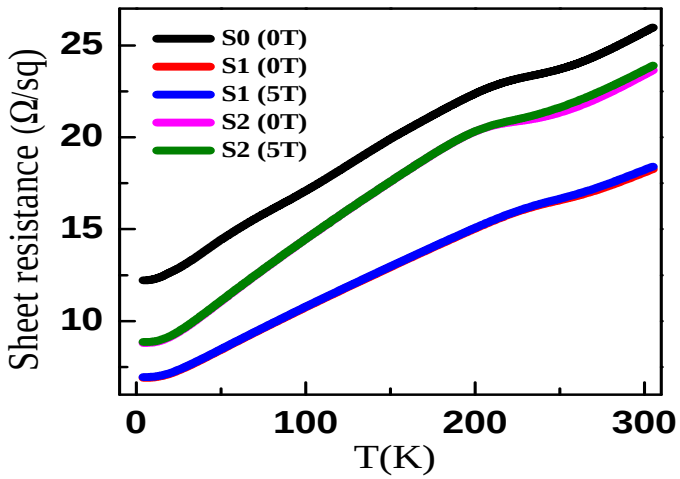

Figure 3.5: Sheet resistance vs temperature at B(T)=0,5 showing the metallic behavior of S0-S2 samples.

3.3 Result and Discussion

Figure 3.5 shows the temperature variation of sheet resistance R_S for PBS thin films in various magnetic fields applied transverse to the film. The temperature dependence of R_S reveals the metallic behavior of PBS thin films with a large residual resistance R_o. This metallic behavior is in agreement with previous reports on Bulk samples [96]. We also observe a slope change in the sheet resistance close to 220 K in all films, which was not observed in bulk samples [94, 95, 96]. The origin of this slope change is not understood at present, but we speculate that the connectivity between grains is changing with temperature, leading to a change in the conductivity of the films. To analyze the effect of annealing on the resistance of different films, we compare the residual resistivity ratio (RRR) and the residual resistivity R_o of all the thin films in Table 3.1. Fig. 3.5 and Table 3.1 show that the RRR increases for the annealed films suggest improved quality arising most likely from the improved connectivity between grains. However, the R_o varies non-monotonically, with a minimum value for the S1 films annealed at 260°C, suggesting that the optimal annealing temperature for the PBS films may be 260°C.

Figure 3.6 (a) shows the variation of Hall resistance (R_{xy}) with the magnetic field (B) at various temperatures for the S0 films. Hall resistance remains linear and positive at high temperatures with the magnetic field, as can be seen from fig. 3.6 (a). At lower temperatures, the Hall resistance becomes non-linear, which implies the presence of more than one type of charge carrier in PBS thin films. To extract the carrier concentration and mobility, we fit simultaneously and globally, the Hall conductance σ_{xy} and the longitudinal conductance σ_{xx} for all films to a semi-classical the two-band model given by the expression: [48, 102]

$$\sigma_{xy} = eB\left[\frac{n_h\mu_h^2}{1+(\mu_h B)^2} - \frac{n_e\mu_e^2}{1+(\mu_e B)^2}\right] \tag{3.1}$$

$$\sigma_{xy} = eB\left[\frac{n_h\mu_h}{1+(\mu_h B)^2} + \frac{n_e\mu_e}{1+(\mu_e B)^2}\right] \tag{3.2}$$

where e is the charge of an electron and B is the magnetic field. The $n(h,e)$ and $\mu(h,e)$ are the carrier density and mobility of electrons and holes, respectively. The fit is shown as the solid curve through the data for S0 in fig. 3.6(b). The parameters extracted from the fit for all the films are given in Table 1. Figure 3.6(c) and (d) show the temperature dependence of mobility and carrier density for S0 sample. The behaviour for S1 and S2 was found to be similar, which is shown in fig. 3.7.

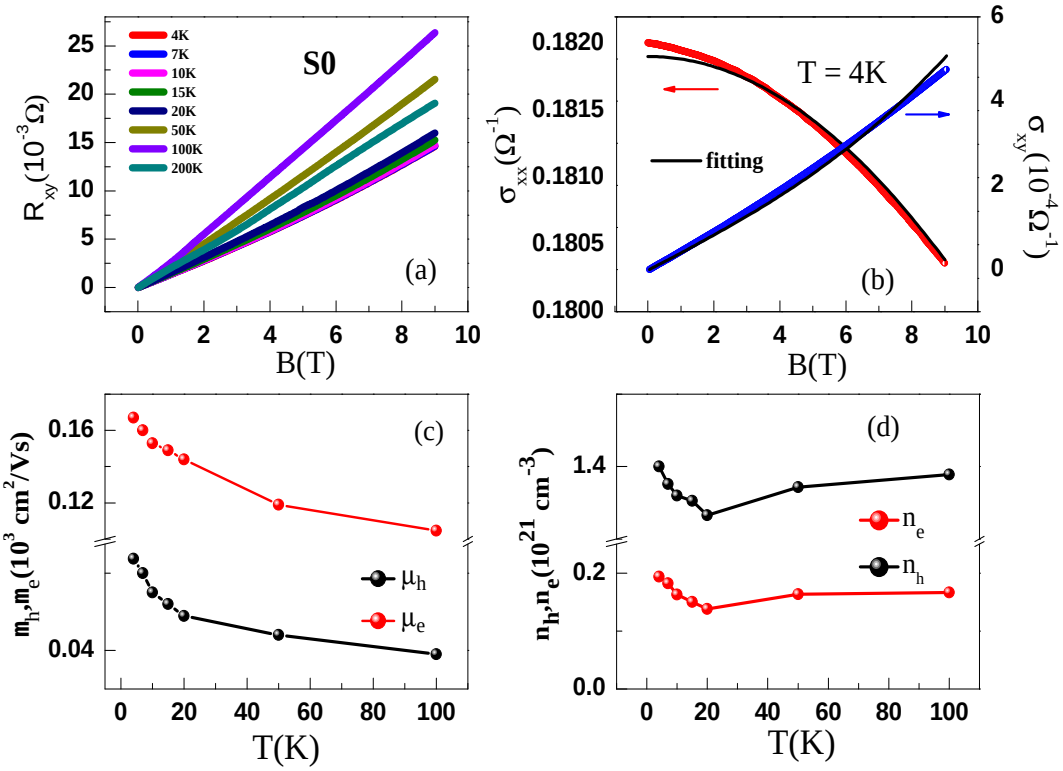

Figure 3.6: (a) Hall resistance (R_{xy}) vs magnetic field (B) at various temperatures for S0 thin film of PBS. (b) Variation of Hall conductance (σ_{xy}) and longitudinal conductance (σ_{xx}) as a function of B at T= 4 K. The solid curves through the data are the global fitting of the σ_{xy} and σ_{xx} by a two-band model (see text for details). (c) Temperature dependence of mobility and (d) carrier density of electron and hole carriers in S0. The solid curves through the data in (c) and (d) are guides to the eye.

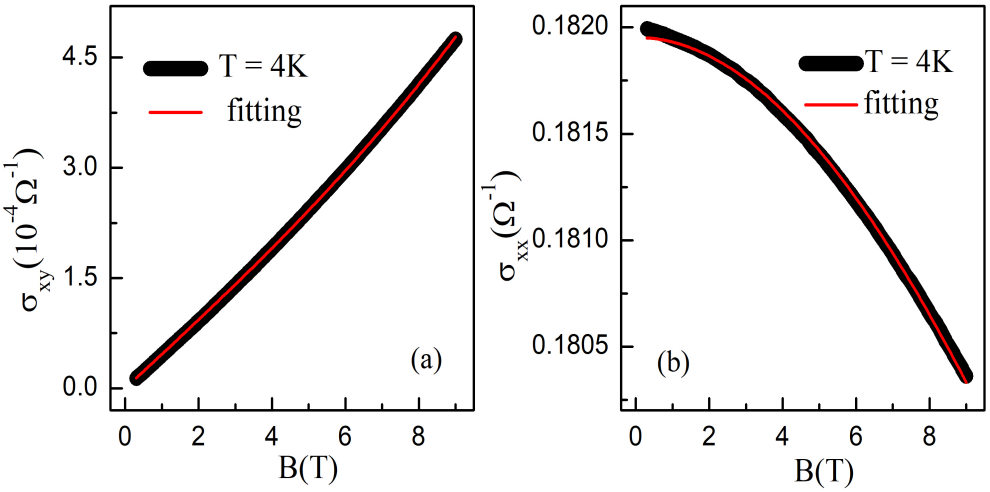

Figure 3.7: (b) Variation of Hall conductance (σ_{xy}) and longitudinal conductance (σ_{xx}) as a function of B at T= 4 K. The solid curves through the data are the global fitting of the σ_{xy} and σ_{xx} by a two-band model

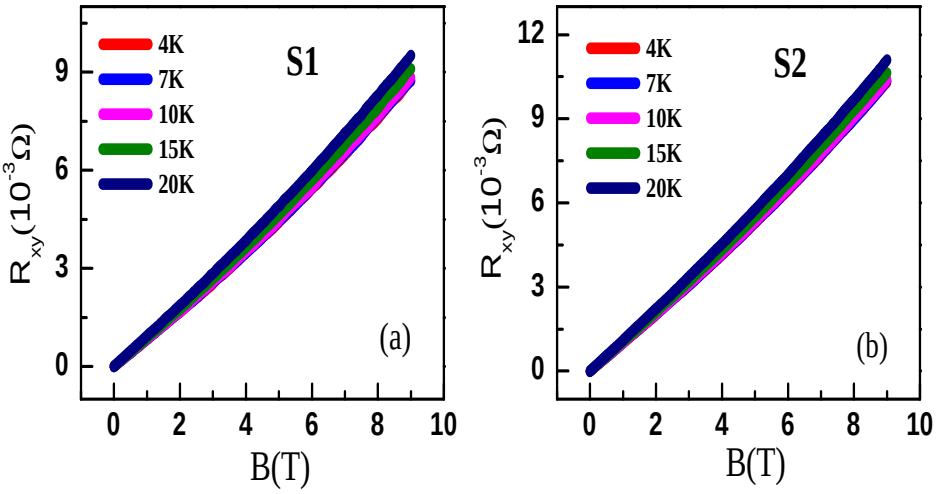

Figure 3.8: (a-b) Hall resistance (R_{xy}) vs magnetic field (B) at various temperatures for S1,S2 thin films of PBS.

The electron (hole) carrier density is estimated to be of order $10^{20}(10^{21})$, which are similar to values reported previously in PBS single crystals [96]. However, the mobility for the PBS films comes out to be of the order 10^2 cm^2/Vs, which is smaller than reported in single crystals [96]. The reduced mobility may be due to a larger amount of disorder in the films compared to the single crystals, as evidenced by the large residual resistance values. Additionally, the polycrystalline nature of the films may also lead to reduced mobility compared to crystals due to grain boundary scattering. From the extracted parameters, we can rule out the possibility of charge carrier compensation as n_h is an order of magnitude larger than n_e, indicating that holes are the dominant charge carriers in our PBS films. Alternately, one may fit σ_{xx} and σ_{xy} separately using the respective expression given above. We have made such a fit which is shown as the solid curve through the σ_{xx} and σ_{xy} data for S0 in Fig. 3.7. In the two-band model fitting of Hall data, over-parameterization will remain. Therefore, we have tried two different fittings (i) fitting of longitudinal (σ_{xx}) and transverse conductivity (σ_{xy}) indvidually, and (ii) simultaneous and global fitting of longitudinal (σ_{xx}) and transverse conductivity (σ_{xy}) as shown in Fig. 3.6, 3.7. From both fittings, we found that over-parameterization is reduced in the case of simultaneous and global fitting of σ_{xx},σ_{xy}. Therefore, we have mainly considered simultaneous and global fitting of σ_{xx},σ_{xy}. In order to reduce over-parameterization further, we have fixed one or two parameters in accordance with values obtained in previous reports. Thus, by fixing parameters one by one, we have obtained rectified values of different parameters.

Figure 3.8 (a) shows the percentage magnetoresistance MR% for S0 at various

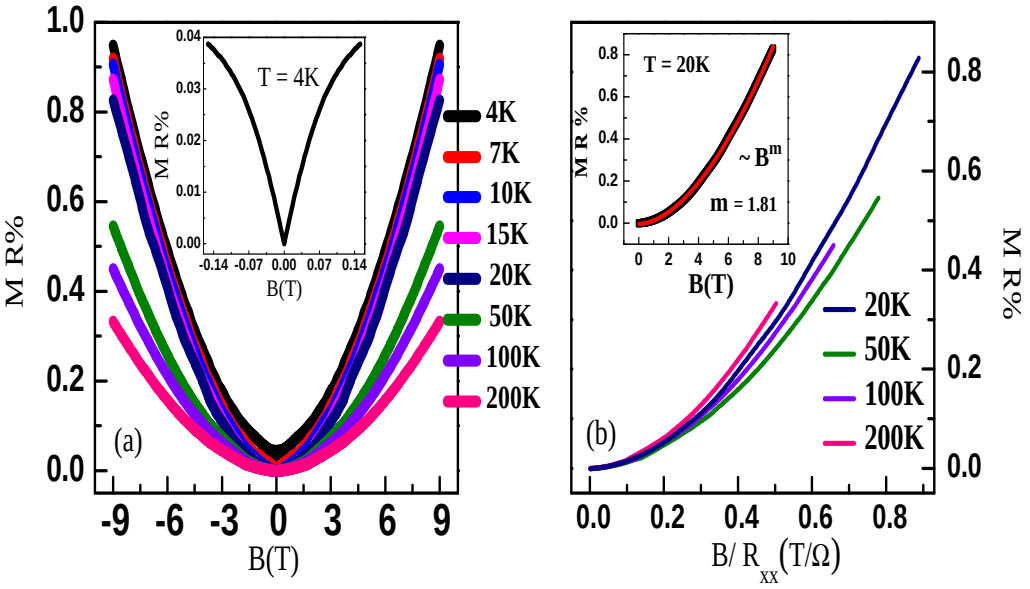

Figure 3.9: a) The percentage magneto-resistance MR% vs magnetic field B at various temperatures for S0 film. The inset shows the data at low magnetic fields at T=4 K showing the WAL effect. (b) Violation of Kohler's rule indicating the presence of multiple scattering mechanism. The inset shows the power-law Bm fitting of the MR data at T=20 K with m=1.81.

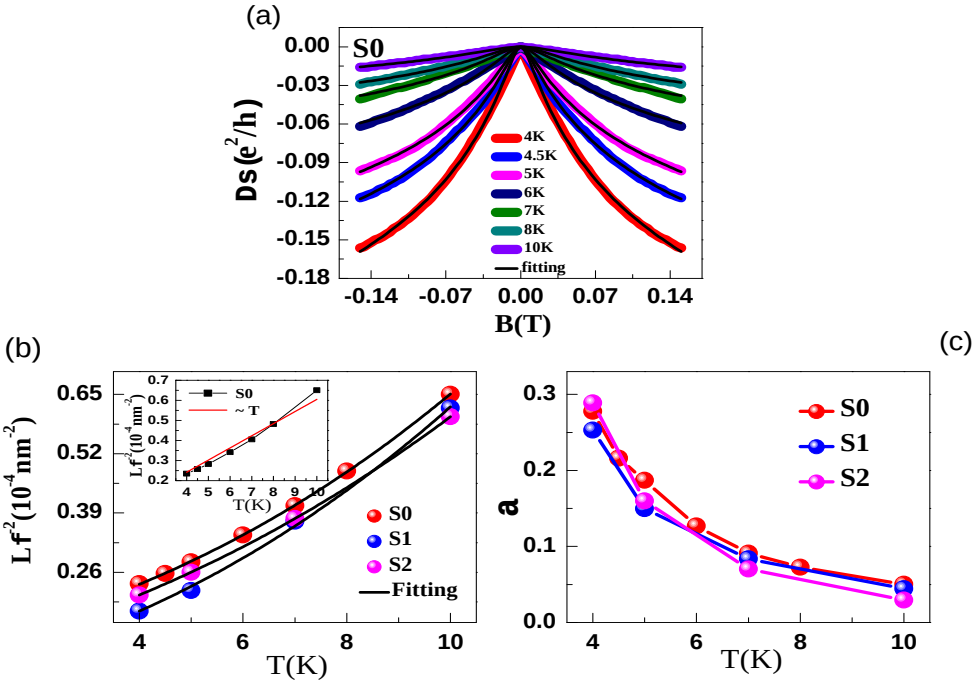

Figure 3.10: (a) The magneto-conductance ($\triangle\sigma$) versus field B at various temperatures for as-grown film S0. Solid curves through the data are fits to the HLN equation. (b) Variation of L_ϕ as a function of temperature, revealing the contribution of different scattering mechanisms. Inset shows the failure of a linear in T fitting. (c) Temperature dependence of α.

temperatures. The inset in fig. 3.8 (a) shows the MR data at low fields, highlighting the cusp-like behaviour at low magnetic fields. This cusp-like behavior under low field is a signature of weak anti-localization (WAL) [78, 83, 97]. The low value of the magnetoresistance in our films compared to the previous report on single crystals is mainly attributed to the lower carrier mobility in PBS thin films, as observed from the Hall data [96]. According to Kohler's rule, for materials with one dominant scattering mechanism, the MR can be represented as a universal function of the quantity $B\tau$, where τ is the time between scattering events of conduction electrons which is inversely proportional to the zero-field resistivity ρ [103]. We, therefore, expect that the MR is a universal function of the ratio B/ρ_{xx}. Figure 3.8(b) shows the MR data plotted as a function of B/R_{xx} for S0 sample. If Kohler's rule was obeyed, the MR vs. B/R_{xx} data would collapse onto a single curve. Figure 3.8 (b) shows that Kohler's rule is violated for PBS films, indicating more than one dominating scattering mechanism.

We next present the WAL analysis. However, the analysis depends on the dimensionality of the system. We must determine whether the mean free path is greater than the film's thickness for thin films. In our case, we have calculated the mean free path using the 2D formula, $l_e = \frac{\hbar}{e}\sqrt{2\pi n_e}\mu_e$, where n_e and μ_e are the 2D Hall carrier density and mobility, respectively. We estimate l_e = 117 nm for S0, larger than the film thickness (93 nm). For Quantum interference (QI) effects, the relevant length scale is the phase coherence length $L\phi = \sqrt{D\tau}$, where D is the diffusion constant, and τ is the phase coherence time. Also, the criterion for the 2D nature of thin films is $L\phi >$ thickness [104, 105]. In our case, the value of $L\phi$ is found to be greater than the thickness of thin-film (based on the analysis presented below), which indicates the 2D nature of our thin films. Figure 3.9 (a) shows the conductance at various temperatures in the low magnetic field range $|B| \geq 0.15$ T for S0. The conductance was found using $\triangle\sigma = \sigma(B) - \sigma(0)$, where $\sigma(B) = (L/W)(1/R_{xx})$, and L and W are the length and width of film, respectively. For 2D systems, Hikami-Larkin-Nagaoka (HLN) equation can be used to model the effect of localization[78, 83]. This theory involves the contribution of quantum effects from three different mechanisms, namely, spin-orbit coupling (SOC), elastic scattering, and electron phase coherence. In the limit of high SOC, Hikami-Larkin-Nagaoka (HLN) can be written as

$$\triangle\sigma = \alpha\frac{e^2}{\pi h}\left[\psi\left(\frac{1}{2}+\frac{B_\phi}{B}\right) - log\left(\frac{B_\phi}{B}\right)\right] \tag{3.3}$$

where ψ is the digamma function, e is the electron charge, h is the Planck constant,

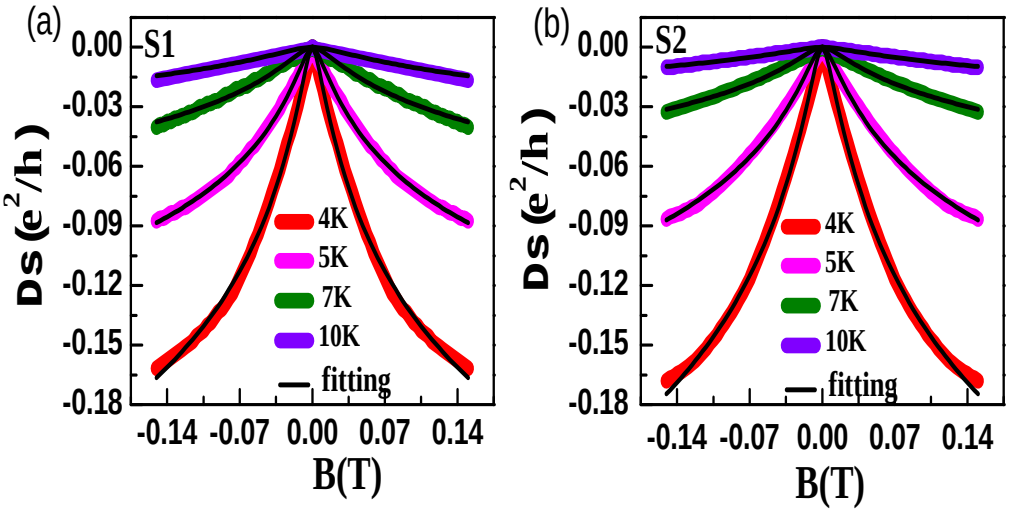

Figure 3.11: The magneto-conductance ($\triangle\sigma$) versus field B at various temperatures for S1,S2. Solid curves through the data are fits to the HLN equation.

$B_\phi = \hbar/(4eL_\phi{}^2)$ is the characteristic field associated with phase coherence length L_ϕ. The parameter α gives the number of conduction channels contributing to the transport. According to the HLN theory, α takes the value 1/2 for weak anti-localization (WAL). However, α has often been observed to deviate from 1/2 in the case when more than one conduction channels are available. In particular, α = 1/2 only for a single topologically non-trivial conduction channel. If there is more than one topological channel, each will contribute α = 1/2 and add up to give a combined α >1/2, whereas if there are multiple channels and some are topologically trivial while others are topological, it leads to α <1/2 [84, 100, 106].

To extract the parameters α and Lϕ, We fit the experimental data by eq. (3.3). The temperature dependence of the fitting parameters for all the films is shown in Fig. 3.9 (b,c). The extracted value of α is 0.28 at T = 4 K, which is smaller than the theoretical value (0.5) expected for a single conduction channel. This indicates the presence of more than one conduction channel. For example, the presence of topologically trivial bands at the Fermi level could contribute to the conductivity in addition to the topological electrons. Figure 3.9 (c) shows that α reduces from 0.28 at 4 K to 0.05 at 10 K, which is consistent with the trend observed previously for other topological materials like Cd_3As_2. Qualitatively, we observed similar magneto conductance behavior for S1 and S2 samples, as shown in fig. 3.10. We fit the experimental data by Eq. 3.3 with fitting parameters α and L_ϕ. The temperature dependence of the obtained fitting parameters for all the films was shown in fig. 3.9. The extracted value of α = 0.26(0.29) at T = 4 K for S1(S2) is smaller than the theoretical value 0.5 expected for a single topological conduction channel. This

indicates the presence of both topological and trivial conduction channels.

Figure 3.9 (b) shows the temperature dependence of phase coherence length L_ϕ plotted as $1/L_\phi{}^2$ versus T for all films. The $L\phi$ decreases from 206 nm at 4 K to 124 nm at 10 K. The fact that $L\phi$ comes out to be larger than the film thickness validates our use of 2D WAL analysis for our PBS films. The Nyquist theory, which considers electron-electron scattering, predicts that $L_\phi \propto T^{-1/2}$ for 2D systems [107]. The inset of fig. 3.9(b) shows that the L_ϕ data for PBS doesn't follow the $T^{-1/2}$ dependence. This indicates that multiple scattering mechanisms with different temperature dependences could be involved in the dephasing of the electron's phase in PBS thin films. We try to analyze the temperature dependence of L_ϕ using the simple equation:[108]

$$\frac{1}{L_\phi^2} = \frac{1}{L_{\phi o}^2} + A_{ee}T + B_{ep}T^p \tag{3.4}$$

where $L_{\phi o}$ represents the zero temperature dephasing length, and A_{ee} T and B_{ep} T^p represent the contributions from electron-electron and electron-phonon interactions, respectively. The value of p for electron-phonon interaction in 2D materials can vary between 2 to 3 depending on the effective dimensionality and disorder in the film [109]. We obtained an excellent fit of the temperature-dependent L_ϕ data by the eq. (3.4) for all the films, shown by the solid curves through the data in fig. 3.9 (b). The value of p is ≈ 2.4 similar to values found on disordered films of $GeSb_2Te_4$ [110].

To further confirm that the WAL effect is coming from the 2D topological surface states and not the bulk bands, we investigated the angular dependence of the magneto-conductance. The conductance at T = 4 K as a function of magnetic field applied at various angles θ to the current, is shown in fig. 3.11 (a). To reveal contribution from the 2D surface states, we have subtracted the θ = 0 data from those at finite θ and plotted the difference as a function of the perpendicular field component $B\mathrm{Sin}\theta$ as shown in fig. 3.11 (b). It is clear that at low values of the perpendicular field, before the upturn in the data due to contribution from bulk bands, all data measured at various θ collapse onto a common curve demonstrating the dominant contribution to the WAL from 2D topological surface states. Such scaling of tilt angle dependent conductivity data demonstrating 2D WAL from topological surface states has been observed previously in many topological materials like single crystals of $Bi_2Se_{2.1}Te_{0.944}$, nano-flakes of $Bi_2(Se_xTe_{1-x})_3$, low mobility crystals of LuPdBi, few layer devices of $ZrTe_5$, and disordered thin films of Bi_2Te_3 [85, 86, 111, 112, 113].

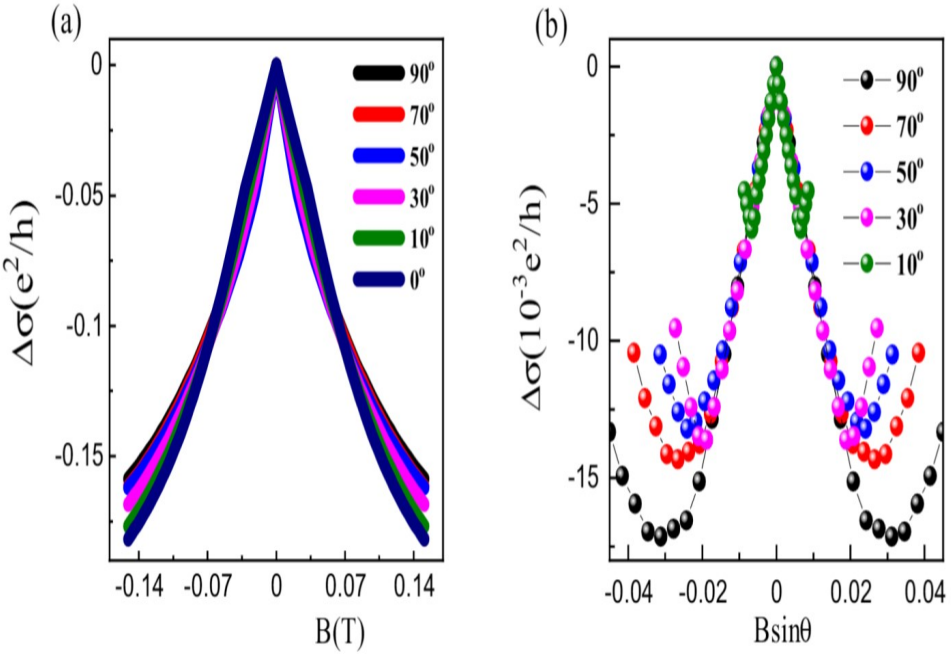

Figure 3.12: (a) The magneto-conductance ($\triangle\sigma$) at T = 4 K measured with the field B applied at various angles θ to the current direction. (b) The 2D contribution to the magneto-conductance at various θ as a function of the perpendicular component of the applied magnetic field BSinθ.

3.4 Conclusions

We report the first synthesis of thin films (93 nm) of the novel topological material $Pd_3Bi_2S_2$ grown on Si (111) substrate by pulsed laser deposition. Longitudinal resistance measurements on PBS thin films indicate a disordered metallic system, which results in reduced mobility of bulk carriers as compared to single crystals. This suppresses the bulk contribution and allows the first detection of transport contribution from topological surface states through the observation of the 2D WAL effect. The WAL data measured for magnetic fields applied at different angles to the current direction, all scale with the perpendicular component of the magnetic field, confirming the contribution of 2D topological surface states to the WAL. These results are satisfactorily analyzed in terms of Hikami-Larkin-Nagaoka theory. It was found that the coefficient α deviates from the value 0.5 expected for 2D systems with a single topological conduction channel. This indicates the contribution from additional (topological and trivial) conducting channels in the electron transport of PBS films. Dependence of the dephasing length L_ϕ on temperature is also anomalous. We found that this behaviour can be understood by including both the Nyquist

electron-electron scattering as well as electron-phonon scattering as the phase relaxation mechanism in PBS films. The magneto-resistance data show deviations from Koehler's rule suggesting the presence of multiple scattering mechanisms. These anomalous behaviours make $Pd_3Bi_2S_2$ an interesting system for further study in various morphologies.

CHAPTER 4

Weak Anti-localization in the Topological Semimetal Candidate $Pd_3Bi_2Se_2$

4.1 Introduction

Recently, a family of ternary compounds with the formula unit $T_3M_2X_2$ (T = Ni, Co, Rh, Pd or Pt; M = In, Sn, Pb, Tl or Bi; and X = S, Se or Te) has attracted a lot of interest [94, 114, 115]. The $T_3M_2X_2$ family of compounds such as $Ni_3Bi_2S_2$, $Pd_3Bi_2Se_2$, and $Rh_3Bi_2Se_2$ manifest superconductivity at low temperatures [94, 114, 115, 116]. Among the members of this family of materials, being host to non-trivial topological behavior, the materials $Co_3Sn_2S_2$, $Pd_3Bi_2S_2$ have been most widely studied [54, 72, 96, 117]. Another member $Pd_3Bi_2Se_2$ has also been proposed to be topologically non-trivial in nature [40, 38]. Previous studies have revealed superconductivity below 1 K in bulk, thin films, and nanoparticles of $Pd_3Bi_2Se_2$ [94, 95, 116]. However, the non-trivial topological behavior of $Pd_3Bi_2Se_2$ is still unexplored.

It is important to identify signatures in magneto-transport measurements of the non-trivial topology. Unlike the conventional electron gas with parabolic dispersion [118], topological materials have the linear energy dispersion that leads to a large separation between the lowest and the first Landau level (LL) of Dirac fermions [119, 120]. Consequently, quantum Hall effect, unsaturated linear magnetoresistance, and non-trivial Berry phase could be observed in Dirac semimetal

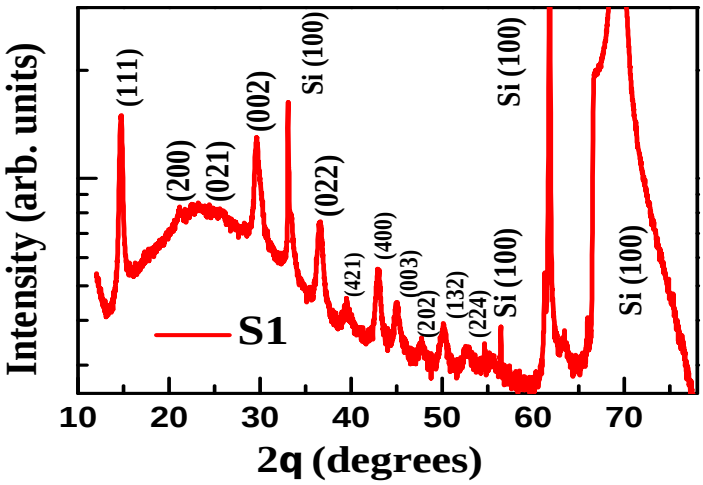

Figure 4.1: X-ray diffraction data for grown S1 thin films of $Pd_3Bi_2Se_2$.

candidates.[121, 122]. Additionally, in magneto-transport measurements, the electron phase can be probed via the quantum (constructive or destructive) interference of electron waves that occurs between electrons traveling through the time-reversed paths [78, 83, 97, 98]. For materials with weak spin-orbit coupling, constructive interference occurs, which leads to weak localization (WL). The presence of a Berry curvature in momentum space may lead to an extra phase shift of π for such closed trajectories, resulting in weak anti-localization (WAL) [113, 123, 124, 125]. This phase shift is a direct consequence of spin-momentum locking. The magnetic field breaks time-reversal symmetry, which is required for interference. Thus quantum (constructive/destructive) interference can be manifested as a positive (negative) magneto-conductance in low magnetic fields.

In this chapter, we explore the magneto-transport properties of $Pd_3Bi_2Se_2$ thin films grown by pulsed laser deposition technique (PLD).

4.2 Methods

$Pd_3Bi_2Se_2$ thin films were grown using a pulsed laser deposition technique following the procedure as described in chapter 3. The single crystalline substrate (Si 100) was heated at 240°C during the growth of thin films. The x-ray diffractometer (Bruker D8 Advance system with Cu-Kα radiation) was used to determine the phase purity of $Pd_3Bi_2Se_2$ thin-films. Figure 4.1 shows the x-ray diffraction (XRD) pattern of $Pd_3Bi_2Se_2$ thin films measured at T= 300 K, which confirms the phase purity of thin films [94, 95, 116]. Figure 4.2 (a) shows the atomic force

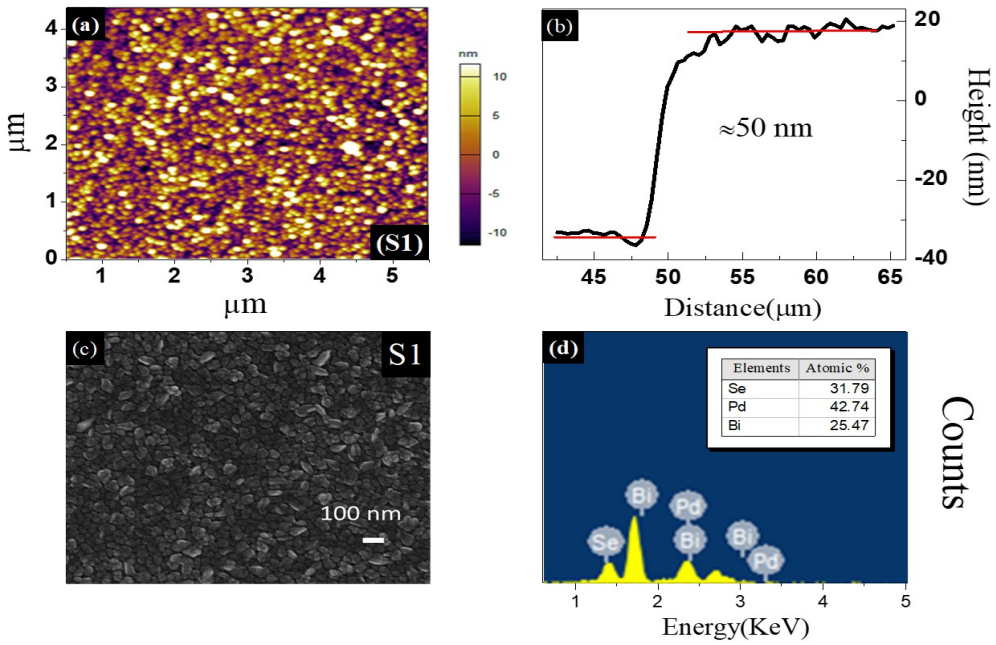

Figure 4.2: The Atomic Force Microscope topography image of surface of S1 $Pd_3Bi_2Se_2$ thin film. (b) The height profile across the S1 film with thickness ≈ 50 nm. (c) A SEM image of surface of S1 film. (d) Results of EDS spectroscopy on S1 film showing the presence of Pd, Bi, Se in stoichiometric amounts in film.

microscope (AFM) topography image of $Pd_3Bi_2Se_2$ thin films. Using AFM, we measured the thickness of the sample, which is 50 nm, as shown in Fig. 4.2 (b). The energy dispersive spectroscopy with a scanning electron microscope (SEM) is used to confirm the stoichiometry of thin films.Figure 4.2 (c) shows the SEM image of the S1 sample. Figure 4.2 (d) shows energy dispersive X-ray spectroscopy data, where peaks of bismuth, palladium, and selenium are observed. These characterization data demonstrate the growth of polycrystalline $Pd_3Bi_2Se_2$ thin films. $Pd_3Bi_2Se_2$ thin films with different thicknesses (50nm, 22nm) are designated as S1, S2, respectively. The electrical transport measurements were performed in Physical Property Measurement System (CFMS 14T, Cryogenics Ltd.).

4.3 Results and Discussion

To determine the carrier density and its mobility, the Hall resistivity (R_{xy}) was measured. Figure 4.3 (a) shows the variation of Hall resistivity (R_{xy}) with the magnetic field (B) at various temperatures for S1. At high temperature, R_{xy} is almost linear in the field and negative. However, with decreasing temperature, R_{xy}(B) be-

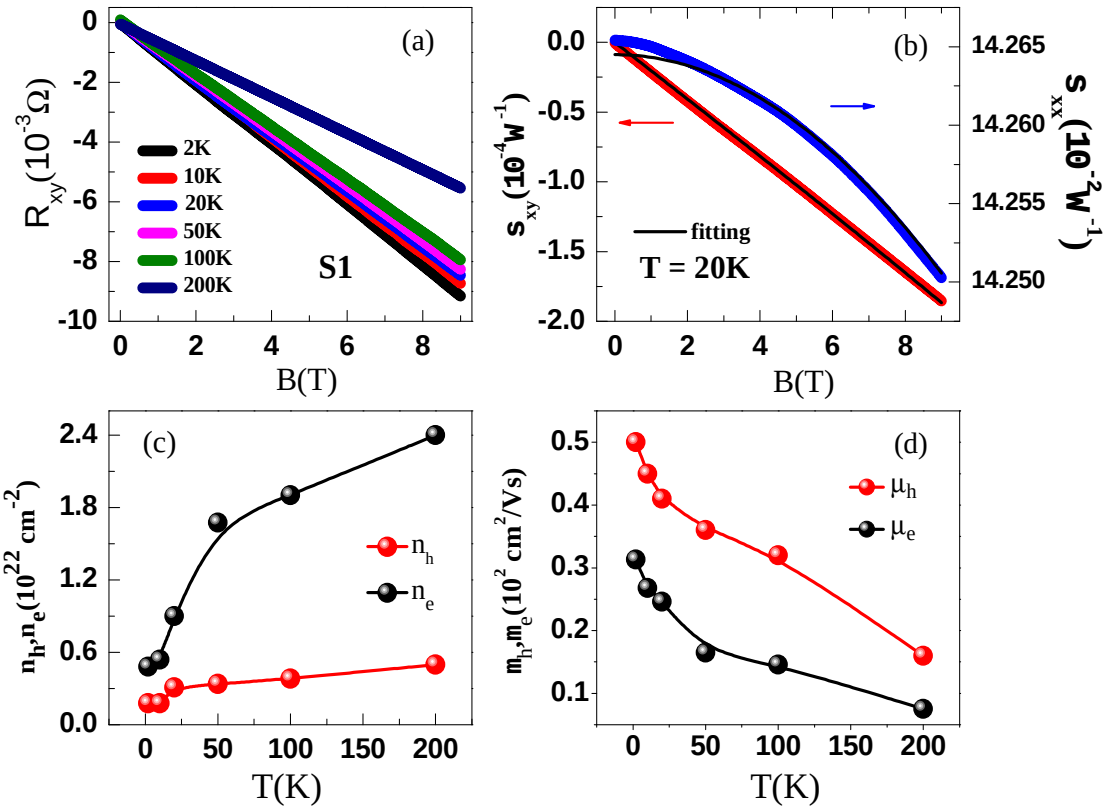

Figure 4.3: The Hall resistance (R_{xy}) vs magnetic Field at various temperatures for S1 thin film of $Pd_3Bi_2Se_2$. (b) Variation Hall conductance (σ_{xy}) and longitudinal conductance (σ_{xx}) vs magnetic field at 20K. The solid curves through the data are the global fitting of σ_{xy} and σ_{xx} by two band model. (c) The temperature dependence of carrier density and (d) mobility for electron and hole carriers in S1.

comes non-linear, which implies the presence of more than one type of charge carrier. To have more insight, we fit simultaneously and globally the Hall conductance (σ_{xy}) and longitudinal conductance (σ_{xx}) by semi-classical two-band model, which is given below:[48, 102]

$$\sigma_{xy} = eB\left[\frac{n_h\mu_h^2}{1+(\mu_h B)^2} - \frac{n_e\mu_e^2}{1+(\mu_e B)^2}\right] \tag{4.1}$$

$$\sigma_{xx} = e\left[\frac{n_h\mu_h}{1+(\mu_h B)^2} + \frac{n_e\mu_e}{1+(\mu_e B)^2}\right] \tag{4.2}$$

where e is the electron charge. The $n_{h(e)}$ & $\mu_{h(e)}$ are the sheet carrier density and mobility, respectively. The subscript e, h denotes electrons and holes, respectively. The fitting of Hall conductance (σ_{xy}) and longitudinal conductance (σ_{xx}) is shown

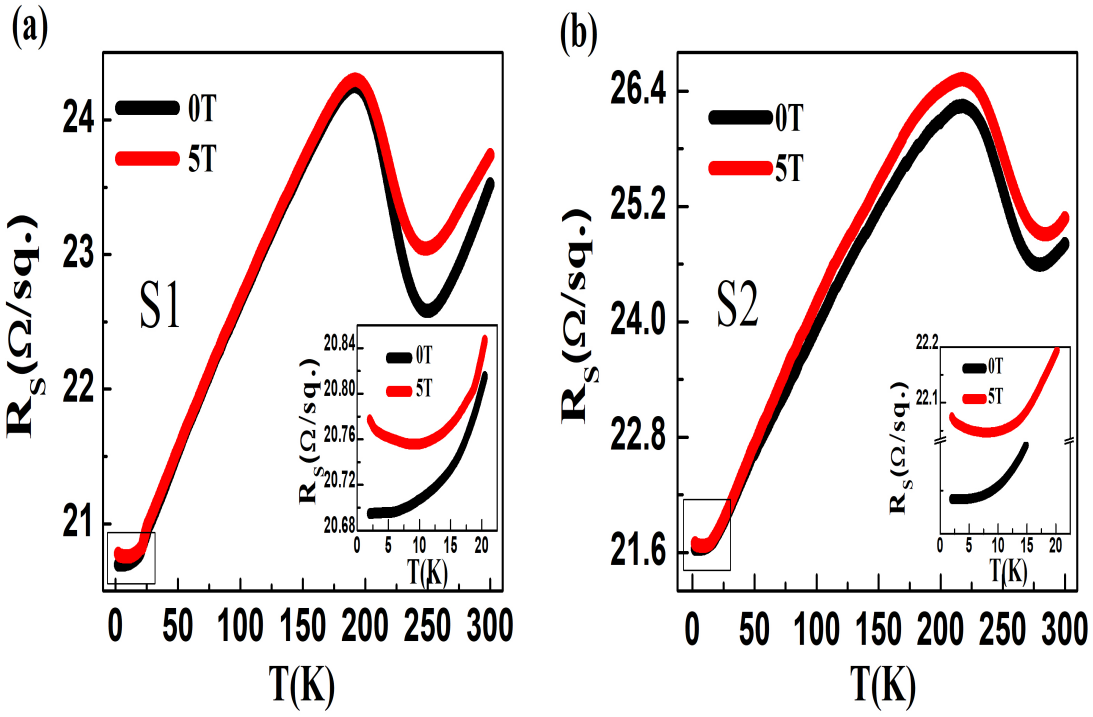

Figure 4.4: (a-b) Sheet resistance vs temperature at various magnetic fields showing the semi-conducting behavior of S1,S2 samples, Inset curve shows an upturn in sheet resistance at low temperatures for S1,S2.

by solid curves in Fig. 4.3 (b). The extracted values of carrier density are of the order 10^{22} and mobility is 10^2, which are close to the values reported previously [116]. The extracted parameter rules out the possibility of charge carrier compensation similar to previous reports, and electrons seem to be the dominant charge carriers [116].

Figure 4.4 (a-b) shows the temperature variation of sheet resistance (R_S) for $Pd_3Bi_2Se_2$ thin films in magnetic fields B = 0T, 5T. We observe metallic behavior with a significant residual resistance R_o at the lowest temperature, indicating the presence of some disorder. Under sufficiently strong magnetic field, R_S(T) below $\sim$ 10 K shows an upturn signalling a tendency towards insulating behaviour as can be seen in Fig. 4 (a) and (b) insets. The temperature at which the minimum in R_S(T) occurs increases with B. Such an upturn in resistance on the application of a field has been observed in several topological materials although an understanding of its origin has not yet been established. [126].

Another notable feature in the R_S(T) is an abrupt upturn in resistance below 250 K for S1 and 275 K for S2 as seen in Fig.4 (a) and (b). Below these temperatures the resistance first increases, goes over a maximum, and then continues in a metallic fashion for lower temperatures. This behaviour is similar to that ob-

served for several charge density wave (CDW) materials.[127, 128] These CDW like features were not observed in the bulk sample reported previously.[94] Also, this could be due to grain connectivity in the thin films. We currently do not have an understanding of the origin of this anomaly in thin films of $Pd_3Bi_2Se_2$.

In figure 4.5 (a), the percentage magnetoresistance (MR% = $\frac{R(B)-R(0)}{R(0)} \times 100$) is plotted as a function of B at various temperatures for B applied perpendicular to the plane of the film. At low temperatures, we observed a logarithmic cusp around zero magnetic fields, which is a signature of WAL. [78, 83, 97, 98]. An increase in magnetic field results in a non-saturating linear response at higher fields. As temperature increases, the linear dependence of MR turns into the classical dependence, as shown in Fig. 4.5 (b). The MR of bands with parabolic dispersion either saturates at high fields or increases as B^2. Such an unusual non-saturating linear magnetoresistance has previously been reported in the gapless semiconductor $Ag_{2-\delta}$(Te/Se) and was argued to arise due to a linear energy spectrum in the quantum limit [130, 131]. Recently, first-principle calculations confirmed a gapless Dirac-type surface state in these materials [132]. Linear magnetoresistance is also observed in Bi_2Te_3, $BaFe_2As_2$, and (Ca, Sr)$MnBi_2$ with Dirac fermion states [121, 122, 133, 134].

Applying a strong perpendicular magnetic field (B) leads to a quantization of the orbital motion of carriers with linear energy dispersion, which results in quantized Landau levels (LLs). The energy splitting between the lowest and first LLs is described by $\triangle_{LL} = \pm\ v_F\ \sqrt{2e\hbar B}$, where v_F is the Fermi velocity, E_F is the Fermi energy [119, 120]. In the quantum limit at a specific value of magnetic field and temperature, $\triangle_{LL}$ becomes larger than the Fermi energy E_F and thermal fluctuations k_BT at a finite temperature. Consequently, all carriers occupy the lowest Landau level, which results in linear magnetoresistance in transport. The transverse MR manifests a crossover at a critical field $B^\star$ from the semi-classical weak-field MR $\sim B^2$ to the high-field MR $\sim$ B dependence. The critical field $B^\star$ above which quantum criterion is achieved is given as $B^\star = \frac{1}{2e\hbar v_F^2}\ (E_F + k_BT)^2$ [122]. Thus, if the magnetoresistance is dominated by Dirac Fermions with a linear dispersion, a parabolic dependence on T is expected for the crossover field B^*. Figure 4.5 (c) shows the temperature dependence of $B^\star$ which can be fitted well with $\frac{1}{2e\hbar v_F^2}\ (E_F + k_BT)^2$. The fitting gives the values of $v_F \sim 1.47 \times 10^5$ ms^{-1} and $E_F \sim 9.81$ meV. The non-saturating linear magnetoresistance at high fields and low temperatures, and the $B^* \propto T^2$ presents strong evidence for the existence of Dirac Fermions in $Pd_3Bi_2Se_2$.

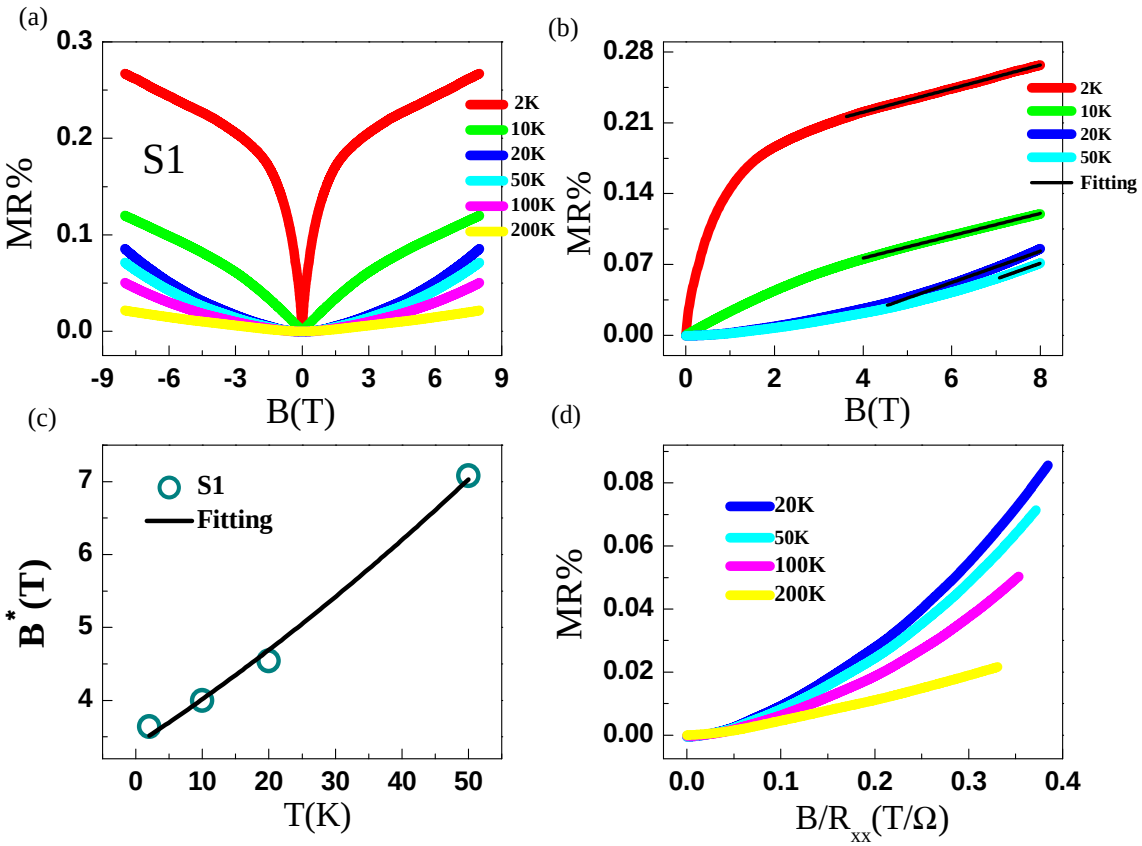

Figure 4.5: (a) Magneto-resistance (MR%) vs magnetic field(B) at various temperatures in transverse configuration for S1 sample. (b) MR% vs B at various temperatures. The Black solid lines are linear fits in higher magnetic field region. (c) Temperature variation of critical magnetic field ($B_{\star}$(T)) (d) The violation of Kohler's plot showing the presence multiple scattering mechanism. .

Kohler's rule states that for materials with one dominant scattering mechanism, the magneto-resistance (MR%) can be represented in terms of scaling function F(x) as follows:[103]

$$\mathrm{MR\%} = \mathrm{F}\left(\frac{B}{R_{xx}}\right) \tag{4.3}$$

where R_{xx} is the zero-field resistivity at a certain temperature. According to Kohler's rule, MR% data is plotted as a function of B/ρ_o as shown in Fig 4.5 (d). For Kohler's rule, MR% vs. B/ρ_o curves should collapse into a single curve in a weak-field regime. Figure 4.5 (d) shows the violation of Kohler's rule, which reveals more than one dominating scattering mechanism. Ahead of further discussions about magneto-transport in $Pd_3Bi_2Se_2$ thin films, we first investigate the dimensionality of thin films. In the case of Quantum interference (QI) effects, the relevant length scale is phase coherence length (L_ϕ), which is equal to $\sqrt{D\tau}$. The criterion for quantum interference to be 2D is $L\phi > t$, where 't' is the thickness of the film [104, 135]. In our case, the value of L_ϕ is greater than the thickness of thin-film (based on the analysis below), indicating the 2D nature of thin films.

Figure 4.6 (a) shows the conductance correction ($\triangle\sigma$) vs. magnetic field at various temperatures in the range of $\pm$ 0.25 T for the S1 sample. Here, the two-dimensional conductance σ_{xx} is obtained by inverting the MR tensor because the Hall resistance R_{xy} of these films is much smaller than the longitudinal resistance R_S. Therefore, we have $\sigma(B) = (L/W)\ (1/R_S)$, L and W are the length and width of the sample, respectively. For two-dimensional systems, Hikami-Larkin-Nagaoka (HLN) equation has been widely used to describe the effect of localization [78, 83]. In the limit of high SOC, Hikami-Larkin-Nagaoka (HLN) can be written as

$$\triangle\sigma(\mathrm{B}) = -\alpha\frac{e^2}{\pi h}\left[\psi\left(\frac{1}{2}+\frac{B_\phi}{B}\right) - \ln\left(\frac{B_\phi}{B}\right)\right] \tag{4.4}$$

where ψ is the digamma function, $B_\phi = \hbar/(4eL_\phi^2)$ is a characteristic field which is required to destroy phase coherence. α measures no. of conduction channels contributing to the transport. The parameter α is a prefactor expected to be 1/2 and

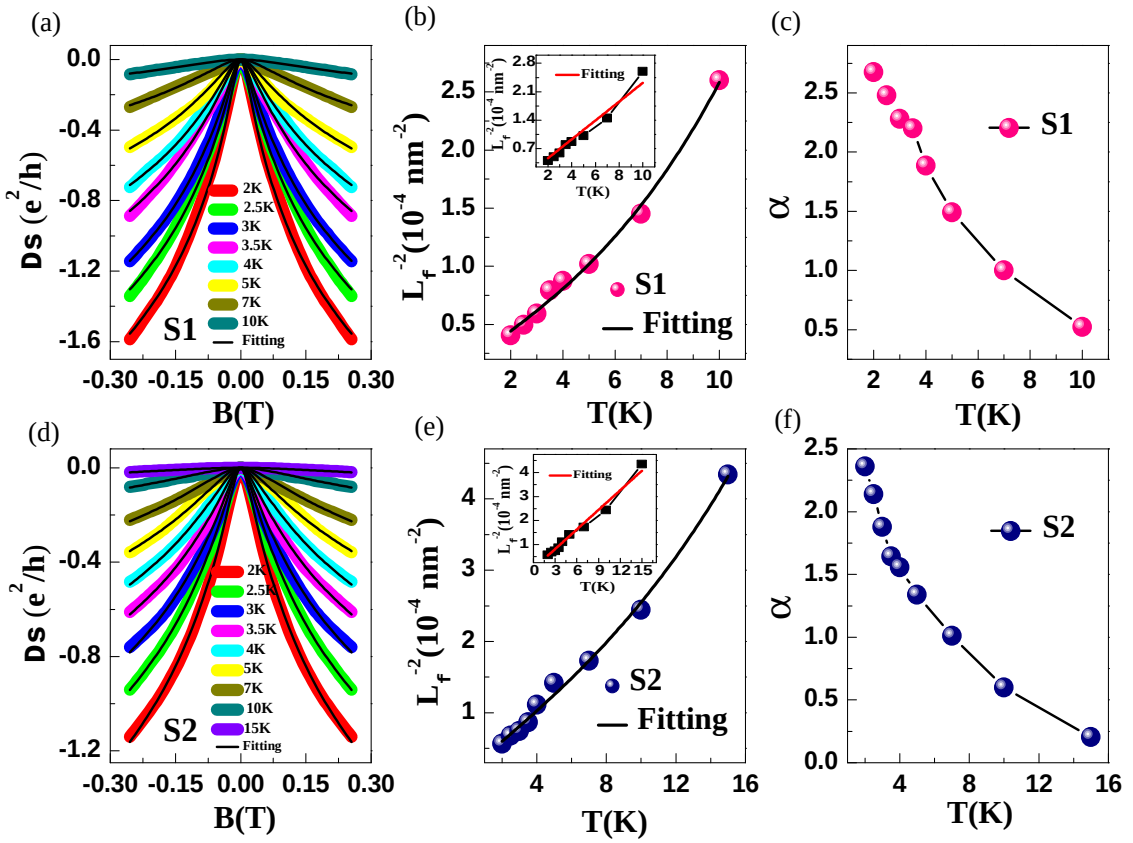

Figure 4.6: (a,d) The magneto-conductance ($\triangle\sigma$) at various temperatures for S1 and S2. Black lines show fitted data w.r.t HLN equation. (b,e) Variation of L_ϕ as a function of temperature, revealing the contribution of different scattering mechanisms. (c,f) Temperature dependence of α.

-1 for weak anti-localization (WAL) and localization (WL), respectively [78]. In particular, the value of α is 1/2 for one topological conduction channel. If more than one conduction channel is present, each adds up and gives the value of $\alpha >$ 1/2 [117, 136]. Our data agree well with HLN fitting, as shown in Fig. 4.6 (a).

The extracted values of α and L_ϕ as a function of temperature are shown in Fig. 4.6 (b-c). The value of α is 2.7 at T= 2 K, greater than the theoretical value expected for a single conduction channel, which implies the presence of more than one topological conducting channel. Figure 4.6 (c) shows the variation of α with temperature, following the trend already observed in some materials [25, 117, 136]. Figure 4.6 (b) shows the temperature variation of L_ϕ, which decreases from 157 nm at 2 K to 62 nm at 10 K. The Nyquist electron-electron theory has predicted the temperature variation of L_ϕ as $L_\phi \propto T^{-n/2}$ where n = 1 for 2D systems [137]. The inset of Fig. 4.6 (b) shows the $T^{-1/2}$ dependence of L_ϕ, which indicates the failure of the fitting. This suggests that several scattering mechanisms are involved

in dephasing the electron's phase in $Pd_3Bi_2Se_2$ thin films. To analyze different scattering mechanisms, we use an equation which is given below: [108]

$$\frac{1}{L_\phi^2} = \frac{1}{L_{\phi o}^2} + A_{ee}\, T^n + B_{ep}\, T^{n'} \tag{4.5}$$

where $L_{\phi o}$ represents the zero temperature dephasing length, $A_{ee}\ T^n$ and $B_{ep}\ T^{n'}$ represent the contributions from electron-electron and electron-phonon interactions, respectively. According to electron-phonon interaction theory, electron-phonon interaction should be n' $\geq$ 2 [109]. We have obtained a proper fit by considering the electron-phonon interaction, as illustrated by the solid black line in Fig. 6 (b). The index n' varies between 2-3, which reveals the presence of e-p scattering mechanism, consistent with the observations in $GeSb_2Te_4$.[110] The value of A_{ee} = 1.57 $\times\ 10^{-5}$ is large in comparison to the B_{ep} = 8.90 $\times\ 10^{-8}$, which suggests the dominance of the e-e scattering mechanism.

Figure 4.6 (d) shows the magnetic field dependence of conductance at various temperatures in the range of $\pm$ 0.25 T for the S2 sample. By applying the eq. 4, we have done fitting of magneto-conductance and extracted the parameters L_ϕ and α, as shown in fig. 4.6 (e-f). Figure 4.6 (e) shows the temperature dependence of L_ϕ, which decreases from 133 nm at 2 K to 48 nm at 15 K. Similar to the S1 sample, we have done the linear fitting of ${L_\phi}^{-2}$, which indicates the failure of the fitting. It suggests that several scattering mechanisms are involved in dephasing electron's phase. By considering the electron-phonon interaction, we have obtained a proper fit with n' = 3, as illustrated by the solid black line in Figure 4.6 (e), which reveals the presence of an e-p scattering mechanism.[109] The value of A_{ee} = 2.05 $\times\ 10^{-5}$ is large as compared to the value of B_{ep} = 3.18 $\times\ 10^{-8}$, which suggests the dominance of the e-e scattering mechanism. The value of α is 2.36 at T = 2 K, which is greater than the expected value. The $\alpha > 0.5$ indicates the presence of more than one topological non-trivial conduction channels.[136]

4.4 Conclusion

We report successful synthesis of thin films of the topological material $Pd_3Bi_2Se_2$. We have demonstrated that the linear energy dispersion causes unusual non-saturated

linear magnetoresistance coming from all the Dirac fermions inhabiting the lowest Landau level in the quantum limit. At a critical field $B^{\star}$, the transverse magnetoresistance shifts from semi-classical weak-field B^2 to high-field B dependence. The critical field $B^{\star}$ satisfies the quadratic temperature dependence, which is also expected from the Landau level splitting of a linear energy dispersion. Thus our results evince the existence of Dirac Fermions in $Pd_3Bi_2Se_2$. We also observed signatures of weak anti-localization (WAL). The magneto-conductivity data are satisfactorily analyzed in terms of the Hikami-Larkin-Nagaoka theory. It was found that the coefficient α (number of conduction channels) deviates from the value 0.5 expected for 2D systems with a single topological conduction channel. This indicates the contribution from additional topological conducting channels in the electron transport. Dependence of the dephasing length L_ϕ on temperature is also anomalous. We found that this behavior can be understood by including both the Nyquist electron-electron scattering and electron-phonon scattering as the phase relaxation mechanism in PBS films. The magnetoresistance data show deviations from Koehler's rule, suggesting multiple scattering mechanisms. Finally, the resistance versus temperature data show signatures consistent with a CDW transition. Such signatures have not been reported in previous works on bulk samples. These anomalous behaviors make $Pd_3Bi_2Se_2$ an interesting system for further study in various morphologies.

CHAPTER 5

Observation of Weak Anti-localization in thin films of the Topological Semimetal Candidate $PdSb_2$

5.1 Introduction

Fermionic particles and phenomena anticipated in high-energy physics have lately been discovered in condensed-matter systems; for example, Majorana fermions, as well as Dirac and Weyl fermions. These fermions are constrained by Poincaré invariance in high energy physics. However, in condensed-matter systems, fermions in crystals respect only the 230 crystal space groups symmetries rather than the Poincaré invariance. Hence, there is a possibility of realizing other fermions with no high-energy physics counterparts [37, 38, 39, 40]. Based on density functional theory (DFT) calculations, Bradlyn *etal.* have recently predicted the existence of such unconventional fermions having three, six, and eightfold degenerate band crossing in various materials [40]. $PdSb_2$ has been proposed to consist of such fermions with six-fold degenerate band crossing. Previous studies have confirmed the existence of sixfold degenerate band crossings by angle-resolved photoemission spectroscopy (ARPES) and density functional theory (DFT) [138, 139, 140]. Also, R. Chapai *et al.* have probed the presence of massless particles with non-trivial Berry phase by the de Hass-van oscillations in $PdSb_2$ single crystals [141].

In topological materials, the Berry phase associated with surface electrons suppresses backscattering and hence provides immunity to weak localization [123, 124,

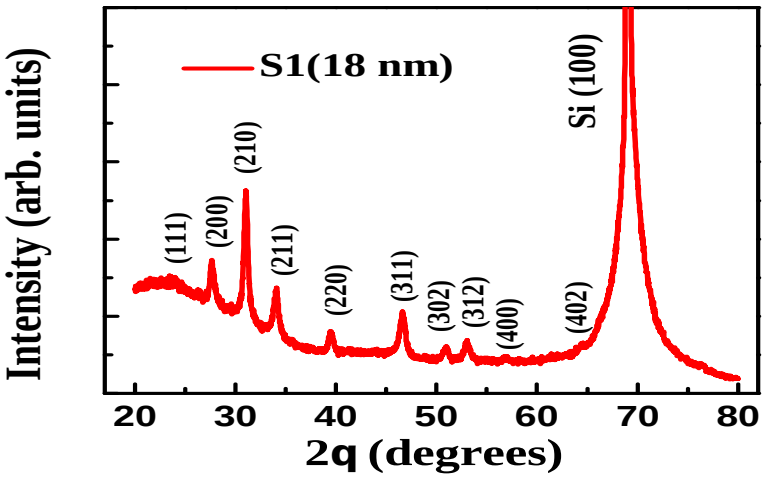

Figure 5.1: X-ray diffraction data for grown S1 thin films of $PdSb_2$.

125, 142]. This results in a quantum correction to conductivity whose temperature and magnetic field dependences are comparable to the weak anti-localization (WAL) effect in 2D systems [97, 98, 143, 144]. The WAL effect is reduced by applying an external magnetic field, which destroys the time-reversal symmetry and causes the electron to localize. WAL has been described by Hikami, Larkin, and Nagaoka (HLN) in two-dimensional systems [78, 83]. At low temperatures, the electron-electron interaction effect (EEI) has also been observed in various topological materials [145, 146, 147, 148, 149, 150]. The EEI effect can be used to determine the number of conducting transport channels [145]. Transport experiments often involve the non-negligible contribution from the bulk states, complicating the electronic probing of surface states. Therefore, the fabrication of thin films is a useful approach for reducing bulk contribution by raising the surface-to-volume ratio. The fabrication of $PdSb_2$ (PS) thin films using the pulsed laser deposition technique (PLD) and their magneto-transport properties will be discussed in this chapter.

5.2 Experimental Details

PS thin films were grown on a silicon (100) substrate in the Argon atmosphere using a pulsed laser (KrF excimer, λ = 248 nm). The laser ablation was performed on a polycrystalline PS target. PS thin film growth was carried out under optimal conditions, such as a pressure of the order of 10^{-1} m bar and a substrate temperature of 120°C. The phase purity of thin films was determined using an x-ray diffractometer (Bruker D8 Advance system with Cu-Kα radiation). Figure 5.1 shows the X-ray

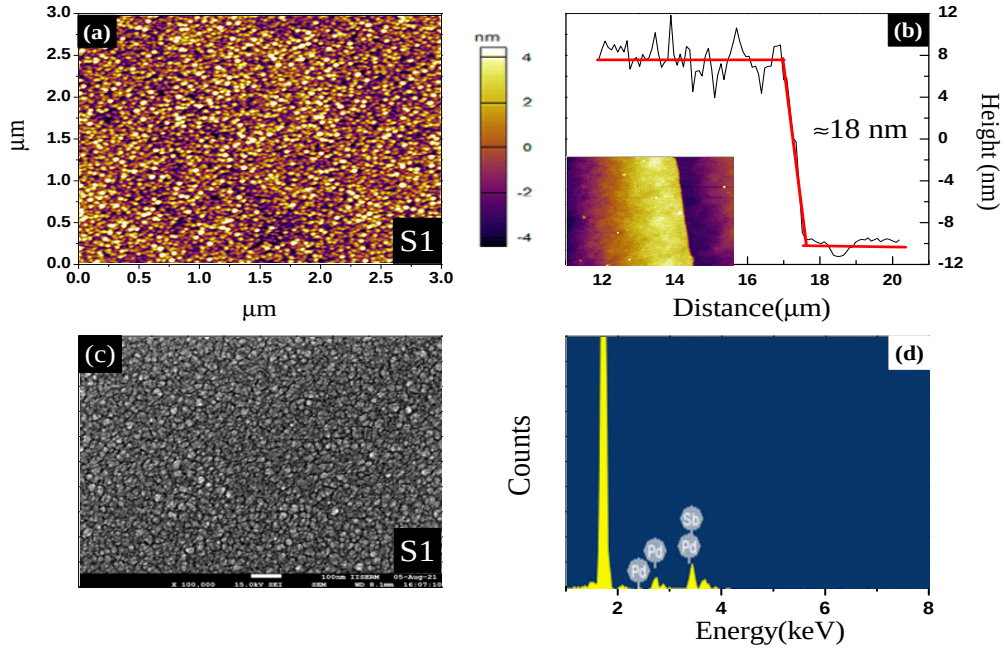

Figure 5.2: (a) Atomic Force microscope topographic image of PS thin films. (b) Height profile of S1 sample with thickness ≈ 18 nm. (c) SEM micro graphs of PS thin films obtained on Si (100) substrate. (d) EDS data.

diffraction (XRD) pattern of a PS thin film, confirming the cubic crystal structure with space group $Pa\bar{3}$ [138, 139, 140, 141]. We have grown PS thin films with different thickness. The PS thin films with thickness 18 nm and 10 nm are designated as S1, S2, respectively. Figure 5.2 (a) shows the atomic force microscope (AFM) image of thin film, which indicates the granular growth of the film. Figure 5.2 (b) shows the height profile of S1 thin film with thickness ≈ 18nm. The inset shows the topography image. Figure 5.2(c) shows the scanning electron microscopy (SEM) image of the thin film S1. The energy-dispersive x-ray spectroscopy (EDS) data confirms the stoichiometry of the compound, as shown in Fig. 5.2 (d). The PS thin films with thickness 18 nm and 10 nm are designated as S1, S2, respectively. The longitudinal and Hall resistances were measured in a Physical Property Measurement System (PPMS-Cryogenics) equipped with a 14T magnet.

5.3 Results and Discussion

Figure 5.3 shows the temperature variation of sheet resistance (R_S) for PS (S1, S2) thin films in various transverse magnetic fields. There is a decrease in sheet resistance with increased temperature, revealing the non-metallic type behavior of

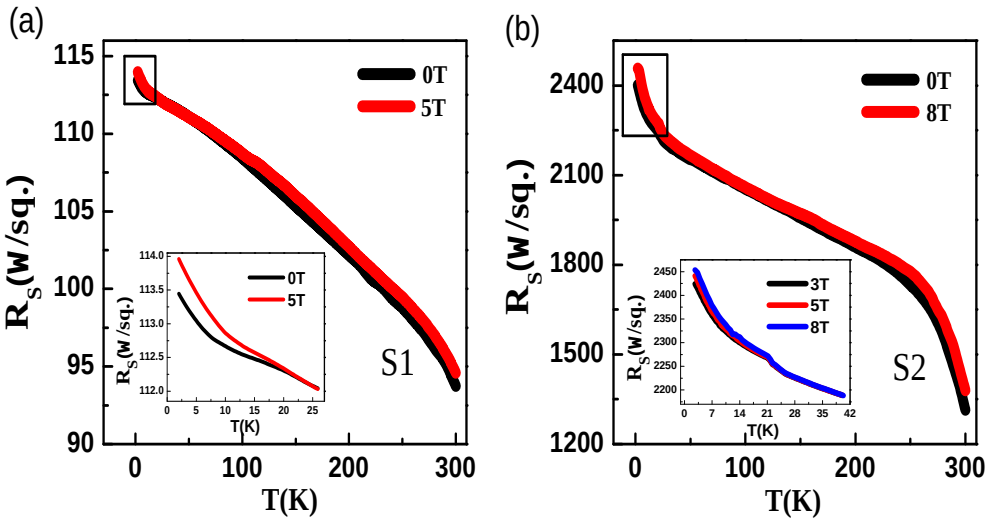

Figure 5.3: (a-b) Sheet resistance vs temperature at various magnetic fields showing the semi-conducting behavior of S1,S2 samples, Inset curve shows an upturn in sheet resistance at low temperatures for S1,S2.

PS thin films. The non-metallic behavior in resistivity contrasts with the metallic behavior observed in bulk materials. We postulate that this non-metallic behavior results from the quasi-low-dimensionality of the thin film. A change from metallic to insulating behavior on reducing thickness from bulk to quasi low dimensional has been reported previously [84, 146]. Below T = 20K, there is an upturn in sheet resistance, which may either be due to disorder-induced weak localization or electron-electron interaction in the two-dimensional limit [78, 145, 146]. We will return to discuss low-temperature upturn later.

Figure 5.4 shows the magneto-resistance (MR%) at various temperatures in the perpendicular magnetic field range of $\pm$ 7 T and $\pm$ 14 T for all films of PS, respectively. The sharp cusp type behavior around zero magnetic fields is observed in both samples, indicating the WAL effect in PS thin films [78, 83, 97, 98]. The low value of the magneto-resistance as compared to single crystals mainly corresponds to the low carrier mobility in PS thin films [141]. Before further discussions about WAL, we should consider the dimensionality of thin films. For Quantum interference (QI) effects, relevant length scale is phase coherence length (L_ϕ) which is equal to $\sqrt{D\tau}$. For the quantum diffusion regime, if $L\phi > t$, where 't' is the thickness of the film, then the quantum interference is quasi 2D in nature [104]. In our case, the value of L_ϕ is greater than the thickness of the thin film (based on the analysis below). Therefore, we restrict our analysis to the quasi 2D limit.

The magnetoconductance at various temperatures in the $\pm$ 0.5 T field is shown in Fig. 5.5 (a) for the S1 sample. The two dimensional conductance was found using

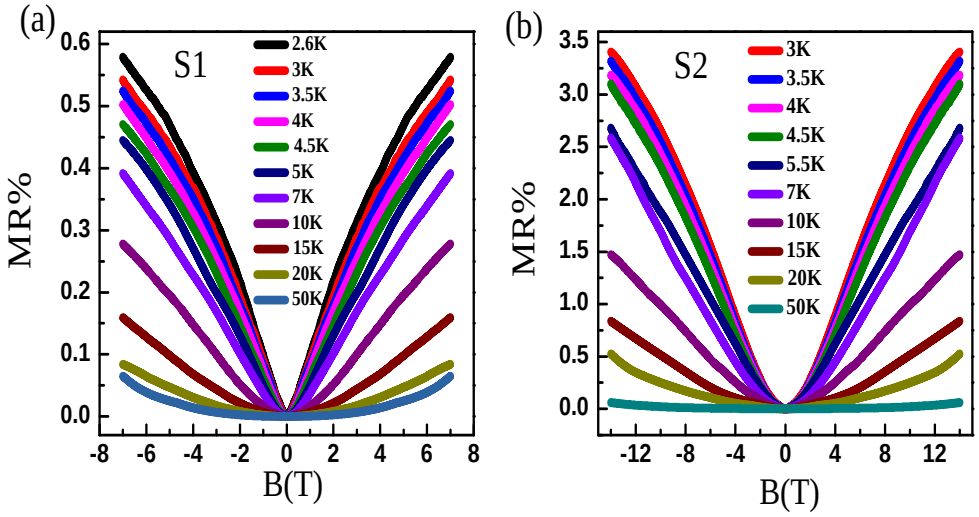

Figure 5.4: Magneto-resistance (MR%) vs magnetic field(B) at various temperatures in transverse configuration for S1,S2 sample.

$\triangle\sigma = \sigma(B)-\sigma(0)$ where $\sigma(B) = (L/W)\ (1/R_s)$, L and W are the length and width of sample respectively, R_s is the sheet resistance. The Hikami-Larkin-Nagaoka (HLN) equation can be used to describe the effect of localization in two-dimensional systems [78, 83]. For 2D systems, The HLN equation is given by

$$\triangle\ \sigma(B) = -\alpha\frac{e^2}{\pi h}\left[\psi\left(\frac{1}{2}+\frac{B_\phi}{B}\right) - \ln\left(\frac{B_\phi}{B}\right)\right] \tag{5.1}$$

where $\psi(x)$ is the digamma function, e is the electron charge, h is the Planck constant, B_ϕ is the characteristic field, which is required to destroy phase coherence. The characteristic field is associated with phase coherence length as $B_\phi = \hbar/(4eL_\phi^2)$, where $L_\phi = \sqrt{D\tau}$, D is the diffusion constant, and τ is the phase coherence time. The parameter α is related to conducting transport channels in a material. In accordance with HLN theory, the parameter α takes value 1/2 and -1 for weak anti-localization (WAL) and localization (WL), respectively.

By applying equation (2) to experimental curves, L_ϕ and α parameters are extracted for S1 as shown in fig. 5.5 (c,e). Figure 5.5 (c) shows the temperature dependence of L_ϕ of the S1 sample, which decreases from 41 nm at 2.6K to 7.5nm at 20K. Theoretically, the Nyquist electron-electron theory has predicted the variation of L_ϕ with temperature as $L_\phi \propto T^{-n/2}$ where n= 1 for 2D systems [107].

Figure 5.5 (c) inset curve shows the $T^{-1/2}$ dependence of L_ϕ, which indicates the failure of the fitting. This suggests that several scattering mechanisms are involved in dephasing the electron's phase in S1 thin films of PS. To analyze the temperature dependence of all scattering mechanisms, we will fit using a simple equation:[108]

$$\frac{1}{L_\phi^2} = \frac{1}{L_{\phi o}^2} + A_{ee}\, T^n + B_{ep}\, T^{n'} \tag{5.2}$$

where $L_{\phi o}$ is the temperature-independent dephasing length, $A_{ee}\ T^{n'}$ and $B_{ep}\ T^n$ represent the contributions from electron-electron (e-e) and electron-phonon (e-p) interactions, respectively. The value of n is 1 for electron-electron scattering [107]. According to electron-phonon interaction theory, electron-phonon interaction leads to $n \geq 2$ [109, 110]. By considering the electron-phonon interaction, we have obtained a proper fit with n' = 3 as illustrated by the solid black line in Fig. 5.5 (c), reveals the presence of both e-e scattering and e-p scattering mechanism. The value of $A_{ee} = 4.12 \times 10^{-4}$ is very large as compared to the value of $B_{ep} = 1.1555 \times 10^{-6}$, which suggests the dominance of the e-e scattering mechanism. The value of α is 0.5 at T = 2.6 K, which is in accordance with the theoretical value. Figure 5.5 (e) shows the variation of α as a function of temperature. It is clear from Fig. 5.5 (e), the number of conducting channels is strongly temperature-dependent. This indicates that at low temperatures, there is a good coupling between various surface topological conducting channels. As temperature is increased, decrease in coupling between various conducting channels occurs, which leads to increase in value of α [151, 152]. Above $\sim$ 10 K, α saturates to a value consistent with no. of conduction channels being 4-5.

Qualitatively, similar results were obtained for S2 as shown in Fig. 5.5 (b), (d), and (f). Figure 5(d) shows the temperature dependence of L_ϕ of the S2 sample, which decreases from 23 nm at 2.6 K to 7.6 nm at 20 K. By considering the electron-phonon interaction, we have obtained a proper fit with n' = 3 as illustrated by the solid black line in Figure 5.5 (d), which reveals the presence of both e-e scattering and e-p scattering mechanism [109]. The value of $A_{ee} = 3.95 \times 10^{-4}$ is very large as compared to the value of $B_{ep} = 1 \times 10^{-6}$, which suggests the dominance of the e-e scattering mechanism. The value of α is 0.13 at T = 3 K, which is less than the expected value. The low value of α indicates the presence of both topological

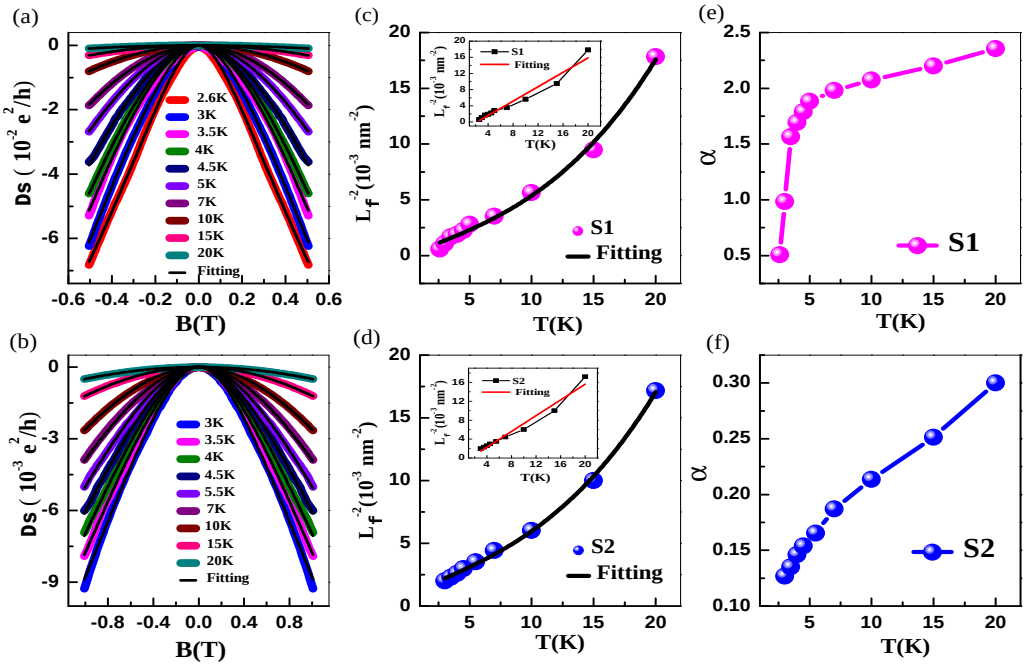

Figure 5.5: (a,b) Magnetic field dependence of magneto-conductance ($\triangle\sigma$) at various temperatures for S1 and S2. Black lines show fitted data w.r.t HLN equation. (c,d) Variation of L_ϕ as a function of temperature, revealing the contribution of different scattering mechanisms. (e,f) Temperature dependence of α.

trivial and non-trivial electrons,[117] or enhanced disorder. The low value of α has been observed for disordered thin films of other topological materials [153, 154].

Now we turn to the low temperature upturn in the resistance which was highlighted in the insets of fig. 5.3. The WAL dominated conductivity is expected to increase with lowering temperature without any external magnetic field [155]. However, the measured conductivity drops logarithmically as the temperature is lowered, as shown in fig. 5.6(a). This could arise either from disorder-induced weak localization (WL), or from electron-electron interaction effects. For the WL effect, magneto-conductivity should be positive, which is not observed in our case. This suggests that electron-electron interaction could be the possible mechanism for the anomalous rise in the resistance at low temperature [145, 146, 147, 148, 149]. The logarithmic T dependence of conductivity rules out the 3D theory for which we expect $\triangle\sigma = \sqrt{T}$ [98, 156]. Theoretically, 2D EEI correction to conductivity is given by

$$\delta\sigma = -\frac{e^2}{\pi h} n \left(1 - \frac{3}{4}F\right) \ln\left(\frac{T}{T_o}\right) = -\frac{e^2}{\pi h}\kappa \ln\left(\frac{T}{T_o}\right) \tag{5.3}$$

where n is no. of conduction channels and F is the screening factor, and T_o is the characteristic temperature at which electron-electron interaction effect vanishes.

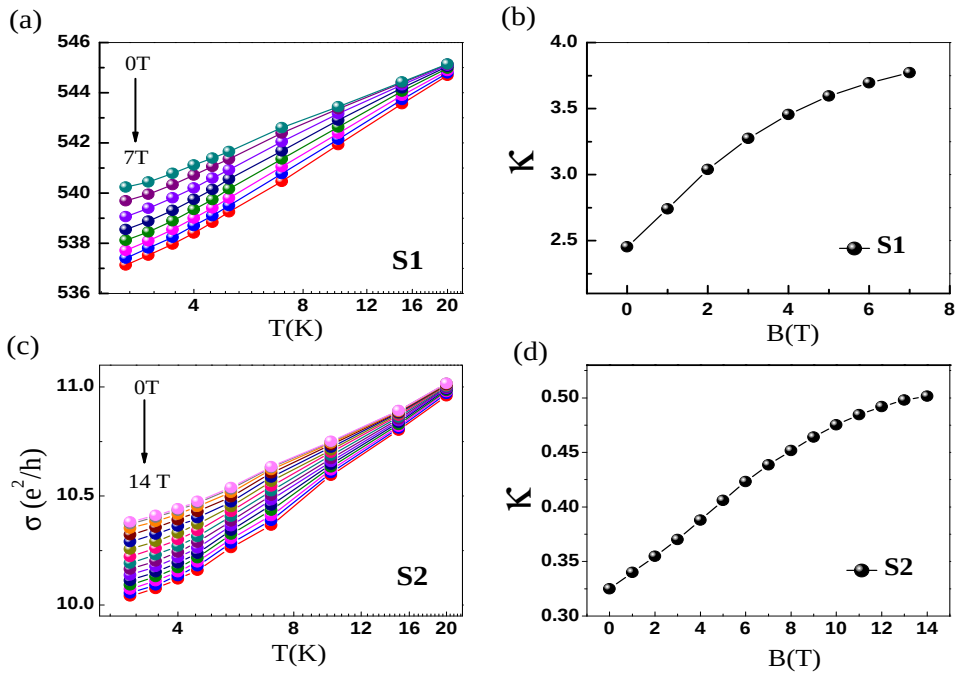

Figure 5.6: (a,c) Logarithmic temperature dependence of conductivity at low temperatures. The solid lines are guides for the eye. (b-d) shows the κ obtained by linear fitting the conductivity data shown in fig. (a,c) as function of magnetic field.

Figure 5.6 (a) shows the logarithmic temperature dependence of the conductivity for an S1 sample at various magnetic fields up to 7 T. By applying eq. 5.3, κ is obtained and is shown in Fig. 5.6 (b) as a function of the magnetic field. On increasing the magnetic field, the slope of the σ(T) curve increases and then tends to saturate. The saturated value of κ in the high field range indicates that the WAL is quenched. The saturated κ, referred to κ_{ee}, only includes the EEI correction to the conductivity at high field. According to the relation, κ = n(1-3F/4), the maximum (i.e., 3.76) of κ_{ee} requires n >2 to assure F $\geq$ 0. Then assuming n = 4, corresponding to four transport channels for the EEI effect, we obtain F = 0.08, which is comparable to the reported values of 0.15 and 0.32 [145]. This value of n is consistent with the estimates of n = 4-5 made from the WAL effect above.

Qualitatively similar results are obtained for S2, for which measurements were done in fields up to 14 T. Specifically, quenching of the WAL effect for high fields was observed as shown in fig. 5.6 (c). By applying Eq. 4, κ is obtained and shown as a function of field in fig. 5.6 (d). The high field value κ_{ee} = n(1-3F/4) $\approx$ 0.5 can be used to estimate the number of conduction channels. We have seen previously from the WAL analysis that the value of α was smaller than expected for a single conduction channel. This is most likely due to the enhanced disorder in the thinner

film. Assuming n = 1, corresponding to a single transport channel, we obtain F = 0.66, which is much larger than the value for S1 estimated above but is within the acceptable range of $0 \leq F \leq 1$. A high $F \sim 0.35$ has been previously reported for disordered WTe_2 films [157].

5.4 Conclusion

In conclusion, PS thin films with different thicknesses were grown on Si (100) substrate by the pulsed laser de-position (PLD) technique. To the best of our knowledge, PS thin films have been grown for the first time. We find that the magneto-conductivity at low temperatures has contributions from both the WAL and the EEI effects. An analysis of the WAL effect gives an idea about the thickness and temperature dependent coupling between various conduction channels (Topological surface state and trivial bulk states) in the material. Our results also elucidate the electron dephasing mechanisms. We find that both electron-electron and electron-phonon scattering mechanisms were responsible for electron dephasing effects in PS thin films. The EEI effect is also observed at low temperatures. From the EEI effect, we extracted the number of transport channels and found estimates in accordance with values obtained from the WAL effect. This suggests that the EEI effect can be used as an alternate method to estimate the number of conduction channels in materials where the WAL may not be observed.

CHAPTER 6

Planar Hall effect in the Ferromagnetic Weyl Semimetal $Co_3Sn_2S_2$

6.1 Introduction

Weyl semimetals (WSMs) have recently been discovered with relativistic bulk Weyl fermions, connected by topological surface Fermi-arcs (SFAs) [19, 158]. Unlike topological insulators (TIs) or Dirac semimetals (DSMs), WSMs can be realized by breaking certain symmetry such as the inversion symmetry (IS) or the time-reversal symmetry (TRS), or both. The unique electronic structures of WSMs give rise to unusual physical phenomena such as very high mobility, low carrier density, giant linear magnetoresistance (MR), anomalous Hall effect (AHE) and chiral anomaly, etc [19, 159, 160]. An earlier version of the WSMs were mostly nonmagnetic [23, 29, 35, 161]. However, several promising candidates for magnetic Weyl state have been proposed, such as $Y_2Ir_2O_7$, $HgCr_2Se_4$, Co_2 based Heusler alloys [162, 163, 164]. An anomalous Hall angle $\approx$ 16 % was observed in the magnetic-field-induced Weyl semimetal GdPtBi at low temperatures. Whereas, a finite external magnetic field is imperative to make GdPtBi a Weyl semimetal [165]. Therefore, the search for Weyl semimetals with intrinsic magnetic behavior and Weyl nodes close to the Fermi level has begun to obtain materials exhibiting both a high anomalous Hall conductivity and large anomalous Hall angle. In particular, the kagome lattice with out-of-plane magnetization is an excellent platform for

investigating the quantum anomalous Hall effect [166, 167].

$Co_3Sn_2S_2$ is a shandite compound, which is also known to be a ferromagnet with curie temperature $\approx$ 177 K with c axis as the easy axis of magnetization [168, 169, 170, 171]. The $Co_3Sn_2S_2$ crystal retains a quasi-2D Co_3Sn layer, which is sandwiched between sulfur atoms with the magnetic cobalt atoms arranged on a kagome lattice in a–b plane. Therefore, Enke Liu *et al.* has reported a magnetic Weyl semimetal in the kagome-lattice compound $Co_3Sn_2S_2$ with out-of-plane ferromagnetic order, and demonstrate both a large intrinsic anomalous Hall conductivity (1130 $\Omega^{-1}cm^{-1}$) and Chiral anomaly with negative longitudinal magnetoresistance (MR) $\approx$ 2%.[72] Previously negative longitudinal magnetoresistance (NLMR) in collinear magnetic and electric fields has been regarded as a possible signature of the chiral anomaly expected in these WSMs [60, 172, 173, 174]. However, Negative MR can result from many extrinsic mechanisms such as current jetting and crystal inhomogeneity. A direct cause and effect link between the observation of a negative MR and the presence of the chiral anomaly is still debated [34, 63, 175, 176, 177, 178].

Recent theoretical calculations on the WSM have predicted another transport signature of the chiral anomaly. An unusual Hall effect is predicted and observed when a magnetic field is applied in the plane of the current and the voltage contacts [179, 180, 181]. In this planar geometry, the Lorentz force does not play any role. Starting with a magnetic field parallel to the current I, the voltage oscillates with minima and maxima at 45 ° and 135 °, respectively, as the magnetic field is rotated in the plane. This effect is known as the planar Hall effect (PHE), as the Hall voltage is generated by the coplanar current and magnetic field. Recently, a very large PHE has been observed in some DSM and WSM materials [101, 182, 183, 184, 185, 186]. On the other hand, recent experimental findings suggest that PHE can be observed even if the signature of the chiral anomaly are masked by other contributions because the PHE does not depend on the position of the chemical potential from the Weyl nodes [183, 187]. In this chapter, we report the observation of a large PHE in single crystals of the recently discovered magnetic Weyl semimetal $Co_3Sn_2S_2$.

6.2 Experimental Details

The crystal structure of $Co_3Sn_2S_2$ was confirmed by powder x-ray diffraction on crushed single crystals. The reitveld refinement using fullprof software was used

to refine the crystal structure. Figure (6.1) shows the observed and calculated XRD data, confirming the single phase of $Co_3Sn_2S_2$ crystals with space group R-3m. The lattice parameters obtained from the refined structure, are $a = b = 5.3666$ Å, c=13.165 Å, $\alpha = \beta = 90°$, and $\gamma = 120°$, which are close to the values reported in literature [168, 169, 170, 171]. The stoichiometry of crystal was confirmed by energy dispersive x-ray spectroscopy (EDS) using scanning electron microscope as shown in fig. 6.2.

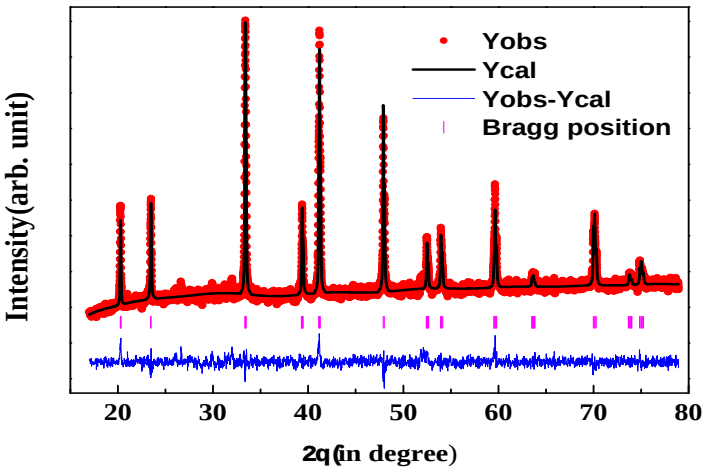

Figure 6.1: The X-ray diffraction pattern of $Co_3Sn_2S_2$ with Rietveld refinement. The Red circles, black line, blue line, and magenta bar marks represent observed, calculated, background (the difference between observed and calculated) and Bragg positions, respectively.

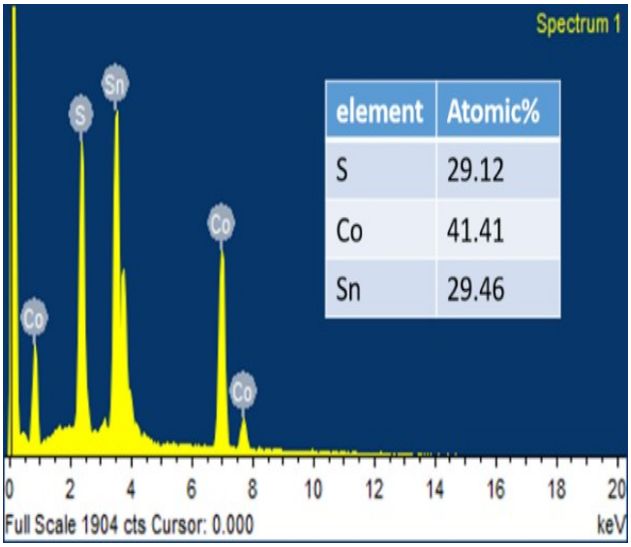

Figure 6.2: The energy dispersive X-ray spectroscopy image with atomic percentage shown in Table.

6.3 Results and Discussion

Figure 6.3 (a) shows magnetization vs. temperature at various magnetic fields. It is clear from fig. 6.3 (a), our single crystals show a ferromagnetic transition with a $T_C \approx 175$K. Figure 6.3 (b) shows the magnetization vs. magnetic field at various temperatures, revealing a strong magnetic anisotropy between the in-plane and out-of-plane magnetic field orientations. While the out of plane magnetization (B ∥ c) saturates in a small field B = 0.1T, the in-plane magnetization (B ∥ ab) does not saturate even up to B = 7T (see inset in fig. 6.3 (b)). This confirms the dominance of out-of-plane magnetic ordering in this compound, consistent with previous studies on this compound [171]. Figure 6.3 (c) and (d) show the resistivity ρ(T) at various magnetic fields. The ρ(T) follows a typical metallic character with a value at 2 K of ρ(2K)= 45 $\mu\Omega$cm and at 300 K value of ρ(300K) = 1168 $\mu\Omega$ cm. The residual resistivity ratio RRR = ρ(300 K)/ ρ(2 K) = 26 is significantly higher than the value of reported previously [72, 171], which indicates the high quality of single crystals. The ferromagnetic transition at $T_C \approx 175$K appears as a kink in the ρ(T) data, as shown in fig. 6.3 (c). Fig. 6.3 (d) shows that the kink in the ρ(T) moves up in temperature and broadens on applying a magnetic field.

Figure 6.4 (a) shows the magnetoresistance at various angles between current and magnetic field at T = 2K. For the B ∥ c configuration, the MR is positive and non-saturating, as shown in fig. 6.4 (a). The value of MR is 160 % at a field of 9 T, which is higher than the value previously reported [72]. A large non-saturating MR is a characteristic feature of compensated semimetals. The MR (B ∥ c) is parabolic in nature at low fields and becomes linear at higher fields. The parabolic MR in weak fields confirms the three-dimensional nature of the charge carriers in $Co_3Sn_2S_2$. Fig. 6.4 (a) confirms the absence of NLMR in the B ∥ I configuration at temperature T = 2K. The absence of NLMR in our sample might be due to the large value of the orbital MR in the B ∥ c configuration. It must be pointed out that the magnitude of the previously reported NLMR in B ∥ I configuration was only 2% at T = 2K, which can be easily mask by large (160%) orbital MR in our case. However, we did not observe a negative MR in our experiment at a low temperature. We do observe a negative MR at higher temperatures close to T_C (175 K) shown in fig. 6.4 (b), which may be due to suppression of spin disorder scattering in magnetic fields.

Figure 6.4 (c) and (d) show the Hall effect data taken at different temperatures. The measured Hall data is anti-symmetrized to remove the contribution of the orbital MR. A hysteric behavior can be seen in the Hall resistivity at low tempera-

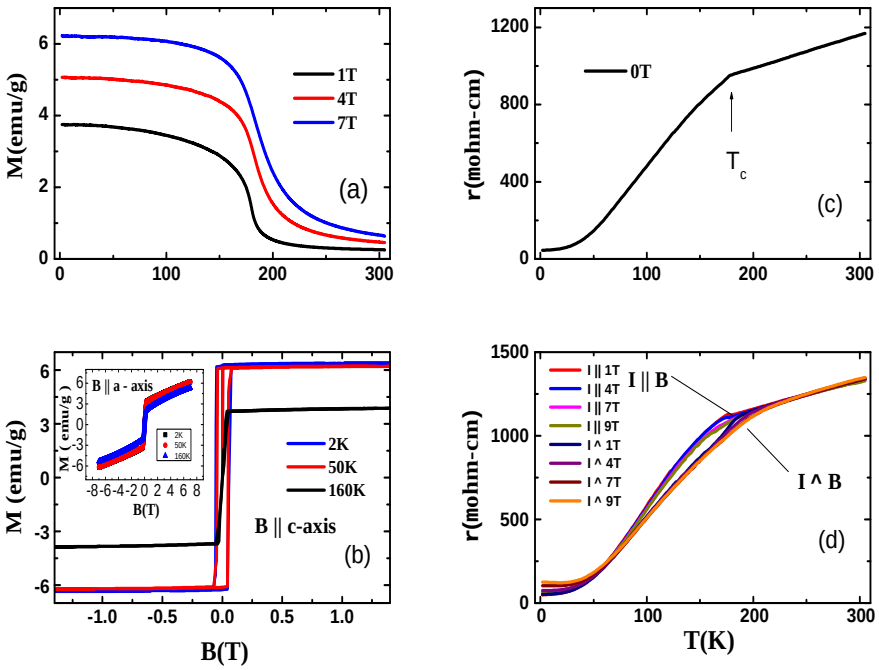

Figure 6.3: (a) Temperature (T) dependent magnetization (M) data at different magnetic fields B ∥ c-axis (b) M vs B at various temperatures for B ∥ c-axis and (inset) M vs B for B ∥ ab plane (c) Resistivity (ρ) vs T data at 0 T showing a kink at ferromagnetic transition temperature (d) The ρ(T)for various B with current I ∥ B and I ⊥ B.

tures, which is a signature of the anomalous Hall effect. Figure 6.4 (d) shows the low field zoomed-in version of the rectangular hysteresis loop of Hall data shown in fig. 6.4 (c). The coercive field at 2 K is 0.5T, decreasing with increasing temperature, as expected for a ferromagnetic material. The anomalous Hall conductivity ${\sigma_H}^A$ is calculated using the expression ${\sigma_H}^A = {\rho_H}^A/({\rho_H}^A)^2 + \rho^2)$, where ${\rho_H}^A$ and ρ are the anomalous Hall resistivity at zero field and the zero-field resistivity, respectively. The value of ${\rho_H}^A$ was calculated by extrapolating the linear high field part of the Hall resistivity to zero fields. At 2 K, the value of ${\sigma_H}^A$ is found to be 1266 $(\Omega\text{cm})^{-1}$. Additionally, we observe nonlinearity in the Hall resistivity at high fields, which indicates the presence of two types of carriers.

Figure 6.5 (a) and (c) show the planar Hall resistivity ρ_{xy}^{PHE} and longitudinal resistivity (ρ_{xx}) data as a function of ϕ at T = 2K. We have averaged the ρ_{xy}^{PHE} data measured at positive and negative magnetic fields to remove the contribution of the normal Hall resistivity. It can be seen from fig. 6.5 (a) that ρ_{xy}^{PHE} increases with increasing magnetic field. As predicted theoretically for PHE, ρ_{xy}^{PHE} shows minima and maxima near ϕ = 45 ° and 135 °, respectively. The position of minima and maxima is consistent with previously reported PHE results on other DSMs

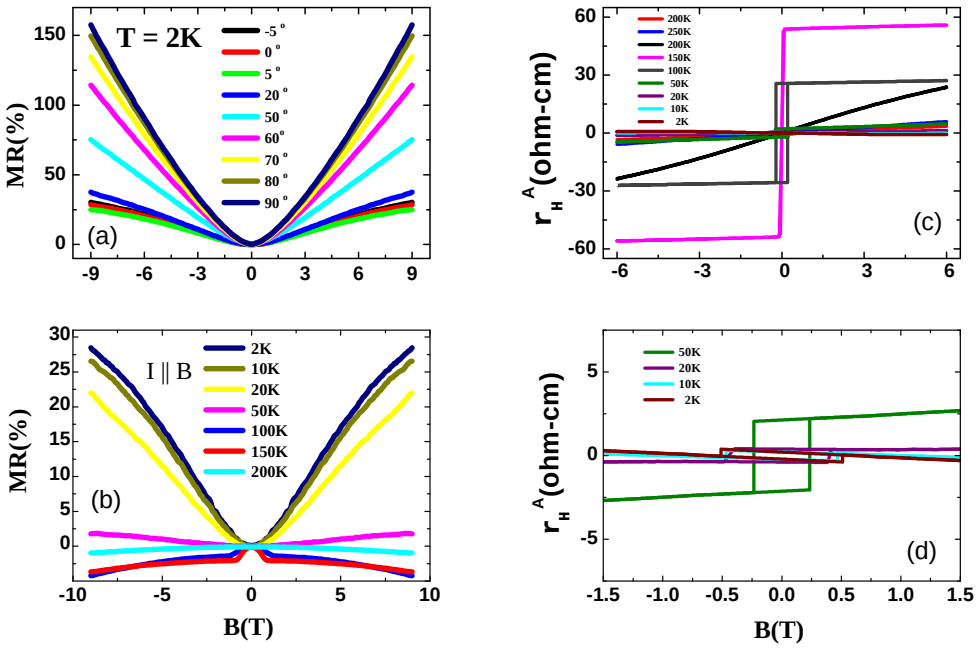

Figure 6.4: (a) MR data at various angles between current (I) and magnetic field (B) (b) Longitudinal (B ∥ I) MR at various temperatures (c) Anomalous Hall resistivity $\rho_H{}^A$ vs B at various Temperatures (d) An expanded plot of $\rho_H{}^A$ vs B to highlight the behavior at low fields and temperatures.

such as $ZrTe_5$, Cd_3As_2, VAl_3, GdPtBi, and $MoTe_2$ [101, 182, 183, 184, 185]. The contribution of chiral anomaly to ρ_{xy}^{PHE} and ρ_{xx} is given below [179, 180, 181],

$$\rho^{PHE} = \triangle\rho^{Chiral} \sin\phi \cos\phi + b \tag{6.1}$$

$$\rho_{xx} = \rho_{\perp} - \triangle\rho^{Chiral} \cos^2\phi \tag{6.2}$$

where $\triangle\rho^{Chiral}$ = $\rho_{\perp}$ - $\rho_{\parallel}$ is the chiral anomaly induced resistivity, $\rho_{\perp}$ and $\rho_{\parallel}$ are the transverse (ϕ = 90°) and longitudinal (ϕ = 0°) resistivity in the planar Hall measurement geometry. The constant b accounts for the anisotropic MR resulting from any small misalignment. The data in fig. 6.5 (a) and (c) were fitted by the above expressions and the chiral resistivity ($\triangle\rho^{Chiral}$) and the transverse resistivity ($\rho_{\perp}$) were extracted at each magnetic field. The fits to Eqs. (1) and (2) are shown in the inset of fig. 6.5 (b) and (d), respectively. The obtained $\triangle\rho^{Chiral}$ and $\rho_{\perp}$ are plotted versus the magnetic field in fig. 6.5 (b) and (d). Both $\triangle\rho^{Chiral}$ and $\rho_{\perp}$ show a monotonically increasing trend with increasing magnetic field. We have fitted the magnetic field dependence to a power law (B^n). The extracted values of the

exponents are found to be nearly quadratic (n = 2) for both $\triangle\rho^{Chiral}$ and $\rho_{\perp}$. These values are similar to exponents obtained in other DSM and WSM materials [183].

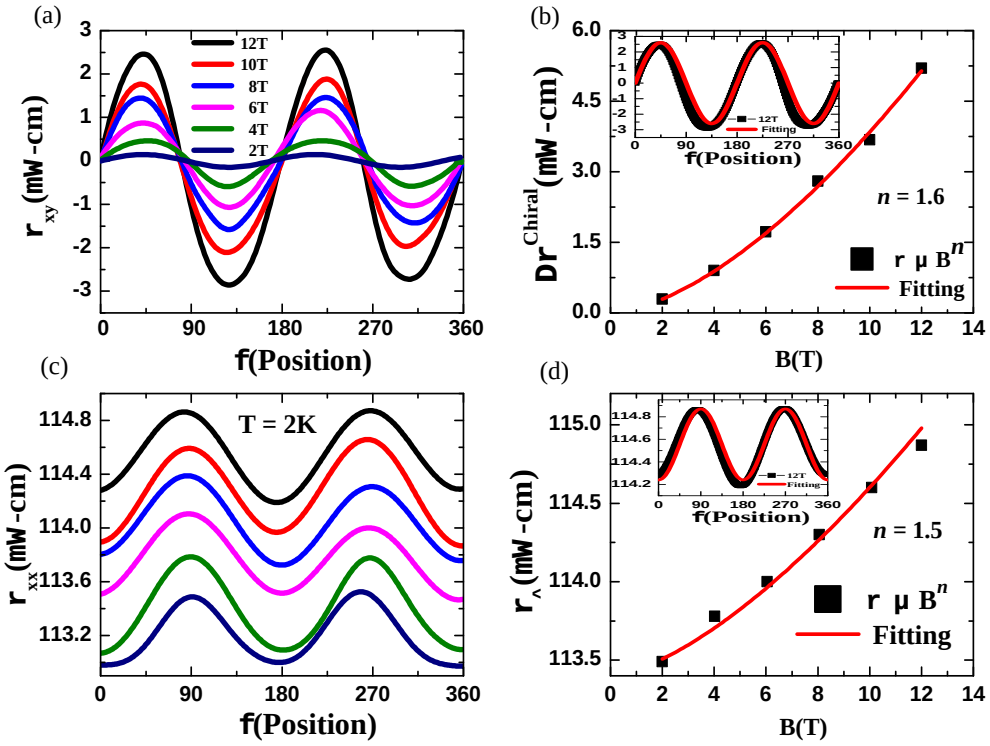

Figure 6.5: (a) The planar Hall resistivity ρ_{PHE} and (b) the longitudinal resistivity ρ_{xx} vs angle ϕ measured at T = 2K in various magnetic fields. (c) Extracted chiral contribution $\triangle\rho^{Chiral}$ vs magnetic field. (d) Extracted $\rho_{\perp}$ vs magnetic field. The solid curves through the data in (c) and (d) are fits to a power law field dependence B^n. Insets in (c) and (d) show the fitting of ρ_{PHE} and ρ_{xx} data at 12 T to the Eqs.(1) and (2), respectively.

The data in fig. 6.5 (a) demonstrates the presence of the PHE in $Co_3Sn_2S_2$. However, given that the material shows a ferromagnetic ordering below T_C= 175K, it is unclear whether the PHE in $Co_3Sn_2S_2$ is related to the topological character of the material or the ferro-magnetism. Previous studies of the PHE in ferromagnetic materials have shown that the PHE, if present due to ferro-magnetism, tracks the magnetization and is observed in the ordered state but vanishes at the ferromagnetic critical temperature. We have therefore tracked the temperature dependence of the PHE in $Co_3Sn_2S_2$. Fig. 6.6 (a) shows the temperature-dependent $\triangle\rho_{xy}^{PHE}$ measured in 12 T at various temperatures, and fig. 6.6 (b) shows the chiral contribution extracted from these data. It can be seen from the data that the chiral contribution decreases on increasing the temperature. We performed a phenomenological fit to the data by the expression $\triangle\rho^{Chiral}$ = A +B T^m, where A, B, and m are fit parameters. This fit is extrapolated to $\triangle\rho^{Chiral}$ = 0 at T $\approx$ 174K. This demonstrates that

the PHE signal vanishes at a temperature close to the ferromagnetic ordering temperature T_C = 175 K, thereby suggesting that the origin of the PHE is most likely related to the ferromagnetism and not the Chiral anomaly.

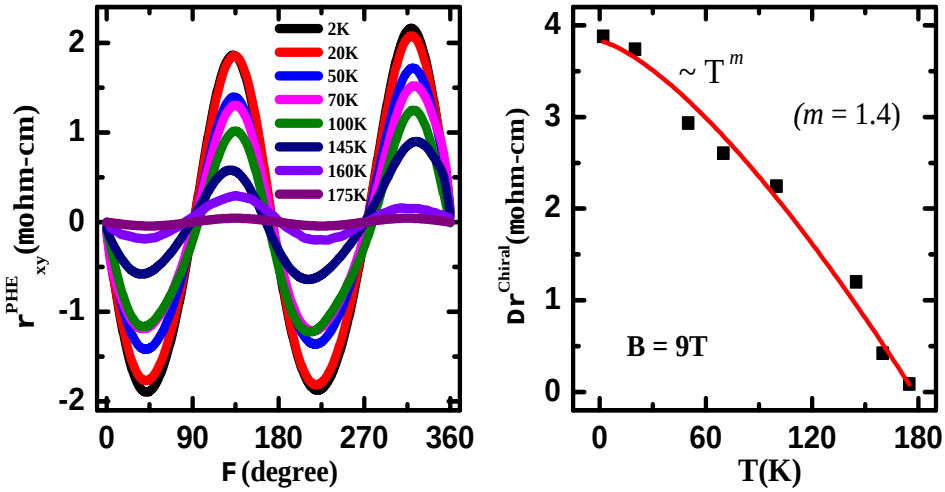

Figure 6.6: a) Planar Hall resistivity ρ_{PHE} vs angle ϕ, measured at various temperatures in a magnetic field of 9 T. (b) The extracted chiral contribution $\triangle\rho^{Chiral}$ to the PHE vs temperature T. The solid curve through the data is a power law fit.

6.4 Conclusion

We have grown high-quality (RRR=26) single crystals of the recently discovered magnetic Weyl semimetal $Co_3Sn_2S_2$. We confirm a large intrinsic anomalous Hall conductivity of the order of 1266 $(\Omega\ \text{cm})^{-1}$ for our crystals which provides strong evidence for the topological band structure of this compound. However, we did not observe the chiral anomaly-induced NLMR reported previously for these materials even though our crystals show a larger RRR than reported previously. We note that the NLMR reported previously is only 2 %, which could be easily masked by a large orbital MR, as observed in our measurements. It has recently been pointed out theoretically that the planar Hall effect could be more direct evidence of the non-trivial band structure of a Weyl semimetal. Therefore, we looked for and observed a large PHE for our $Co_3Sn_2S_2$ crystals. However, the temperature dependence of the PHE signal showed that the signal vanished close to the ferromagnetic T_C = 174 K, which suggests that the origin of the PHE signal could be magnetic anisotropy in the ferromagnetic state rather than the Chiral anomaly. In conclusion, we did not observe any magneto-transport signature of the topological character of charge carriers in $Co_3Sn_2S_2$.

CHAPTER 7

Summary and Outlook

7.1 Summary

Topological materials, including topological insulators, topological semimetals, topological superconductors, etc., host phases of matter which cannot be characterized by classical order parameters but by topological invariants. Topological materials have been shown to exhibit exotic physical properties such as giant magneto-resistance, Fermi arc surface states, high mobility, non-trivial Berry phase, chiral anomaly induced negative magneto-resistance, etc. These novel properties promise useful applications such as high-speed electronics, better catalysts, spintronic, magnetic storage devices, fault-tolerant Quantum computation, etc. The signature of Topological surface states in electrical transport measurements is often masked by the contributions from topologically trivial bulk conduction channels. This necessitates the use of advanced measurement techniques like angle-resolved photoemission spectroscopy to identify new Topological materials. In this thesis, we show that by synthesizing the Topological materials in the thin film form, we can reduce the relative contribution of the bulk states and reveal contributions from Topological surface states. Therefore, the fabrication of thin films is an effective technique to reduce the bulk contribution by increasing the surface-to-volume ratio. We have grown the thin films of a few specific topological materials such as $Pd_3Bi_2S_2$, $Pd_3Bi_2Se_2$, $PdSb_2$, and single crystals of quasi-two-dimensional $Co_3Sn_2S_2$. We use

detailed magneto-transport measurements to reveal various electrical-transport phenomena, which are consequences of the non-trivial Topology of electronic states in these materials.

In our study, the detailed magnetotransport measurements on thin films (93 nm) of the novel topological semimetal $Pd_3Bi_2S_2$ grown by pulsed laser deposition has been carried out. $Pd_3Bi_2S_2$ have been theoretically proposed to consist of exotic fermions having three-fold degenerate band crossing at P point, which is only 0.1 eV above the Fermi level. However, evidence for topological surface states has not yet been revealed in transport measurements due to large mobility of bulk charge carriers. The longitudinal resistance measurements on PBS thin films indicate a disordered metallic system, resulting in reduced mobility of bulk carriers as compared to single crystals. This inhibits the bulk contribution and allows the first detection of transport contribution from topological surface states through the observation of the 2D WAL effect. The WAL data measured for magnetic fields applied at different angles to the current direction, all scale with the perpendicular component of the magnetic field, confirming the contribution of 2D topological surface states to the WAL. The magnetotransport data is analyzed within the 2D Hikami-Larkin-Nagaoka (HLN) theory. The analysis indicates that multiple conduction channels contribute to electrical transport. It is also found that the temperature dependence of the phase dephasing length can't be unraveled only by electron-electron scattering and that electron-phonon scattering also contributes to the phase relaxation mechanism in $Pd_3Bi_2S_2$ films. These anomalous behaviours in transport measurements make $Pd_3Bi_2S_2$ an interesting system for further study in various morphologies.

The second part of the thesis focuses on the growth and probing of the non-trivial states in thin films of topological material $Pd_3Bi_2Se_2$. The linear energy dispersion causes unusual non-saturated linear magnetoresistance since all Dirac fermions inhabit the lowest Landau level in the quantum limit. At a critical field $B^\star$, the transverse magnetoresistance shifts from semi-classical weak-field B^2 dependence to high-field B dependency. The critical field $B^\star$ satisfies the quadratic temperature dependency, which is ascribed to the Landau level splitting of linear energy dispersion. Also, we observed a sharp cusp-like behavior in magneto-conductance at low temperatures, which is a hallmark of weak anti-localization (WAL). These results are satisfactorily analyzed in terms of the Hikami-Larkin-Nagaoka theory. The α (no. of conducting channels) deviates from the theoretical value, revealing the contribution of additional topological conducting channels in electron transport. The temperature dependence of phase dephasing length can be understood by including both the Nyquist electron-electron scattering and electron-phonon scattering as the

phase relaxation mechanism in $Pd_3Bi_2Se_2$ films. This magnetotransport study suggests the presence of Dirac Fermions in $Pd_3Bi_2Se_2$ which can lead to application in the field of spintronics.

In third part, detailed magnetotransport study has been done on thin films of topological semimetal candidate $PdSb_2$, which has been predicted to host exotic fermions with six fold degenerate band crossing. We find that the magneto-conductivity at low temperatures has contributions from both the WAL and the EEI effects. An analysis of the WAL effect gives an idea about the thickness and temperature dependent coupling between various conduction channels (Topological surface state and trivial bulk states) in the material. Our results also elucidate the electron dephasing mechanisms. We find that both electron-electron and electron-phonon scattering mechanisms were responsible for electron dephasing effects in PS thin films. The EEI effect is also observed at low temperatures. From the EEI effect, we extracted the number of transport channels and found estimates in accordance with values obtained from the WAL effect. This suggests that the EEI effect can be used as an alternate method to estimate the number of conduction channels in materials where the WAL may not be observed.

The last part of the thesis is concerned with magnetotransport study on high-quality single crystals of the recently discovered magnetic Weyl semimetal $Co_3Sn_2S_2$. We confirm a large intrinsic anomalous Hall conductivity of the order of 1266 $(\Omega\ \text{cm})^{-1}$ for our crystals which provides strong evidence for the topological band structure of this compound. However, we did not observe the chiral anomaly-induced NLMR reported previously for these materials even though our crystals show a larger RRR than reported previously. We note that the NLMR reported previously is only 2 %, which could be easily masked by a large orbital MR, as observed in our measurements. It has recently been pointed out theoretically that the planar Hall effect could be more direct evidence of the nontrivial band structure of a Weyl semimetal. Therefore, we looked for and observed a large PHE for our $Co_3Sn_2S_2$ crystals. However, the temperature dependence of the planar Hall effect signal showed that the signal vanished close to the ferromagnetic T_C = 174 K, which suggests that the origin of the planar Hall effect signal could be magnetic anisotropy in the ferromagnetic state rather than the Chiral anomaly. This indicates that the observed planar Hall effect can't be connected to the topological character of charge carriers in $Co_3Sn_2S_2$.

7.2 Outlook

Research on topological phases of matter has dramatically escalated due to the non-trivial band structure that topological material can host and possible applications in spintronics and quantum computation. There are some challenges in the research field of topological materials. One of these challenges is searching for ideal topological semimetals with Dirac/ Weyl points close to the Fermi level, making it easier to understand the Dirac/Weyl points physics from transport measurements. Several materials such as $Y_2Ir_2O_7$, $HgCr_2Se_4$, and Co-based magnetic Heusler compounds are proposed to be magnetic Weyl semimetal but not confirmed experimentally. That may be because their Weyl points are far from Fermi level, making it difficult to detect Weyl points dominated physics from transport measurements. For example, $Pd_3Bi_2S_2$ (studied in the present thesis) consists of band crossing point 0.1 eV away from Fermi level, which complicates the observation of topological signatures in transport measurements. Recently, another member of the ternary family, a magnetic Weyl semimetal $Co_3Sn_2S_2$ came into the picture in which Weyl points are 60 meV above and below the Fermi level. In this direction, it has been suggested that doping of materials can cause crossing points to approach the Fermi level. This work is currently in progress in our Novel Materials Lab. It also offers a good platform for the study of topological phase transition along with magnetic phase transition. Moreover, owing to the layered lattice structure, the ternary family of compounds is also a good candidate for thin film growth and to incorporate into heterostructures, which may play a vital role in the future utilization of topological materials in electronic devices.

Bibliography

[1] D. J. Thouless, M. Kohmoto, M. P. Nightingale, and M. den Nijs, Phys. Rev. Lett. **49**, 405 (1982).

[2] M. Nakahara, Adam Hilger, Bristol etc (1990).

[3] K. v. Klitzing, G. Dorda, and M. Pepper, Phys. Rev. Lett. **45**, 494 (1980).

[4] R. E. Prange and S. M. Girvin, Springer, New York, 1987 https://link.springer.com/book/10.1007/978-1-4684-0499-9.

[5] L. LANDAU and E. LIFSHITZ, Butterworth-Heinemann, Oxford, 1980 https://www.elsevier.com/books/statistical-physics/landau/978-0-08-057046-4.

[6] K. v. Klitzing, Philos. Trans. R. Soc. London **363**, 10.1098/rsta.2005.1640 (2005).

[7] M. V. Berry, Proceedings of Royal Society A **392**, rspa.1984.0023 (1983).

[8] S. Murakami, N. Nagaosa, and S.-C. Zhang, Science **301**, 1348 (2003).

[9] C. L. Kane and E. J. Mele, Phys. Rev. Lett. **95**, 226801 (2005).

[10] B. A. Bernevig and S.-C. Zhang, Phys. Rev. Lett. **96**, 106802 (2006).

[11] X. L. Qi and S. C. Zhang, Physics Today **63**, 33 (2010).

[12] C. L. Kane and E. J. Mele, Phys. Rev. Lett. **95**, 146802 (2005).

[13] L. Fu and C. L. Kane, Phys. Rev. B **74**, 195312 (2006).

[14] M. König, S. Wiedmann, C. Brüne, A. Roth, H. Buhmann, L. W. Molenkamp, X. L. Qi, and S. C. Zhang, Science **318**, 766 (2007).

[15] L. Fu, C. L. Kane, and E. J. Mele, Phys. Rev. Lett. **98**, 106803 (2007).

[16] D. Hsieh, D. Qian, L. Wray, Y. Xia, Y. S. Hor, R. J. Cava, and M. Z. Hasan, Nature **452**, 970 (2008).

[17] Y. Xia, D. Qian, D. Hsieh, L. Wray, A. Pal, H. Lin, A. Bansil, D. Grauer, Y. S. Hor, R. J. Cava, and M. Z. Hasan, Nat. Phys. **5**, 398 (2009).

[18] Y. L. Chen, J. G. Analytis, J.-H. Chu, Z. K. Liu, S. K. Mo, X. L. Qi, H. J. Zhang, D. H. Lu, X. Dai, Z. Fang, S. C. Zhang, I. R. Fisher, Z. Hussain, and Z. X. Shen, Science **325**, 178 (2009).

[19] N. P. Armitage, E. J. Mele, and A. Vishwanath, Rev. Mod. Phys. **90**, 015001 (2018).

[20] Z. Wang, Y. Sun, X.-Q. Chen, C. Franchini, G. Xu, H. Weng, X. Dai, and Z. Fang, Phys. Rev. B **85**, 195320 (2012).

[21] A. A. Burkov, Nat. Mater. **15**, 1145 (2016).

[22] S. M. Young, S. Zaheer, J. C. Y. Teo, C. L. Kane, E. J. Mele, and A. M. Rappe, Phys. Rev. Lett. **108**, 140405 (2012).

[23] S.-M. Huang, S.-Y. Xu, I. Belopolski, C.-C. Lee, G. Chang, B. Wang, N. Alidoust, G. Bian, M. Neupane, C. Zhang, S. Jia, A. Bansil, H. Lin, and M. Z. Hasan, Nat. Commun. **6**, 7373 (2015).

[24] T. Liang, Q. Gibson, M. N. Ali, M. Liu, R. J. Cava, and N. P. Ong, Nat. Mater. **14**, 280 (2014).

[25] X. Huang, L. Zhao, Y. Long, P. Wang, D. Chen, Z. Yang, H. Liang, M. Xue, H. Weng, Z. Fang, X. Dai, and G. Chen, Phys. Rev. X **5**, 031023 (2015).

[26] Y. Ando, J. Phys. Soc. Japan **82**, 102001 (2013).

[27] S. Murakami, New J. Phys. **9**, 356 (2007).

[28] S. M. Young, S. Chowdhury, E. J. Walter, E. J. Mele, C. L. Kane, and A. M. Rappe, Phys. Rev. B **84**, 085106 (2011).

[29] S.-Y. Xu, Y. Xia, L. A. Wray, S. Jia, F. Meier, J. H. Dil, J. Osterwalder, B. Slomski, A. Bansil, H. Lin, R. J. Cava, and M. Z. Hasan, Science **332**, 560 (2011).

[30] M. Brahlek, N. Bansal, N. Koirala, S.-Y. Xu, M. Neupane, C. Liu, M. Z. Hasan, and S. Oh, Phys. Rev. Lett. **109**, 186403 (2012).

[31] J. A. Steinberg, S. M. Young, S. Zaheer, C. L. Kane, E. J. Mele, and A. M. Rappe, Phys. Rev. Lett. **112**, 036403 (2014).

[32] Z. Wang, H. Weng, Q. Wu, X. Dai, and Z. Fang, Phys. Rev. B **88**, 125427 (2013).

[33] H. Weyl, Zeitschrift für Physik **56**, 330 (1929).

[34] H. Weng, C. Fang, Z. Fang, B. A. Bernevig, and X. Dai, Phys. Rev. X **5**, 011029 (2015).

[35] B. Q. Lv, H. M. Weng, B. B. Fu, X. P. Wang, H. Miao, J. Ma, P. Richard, X. C. Huang, L. X. Zhao, G. F. Chen, Z. Fang, X. Dai, T. Qian, and H. Ding, Phys. Rev. X **5**, 031013 (2015).

[36] S. Y. Xu, I. Belopolski, N. Alidoust, M. Neupane, G. Bian, C. Zhang, R. Sankar, G. Chang, Z. Yuan, C. C. Lee, S. M. Huang, H. Zheng, J. Ma, D. S. Sanchez, B. Wang, A. Bansil, F. Chou, P. P. Shibayev, H. Lin, S. Jia, and M. Z. Hasan, Science **349**, 613 (2015).

[37] G. Chang, B. J. Wieder, F. Schindler, D. S. Sanchez, I. Belopolski, S.-M. Huang, B. Singh, D. Wu, T. R. Chang, T. Neupert, S. Y. Xu, H. Lin, and M. Z. Hasan, Nat. Mater. **17**, 978 (2018).

[38] F. Tang, H. C. Po, A. Vishwanath, and X. Wan, Nature **566**, 486 (2019).

[39] T. Zhang, Y. Jiang, Z. Song, H. Huang, Y. He, Z. Fang, H. Weng, and C. Fang, Nature **566**, 475 (2019).

[40] B. Bradlyn, J. Cano, Z. Wang, M. G. Vergniory, C. Felser, R. J. Cava, and B. A. Bernevig, Science **353**, 6299 (2016).

[41] B. Q. Lv, Z.-L. Feng, Q.-N. Xu, X. Gao, J.-Z. Ma, L.-Y. Kong, P. Richard, Y.-B. Huang, V. N. Strocov, C. Fang, H.-M. Weng, Y.-G. Shi, T. Qian, and H. Ding, Nature **546**, 627 (2017).

[42] D. S. Sanchez, I. Belopolski, T. A. Cochran, X. Xu, J.-X. Yin, G. Chang, W. Xie, K. Manna, V. Süß, C.-Y. Huang, N. Alidoust, D. Multer, S. S. Zhang, N. Shumiya, X. Wang, G.-Q. Wang, T.-R. Chang, C. Felser, S.-Y. Xu, S. Jia, H. Lin, and M. Z. Hasan, Nature **567**, 500 (2019).

[43] N. B. M. Schröter, D. Pei, M. G. Vergniory, Y. Sun, K. Manna, F. de Juan, J. A. Krieger, V. Süss, M. Schmidt, P. Dudin, B. Bradlyn, T. K. Kim, T. Schmitt, C. Cacho, C. Felser, V. N. Strocov, and Y. Chen, Nat. Phys. **15**, 759 (2019).

[44] N. Kumar, M. Yao, J. Nayak, M. G. Vergniory, J. Bannies, Z. Wang, N. B. M. Schröter, V. N. Strocov, L. Müchler, W. Shi, E. D. L. Rienks, J. L. Mañes, C. Shekhar, S. S. P. Parkin, J. Fink, G. H. Fecher, Y. Sun, B. A. Bernevig, and C. Felser, Adv. Mater. **32**, 1906046 (2020).

[45] A. A. Abrikosov, NorthHolland, Amsterdam, (1988).

[46] W. Gao, N. Hao, F.-W. Zheng, W. Ning, M. Wu, X. Zhu, G. Zheng, J. Zhang, J. Lu, H. Zhang, C. Xi, J. Yang, H. Du, P. Zhang, Y. Zhang, and M. Tian, Phys. Rev. Lett. **118**, 256601 (2017).

[47] M. N. Ali, J. Xiong, S. Flynn, J. Tao, Q. D. Gibson, L. M. Schoop, T. Liang, N. Haldolaarachchige, M. Hirschberger, N. P. Ong, and R. J. Cava, Nature **514**, 205 (2014).

[48] C. M. Hurd, (Plenum Press, New York, 1972) (1972).

[49] Amit, R. K. Singh, N. Wadehra, S. Chakraverty, and Y. Singh, Phys. Rev. Materials **2**, 114202 (2018).

[50] Y. Zhao, H. Liu, C. Zhang, H. Wang, J. Wang, Z. Lin, Y. Xing, H. Lu, J. Liu, Y. Wang, S. M. Brombosz, Z. Xiao, S. Jia, X. C. Xie, and J. Wang, Phys. Rev. X **5**, 031037 (2015).

[51] M. M. Parish and P. B. Littlewood, Nature **426**, 162 (2003).

[52] A. A. Abrikosov, Phys. Rev. B **58**, 2788 (1998).

[53] H. Wang, H. Su, J. Zhang, W. Xia, Y. Lin, X. Liu, X. Hou, Z. Yu, N. Yu, X. Wang, Z. Zou, Y. Wang, Q. Liang, Y. Zhen, and Y. Guo, Phys. Rev. B **100**, 115127 (2019).

[54] Shama, R. Gopal, and Y. Singh, Journal of Magnetism and Magnetic Materials **502**, 166547 (2020).

[55] S. L. Adler, Phys. Rev. **177**, 2426 (1969).

[56] J. S. Bell and R. Jackiw, Il Nuovo Cimento A (1965-1970) **60**, 47 (1969).

[57] H. Nielsen and M. Ninomiya, Physics Letters B **130**, 389 (1983).

[58] H.-J. Kim, K.-S. Kim, J.-F. Wang, M. Sasaki, N. Satoh, A. Ohnishi, M. Kitaura, M. Yang, and L. Li, Phys. Rev. Lett. **111**, 246603 (2013).

[59] Z. Wang, Y. Zheng, Z. Shen, Y. Lu, H. Fang, F. Sheng, Y. Zhou, X. Yang, Y. Li, C. Feng, and Z.-A. Xu, Phys. Rev. B **93**, 121112 (2016).

[60] J. Xiong, S. K. Kushwaha, T. Liang, J. W. Krizan, M. Hirschberger, W. Wang, R. J. Cava, and N. P. Ong, Science **350**, 413 (2015), https://www.science.org/doi/pdf/10.1126/science.aac6089 .

[61] Q. Li, D. E. Kharzeev, C. Zhang, Y. Huang, I. Pletikosić, A. V. Fedorov, R. D. Zhong, J. A. Schneeloch, G. D. Gu, and T. Valla, Nat. Phys. **12**, 550 (2019).

[62] K. Yoshid, J. Appl. Phys. **50**, 4159 (1979).

[63] R. D. dos Reis, M. O. Ajeesh, N. Kumar, F. Arnold, C. Shekhar, M. Naumann, M. Schmidt, M. Nicklas, and E. Hassinger, New Journal of Physics **18**, 085006 (2016).

[64] S. Nandy, G. Sharma, A. Taraphder, and S. Tewari, Phys. Rev. Lett. **119**, 176804 (2017).

[65] R. Karplus and J. M. Luttinger, Phys. Rev. **95**, 1154 (1954).

[66] M.-C. Chang and Q. Niu, Phys. Rev. B **53**, 7010 (1996).

[67] G. Sundaram and Q. Niu, Phys. Rev. B **59**, 14915 (1999).

[68] T. Jungwirth, Q. Niu, and A. H. MacDonald, Phys. Rev. Lett. **88**, 207208 (2002).

[69] J. Smit and J. Volger, Phys. Rev. **92**, 1576 (1953).

[70] S. Onoda, N. Sugimoto, and N. Nagaosa, Phys. Rev. B **77**, 165103 (2008).

[71] A. A. Burkov, Phys. Rev. Lett. **113**, 187202 (2014).

[72] E. Liu, Y. Sun, N. Kumar, L. Muechler, A. Sun, L. Jiao, S.-Y. Yang, D. Liu, A. Liang, Q. Xu, J. Kroder, V. Süß, H. Borrmann, C. Shekhar, Z. Wang, C. Xi, W. Wang, W. Schnelle, S. Wirth, Y. Chen, S. T. B. Goennenwein, and C. Felser, Nat. Phys. **14**, 1125 (2018).

[73] T. Liang, J. Lin, Q. Gibson, S. Kushwaha, M. Liu, W. Wang, H. Xiong, J. A. Sobota, M. Hashimoto, P. S. Kirchmann, Z.-X. Shen, R. J. Cava, and N. P. Ong, Nat. Phys. **14**, 451 (2018).

[74] Y. Zhu, B. Singh, Y. Wang, C.-Y. Huang, W.-C. Chiu, B. Wang, D. Graf, Y. Zhang, H. Lin, J. Sun, A. Bansil, and Z. Mao, Phys. Rev. B **101**, 161105 (2020).

[75] M. Z. Hasan and C. L. Kane, Rev. Mod. Phys. **82**, 3045 (2010).

[76] J. E. Moore, Nature **464**, 194 (2010).

[77] K. Nomura, M. Koshino, and S. Ryu, Phys. Rev. Lett. **99**, 146806 (2007).

[78] S. Hikami, A. I. Larkin, and Y. Nagaoka, Progress of Theoretical Physics **63**, 707 (1980).

[79] S.-Q. Shen, Phys. Rev. B **70**, 081311 (2004).

[80] H. Suzuura and T. Ando, Phys. Rev. Lett. **89**, 266603 (2002).

[81] E. McCann, K. Kechedzhi, V. I. Fal'ko, H. Suzuura, T. Ando, and B. L. Altshuler, Phys. Rev. Lett. **97**, 146805 (2006).

[82] G. Tkachov and E. M. Hankiewicz, Phys. Rev. B **84**, 035444 (2011).

[83] L. Fang, J. Im, W. DeGottardi, Y. Jia, A. Glatz, K. A. Matveev, W. K. Kwok, G. W. Crabtree, and M. G. Kanatzidis, Sci. Rep. **6**, 35313 (2016).

[84] B. Zhao, P. C. andHaiyang Pan, S. Zhang, G. W. Baigeng Wang, F. Xiu, and F. Song, Sci. Rep. **6**, 22377 (2016).

[85] G. Xu, W. Wang, X. Zhang, Y. Du, E. Liu, S. Wang, G. Wu, Z. Liu, and X. X. Zhang, Scientific Reports **4**, 5709 (2014).

[86] Z. Xie, X. Wei, S. Cao, Y. Zhang, S. Yan, G. D. Gu, Q. Li, and J.-H. Chen, Phys. Rev. B **103**, 155408 (2021).

[87] A. R. West, (Wiley, 2014) (2014).

[88] B. D. Cullity and S. R. Stock, (Prentice Hall New Jersey, 2001) (2001).

[89] B. H. Toby, J. Appl. Cryst. **34**, 210 (2001).

[90] A. Larson and R. V. Dreele, Los. Alamos National Laboratory Report LAUR **86**, 748 (2004).

[91] S. Foner, Rev. Sci. Instrum. **30**, 548 (1959).

[92] Q. design, magnetic property measurement system manual technical report , 1004 ().

[93] Q. design, Resistivity measurement system manual technical report , 1076 ().

[94] T. Sakamoto, M. Wakeshima, Y. Hinatsu, and K. Matsuhira, Phys. Rev. B **78**, 024509 (2008).

[95] M. Roslova, L. Opherden, I. Veremchuk, L. Spillecke, H. Kirmse, T. Hermannsdörfer, J. Wosnitza, T. Doert, and M. Ruck, Inorg. Chem. **55**, 8808 (2016).

[96] S. Roy, A. Pariari, R. Singha, B. Satpati, and P. Mandal, Appl. Phys. Lett. **112**, 162402 (2018).

[97] G. Bergmann, Phys. Rep. **1**, 1 (1913).

[98] P. A. Lee and T. V. Ramakrishnan, Rev. Mod. Phys. **57**, 287 (1985).

[99] P. A. Lee, A. D. Stone, and H. Fukuyama, Phys. Rev. B **35**, 1039 (1987).

[100] H.-Z. Lu and S.-Q. Shen, Phys. Rev. B **84**, 125138 (2011).

[101] H. Li, H.-W. Wang, H. He, J. Wang, and S.-Q. Shen, Phys. Rev. B **97**, 201110 (2018).

[102] N. Bansal, Y. S. Kim, M. Brahlek, E. Edrey, and S. Oh, Phys. Rev. Lett. **109**, 116804 (2012).

[103] J. M. Ziman, (Oxford University Press, 1960) (1960).

[104] Z. Ovadyahu, Y. Gefen, and Y. Imry, Phys. Rev. B **32**, 781 (1985).

[105] W. E. Lawrence and A. B. Meador, Phys. Rev. B **18**, 1154 (1978).

[106] Z. Li, I. Garate, J. Pan, X. Wan, T. Chen, W. Ning, X. Zhang, F. Song, Y. Meng, X. Hong, X. Wang, L. Pi, X. Wang, B. Wang, S. Li, M. A. Reed, L. Glazman, and G. Wang, Phys. Rev. B **91**, 041401 (2015).

[107] C.-Y. Wu, B.-T. Lin, Y.-J. Zhang, Z.-Q. Li, and J.-J. Lin, Phys. Rev. B **85**, 104204 (2012).

[108] J. J. Lin and J. P. Bird, J. Phys. Condens. Matter **14**, R501 (2002).

[109] A. Sergeev, B. S. Karasik, N. G. Ptitsina, G. M. Chulkova, K. S. Il'in, and E. M. Gershenzon, Physica B **263**, 190 (1999).

[110] N. P. Breznay, H. Volker, A. Palevski, R. Mazzarello, A. Kapitulnik, and M. Wuttig, Phys. Rev. B **86**, 205302 (2012).

[111] K. Shrestha, D. Graf, V. Marinova, B. Lorenz, and C. W. Chu, Journal of Applied Physics **122**, 145901 (2017).

[112] J. J. Cha, D. Kong, S.-S. Hong, J. G. Analytis, K. Lai, and Y. Cui, Nano Letters **12**, 1107 (2012).

[113] H.-T. He, G. Wang, T. Zhang, I.-K. Sou, G. K. L. Wong, J.-N. Wang, H.-Z. Lu, S.-Q. Shen, and F.-C. Zhang, Phys. Rev. Lett. **106**, 166805 (2011).

[114] T. Sakamoto, M. Wakeshima, Y. Hinatsu, and K. Matsuhira, Phys. Rev. B **75**, 060503 (2007).

[115] E. Y. Zakharova, S. M. Kazakov, and A. N. Kuznetsov, Journal of Alloys and Compounds **651**, 193 (2015).

[116] J. Lapano, Y.-Y. Pai, A. R. Mazza, J. Zhang, T. Isaacs-Smith, P. Gemperline, L. Zhang, H. Li, H. N. Lee, G. Eres, M. Yoon, R. Comes, T. Z. Ward, B. Lawrie, M. A. McGuire, R. G. Moore, C. T. Nelson, A. F. May, and M. Brahlek, APL Materials **9**, 101110 (2021).

[117] S. , R. K. Gopal, G. Sheet, and Y. Singh, Sci. Rep. **11**, 12618 (2021).

[118] A. A. A. Abrikosov, (North- Holland, Amsterdam,, 1988) (1988).

[119] Y. Zhang, Y. W. Tan, and H. Stormer, Nature **438**, 201 (2005).

[120] D. L. Miller, K. D. Kubista, G. M. Rutter, M. Ruan, W. A. de Heer, P. N. First, and J. A. Stroscio, Science **324**, 924 (2009).

[121] D. X. Qu, Y. S. Hor, J. Xiong, R. J. Cava, and N. P. Ong, Science **329**, 821 (2010).

[122] K. K. Huynh, Y. Tanabe, and K. Tanigaki, Phys. Rev. Lett. **106**, 217004 (2011).

[123] P. Roushan, J. Seo, C. V. Parker, Y. S. Hor, D. Hsieh, D. Qian, A. Richardella, M. Z. Hasan, R. J. Cava, and A. Yazdani, Nature **460**, 1106 (2009).

[124] P. M. Ostrovsky, I. V. Gornyi, and A. D. Mirlin, Phys. Rev. Lett. **105**, 036803 (2010).

[125] H.-Z. Lu and S.-Q. Shen, Phys. Rev. B **84**, 125138 (2011).

[126] H. Jin, K. Lee, S.-H. Baek, J.-S. Kim, B.-k. Cheong, B. H. Park, S. Yoon, B. J. Suh, C. Kim, S. S. A. Seo, and S. Lee, Sci. Rep. **6**, 34295 (2016).

[127] Y. Singh, R. Nirmala, S. Ramakrishnan, and S. K. Malik, Phys. Rev. B **72**, 045106 (2005).

[128] Y. Singh, D. Pal, S. Ramakrishnan, A. M. Awasthi, and S. K. Malik, Phys. Rev. B **71**, 045109 (2005).

[129] N. F. Mott, Philosophical Magazine **19**, 835 (1969).

[130] R. Xu, A. Husmann, T. F. Rosenbaum, M. L. Saboungi, J. E. E. Enderby, and P. B. Littlewood, Nature **390**, 57 (1997).

[131] M. Lee, T. F. Rosenbaum, M.-L. Saboungi, and H. S. Schnyders, Phys. Rev. Lett. **88**, 066602 (2002).

[132] W. Zhang, R. Yu, W. Feng, Y. Yao, H. Weng, X. Dai, and Z. Fang, Phys. Rev. Lett. **106**, 156808 (2011).

[133] K. Wang, D. Graf, H. Lei, S. W. Tozer, and C. Petrovic, Phys. Rev. B **84**, 220401 (2011).

[134] K. Wang, D. Graf, L. Wang, H. Lei, S. W. Tozer, and C. Petrovic, Phys. Rev. B **85**, 041101 (2012).

[135] P. W. Anderson, E. Abrahams, and T. V. Ramakrishnan, Phys. Rev. Lett. **43**, 718 (1979).

[136] H. Cao, C. Liu, J. Tian, Y. Xu, I. Miotkowski, M. Z. Hasan, and Y. P. Chen, arxiv.org **1409**, 3217 (2014).

[137] C.-Y. Wu, B.-T. Lin, Y.-J. Zhang, Z.-Q. Li, and J.-J. Lin, Phys. Rev. B **85**, 104204 (2012).

[138] Z. P. Sun, C. Q. Hua, X. L. Liu, Z. T. Liu, M. Ye, S. Qiao, Z. H. Liu, J. S. Liu, Y. F. Guo, Y. H. Lu, and D. W. Shen, Phys. Rev. B **101**, 155114 (2020).

[139] N. Kumar, M. Yao, J. Nayak, M. G. Vergniory, J. Bannies, Z. Wang, N. B. M. Schröter, V. N. Strocov, L. Müchler, W. Shi, E. D. L. Rienks, J. L. Manes, C. Shekhar, S. S. P. Parkin, J. Fink, G. H. Fecher, Y. Sun, B. A. Bernevig, and C. Felser, Advanced Materials **32**, 1906046 (2020).

[140] X. Yáng, T. A. Cochran, R. Chapai, D. Tristant, J.-X. Yin, I. Belopolski, Z. b. u. b. a. Chéng, D. Multer, S. S. Zhang, N. Shumiya, M. Litskevich, Y. Jiang, G. Chang, Q. Zhang, I. Vekhter, W. A. Shelton, R. Jin, S.-Y. Xu, and M. Z. Hasan, Phys. Rev. B **101**, 201105 (2020).

[141] R. Chapai, Y. Jia, W. A. Shelton, R. Nepal, M. Saghayezhian, J. F. DiTusa, E. W. Plummer, C. Jin, and R. Jin, Phys. Rev. B **99**, 161110 (2019).

[142] H. T. He, G. Wang, T. Zhang, I. K. Sou, G. K. L. Wong, J. N. Wang, H. Z. Lu, S. Q. Shen, and F. C. Zhang, Phys. Rev. Lett. **106**, 166805 (2011).

[143] E. McCann, K. Kechedzhi, V. I. Fal'ko, H. Suzuura, T. Ando, and B. L. Altshuler, Phys. Rev. Lett. **97**, 146805 (2006).

[144] G. Tkachov and E. M. Hankiewicz, Phys. Rev. B **84**, 035444 (2011).

[145] J. Wang, A. M. DaSilva, C.-Z. Chang, K. He, J. K. Jain, N. Samarth, X.-C. Ma, Q.-K. Xue, and M. H. W. Chan, Phys. Rev. B **83**, 245438 (2011).

[146] M. Liu, C.-Z. Chang, Z. Zhang, Y. Zhang, W. Ruan, K. He, L.-l. Wang, X. Chen, J.-F. Jia, S.-C. Zhang, Q.-K. Xue, X. Ma, and Y. Wang, Phys. Rev. B **83**, 165440 (2011).

[147] J. Chen, X. Y. He, K. H. Wu, Z. Q. Ji, L. Lu, J. R. Shi, J. H. Smet, and Y. Q. Li, Phys. Rev. B **83**, 241304 (2011).

[148] Y. Takagaki, B. Jenichen, U. Jahn, M. Ramsteiner, and K.-J. Friedland, Phys. Rev. B **85**, 115314 (2012).

[149] S.-P. Chiu and J.-J. Lin, Phys. Rev. B **87**, 035122 (2013).

[150] A. Roy, S. Guchhait, S. Sonde, R. Dey, T. Pramanik, A. Rai, H. C. P. Movva, L. Colombo, and S. K. Banerjee, Applied Physics Letters **102**, 163118 (2013).

[151] W. Wang, K. Gao, and Z. Li, Sci. Rep. **6**, 25291 (2016).

[152] J. C. M. Protyush Sahu, Jun-Yang Chen and J.-P. Wang, Appl. Phys. Lett. **112**, 122402 (2018).

[153] M. Brahlek, N. Koirala, and S. Oh, Solid State Commun. **215–216**, 54–62 (2015).

[154] J. Liao, Y. Ou, X. Feng, S. Yang, C. Lin, W. Yang, K. Wu, K. He, X. Ma, Q. K. Xue, and Y. Li, Phys. Rev. Lett. **114**, 216601 (2015).

[155] H. Lu and S. Shen, Phys. Rev. Lett. **112**, 146601 (2014).

[156] P. A. Lee and T. V. Ramakrishnan, Phys. Rev. B **26**, 4009 (1982).

[157] X. Zhang, J. M. Woods, J. J. Cha, and X. Shi, Phys. Rev. B **102**, 115161 (2020).

[158] B. Yan and C. Felser, Annu. Rev. Condens. Matter Phys. **8**, 337 (2017).

[159] P. Hosur and X. Qi, Comptes Rendus Physique **14**, 857 (2013).

[160] A. A. Burkov, Journal of Physics: Condensed Matter **27**, 113201 (2015).

[161] Z. K. Liu, L. X. Yang, Y. Sun, T. Zhang, H. Peng, H. F. Yang, C. Chen, Y. Zhang, Y. F. Guo, D. Prabhakaran, M. Schmidt, Z. Hussain, S.-K. Mo, C. Felser, B. Yan, and Y. L. Chen, Nat. Mater. **15**, 27 (2016).

[162] X. Wan, A. M. Turner, A. Vishwanath, and S. Y. Savrasov, Phys. Rev. B **83**, 205101 (2011).

[163] G. Xu, H. Weng, Z. Wang, X. Dai, and Z. Fang, Phys. Rev. Lett. **107**, 186806 (2011).

[164] Z. Wang, M. G. Vergniory, S. Kushwaha, M. Hirschberger, E. V. Chulkov, A. Ernst, N. P. Ong, R. J. Cava, and B. A. Bernevig, Phys. Rev. Lett. **117**, 236401 (2016).

[165] T. Suzuki, R. Chisnell, A. Devarakonda, Y.-T. Liu, W. Feng, D. Xiao, J. W. Lynn, and J. G. Checkelsky, Nat. Phys. **12**, 1119 (2016).

[166] K. Ohgushi, S. Murakami, and N. Nagaosa, Phys. Rev. B **62**, R6065 (2000).

[167] G. Xu, B. Lian, and S.-C. Zhang, Phys. Rev. Lett. **115**, 186802 (2015).

[168] R. Weihrich, I. Anusca, and M. Zabel, Z. Anorg. Allg. Chem. **631**, 1463 (2005).

[169] R. Weihrich and I. Anusca, Z. Anorg. Allg. Chem. **632**, 1531 (2006).

[170] P. Vaqueiro and G. Sobany, Solid State Sciences **11**, 513 (2009).

[171] W. Schnelle, A. Leithe-Jasper, H. Rosner, F. M. Schappacher, R. Pöttgen, F. Pielnhofer, and R. Weihrich, Phys. Rev. B **88**, 144404 (2013).

[172] H.-J. Kim, K.-S. Kim, J.-F. Wang, M. Sasaki, N. Satoh, A. Ohnishi, M. Kitaura, M. Yang, and L. Li, Phys. Rev. Lett. **111**, 246603 (2013).

[173] H. Li, H. He, H.-Z. Lu, H. Zhang, H. Liu, R. Ma, Z. Fan, S.-Q. Shen, and J. Wang, Nat. Commun. **7**, 10301 (2016).

[174] M. Hirschberger, S. Kushwaha, Z. Wang, Q. Gibson, S. Liang, C. A. Belvin, B. A. Bernevig, R. J. Cava, and N. P. Ong, Nat. Mater. **15**, 1161 (2016).

[175] B. A. Assaf, T. Phuphachong, E. Kampert, V. V. Volobuev, P. S. Mandal, J. Sánchez-Barriga, O. Rader, G. Bauer, G. Springholz, L. A. de Vaulchier, and Y. Guldner, Phys. Rev. Lett. **119**, 106602 (2017).

[176] A. V. Andreev and B. Z. Spivak, Phys. Rev. Lett. **120**, 026601 (2018).

[177] S. Wiedmann, A. Jost, B. Fauqué, J. van Dijk, M. J. Meijer, T. Khouri, S. Pezzini, S. Grauer, S. Schreyeck, C. Brüne, H. Buhmann, L. W. Molenkamp, and N. E. Hussey, Phys. Rev. B **94**, 081302 (2016).

[178] F. AU Arnold, C. Shekhar, S.-C. Wu, Y. Sun, R. D. dos Reis, N. Kumar, M. Naumann, M. O. Ajeesh, M. Schmidt, A. G. Grushin, J. H. Bardarson, M. Baenitz, D. Sokolov, H. Borrmann, M. Nicklas, C. Felser, E. Hassinger, and B. Yan, Nat. Commun. **7**, 11615 (2016).

[179] A. A. Burkov, Phys. Rev. B **96**, 041110 (2017).

[180] S. Nandy, G. Sharma, A. Taraphder, and S. Tewari, Phys. Rev. Lett. **119**, 176804 (2017).

[181] A. A. Taskin, H. F. Legg, F. Yang, S. Sasaki, Y. Kanai, K. Matsumoto, A. Rosch, and Y. Ando, Nat. Commun. **8**, 1340 (2017).

[182] P. Li, C. H. Zhang, J. W. Zhang, Y. Wen, and X. X. Zhang, Phys. Rev. B **98**, 121108 (2018).

[183] R. Singha, S. Roy, A. Pariari, B. Satpati, and P. Mandal, Phys. Rev. B **98**, 081103 (2018).

[184] N. Kumar, S. N. Guin, C. Felser, and C. Shekhar, Phys. Rev. B **98**, 041103 (2018).

[185] F. C. Chen, X. Luo, J. Yan, Y. Sun, H. Y. Lv, W. J. Lu, C. Y. Xi, P. Tong, Z. G. Sheng, X. B. Zhu, W. H. Song, and Y. P. Sun, Phys. Rev. B **98**, 041114 (2018).

[186] M. Wu, G. Zheng, W. Chu, Y. Liu, W. Gao, H. Zhang, J. Lu, Y. Han, J. Zhou, W. Ning, and M. Tian, Phys. Rev. B **98**, 161110 (2018).

[187] J. Yang, W. L. Zhen, D. D. Liang, Y. J. Wang, X. Yan, S. R. Weng, J. R. Wang, W. Tong, L. Pi, W. K. Zhu, and C. J. Zhang, Phys. Rev. Materials **3**, 014201 (2019).